Two Phase Flow Solver for Solid Particles in Hypersonic Martian Entry Flows

A thesis accepted by the Faculty of Aerospace Engineering and Geodesy of the Universität Stuttgart in partial fulfillment of the requirements for the degree of Doctor of Engineering Sciences (Dr.-Ing.)

by

Abdul Majid

born in Sahiwal, Pakistan

main referee: Prof. Dr. rer. nat. Hans-Peter Röser
co-referee: Prof. Dr.-Ing. habil. Jean-Marc Moschetta
Date of defense: 15.03.2011

Institute of Space Systems

Universität Stuttgart

2011

It is difficult to express my gratitude to my supervisors Dr.-Ing. Georg Herdrich and Dr.-Ing. Markus Fertig and my colleague Uwe Bauder, so I simply say that this thesis would have remained a dream without the support of them.

Abstract

In the Martian atmosphere heavy storms occur, which transport dust particles even into the higher atmosphere, i.e. up to 40 km of altitude. These particles, with sizes of up to $20\mu m$, consist of silicon oxides and iron oxides may affect the heat load on the heat shield during atmospheric entry. In this present study, these additional loads due to impingement of solid particles in hypersonic entry flows in Martian atmosphere are investigated.

The Euler-Lagrangian approach is used for the modeling and simulation of solid particles in hypersonic Martian entry flows. For the simulation, the program SINA (Sequential Iterative Non-equilibrium Algorithm) previously developed at the Institut für Raumfahrtsysteme is used. SINA consists of different solvers that are loosely coupled. The main limitation of the code was that it could simulate only air flows consisting of eleven species. However, taking advantage of the loose coupling between the solvers, the capabilities of SINA are not only extended to simulate gases other than air, but also to two-phase flow applications. For the Martian atmospheric chemistry model, only carbon dioxide (CO_2) is taken into account because Mars atmosphere consists of 95.3% CO_2. Considering that the entry velocity in the Mars atmosphere is usually around 5-7 km/s, the dissociation of CO_2 has to be taken into account. Therefore, a five species model (carbon dioxide (CO_2), molecular oxygen (O_2), carbon monoxide (CO), oxygen (O) and carbon (C)) is implemented in the code. CO_2 has three modes of vibration, because it is a three atomic molecule. Previously in SINA, there was no provision to take into account vibrational energies for the three atomic molecule. Therefore, a vibrational model for the three atomic molecule is developed and implemented in the code.

Both phases, the gaseous phase and the particle phase, interact with each other through one-way or two-way coupling. In one-way coupling, there is no influence of the particle phase on gas phase. However, two-way coupling takes into account particle phase impact on the gaseous flowfield. The model for the effect of the flowfield gas on a particle includes drag force and particle heating. An adequate model for the drag force computation is implemented in the model in order to take into account transitional and rarefied flows. The heat transfer model of the particle consists of convective heating and radiation cooling. The radiative heating from the gas to the particle is not taken into account because this model is not available in SINA. Due to relative velocity difference in the gas and particle, the development of the local shock may introduce extra heating to the particle. In order to take into account this effect, a normal stagnation point

Abstract

shock relation is also introduced for the computation of particle temperature. The phase change of the particle due to high temperature of the flowfield is also considered. A semi empirical model for the particle-wall interaction is presented. Depending on the input conditions, the erosion mass loss of a charring ablator using an engineering correlation is also discussed.

Verification and validation are the primary means to assess accuracy and reliability in computational simulations. In order to obtain higher confidence and to have a code with as few errors as possible, the models and solvers being implemented in the code are verified and validated with external established resources. The TINA code of Fluid Gravity Engineering (FGE) is used for the verification of particle momentum and heat transfer models. The results of particle momentum agree closely but a notable difference in the values of temperature is found between both codes. In order to further assess the accuracy of thermal model of particle solver, the DSMC code DS2V is also employed. The chemical equilibrium constants of the Martian atmospheric model are validated using the CEA (Chemical Equilibrium with Applications) code of NASA.

Parametric analysis is done regarding the impact of variation in the physical input conditions like position, velocity, size and material of the particle on particle-wall interaction. Particle movement is characterized by transitional and rarefied flow properties due to the low gas densities and small particle sizes. Convective heat fluxes onto the surface of the particle and its radiative cooling are discussed. Variation of particle temperatures under different conditions and for differently sized particle is presented. Mass loss or decrease in particle sizes due to higher temperature is explained. Heat fluxes onto the wall due to impingement of particles are also computed and compared with the heat fluxes from the gas.

Zusammenfassung

In der Marsatmosphäre treten starke Stürme auf, die Staubpartikel bis in Höhen von 40km transportieren. Diese bis zu 20μm großen Partikel bestehen aus Siliziumoxiden und Eisenoxiden und beeinflussen die Wärmelast auf den Hitzeschutzschild eines Raumfahrzeugs während des atmosphärischen Eintrittsmanövers. In der vorliegenden Arbeit wird diese zusätzliche Belastung aufgrund der festen Partikel in einer hypersonischen Eintrittsströmung in die Marsatmosphäre untersucht.

Für die Simulation fester Partikel in hypersonischen Eintrittsströmungen am Mars wird ein Euler-Lagrange-Ansatz gewählt. Die Simulation der Zweiphasenströmung erfolgt mit dem am Institut für Raumfahrtsysteme (IRS) entwickelten Navier-Stokes-Löser für hypersonische Strömungen im thermischen und chemischen Nichtgleichgewicht SINA (Sequentieller Iterativer Nichtgleichgewichts-Algorithmus). SINA besteht aus verschiedenen, lose gekoppelten Lösern und wurde ursprünglich für die Simulation eines 11-Komponenten-Luftgemischs entwickelt. Die Weiterentwicklung des Programms, basierend auf der lose gekoppelten Struktur, erlaubt nun nicht nur eine Simulation anderer Gase als Luft, sondern auch die Simulation von Zweiphasenströmungen.

Für das Chemie-Modell der Marsatmosphäre wird ausschließlich CO_2 berücksichtigt, da sein Anteil an der Atmosphäre 95,3% beträgt. Betrachtet man weiterhin die niedrigen Eintrittsgeschwindigkeiten in die Marsatmosphäre von 5-7 km/s, so müssen lediglich Dissoziationen, jedoch keine Ionisationen von CO_2 in das Chemiemodell aufgenommen werden. Daher wurde ein 5-Komponenten-Modell bestehend aus Kohlendioxid CO_2, molekularem Sauerstoff O_2, Kohlenmonoxid CO, atomarem Sauerstoff O und Kohlenstoff C implementiert.

Das Kohlendioxid-Molekül CO_2 ist ein lineares, 3-atomiges Molekül, wohingegen im ursprünglichen 11-Komponenten Luftgemisch maximal 2-atomige Moleküle vorhanden sind. Daher wurde ein Modell für die Vibrationsenergie 3-atomiger Moleküle entwickelt und in SINA implementiert.

Das Modell für die Interaktion zwischen dem Gas und den Partikeln berücksichtigt den Strömungswiderstand und die Aufheizung der Teilchen. Für die Berechnung der Beschleunigung der Partikel ist ein Modell implementiert, das auch Übergangsströmungen und verdünnte Strömungen um die Partikel berücksichtigt. Das Wärmeübertragungsmodell beinhaltet den konvektiven Wärmeübergang auf die Teilchen und deren Strahlungskühlung, wobei der Einfluß der Strahlung auf die Gas-Phase nicht berücksichtigt wird. Zusät-

zlich werden hierbei lokale Überschallgeschwindigkeiten zwischen Gas und Partikel berücksichtigt, die den Wärmeübergang erhöhen. Die Massenabnahme der Teilchen durch Sublimation wird ebenfalls berücksichtigt. Für die Interaktion der Partikel mit einer festen Wand wird ein semi-empirisches Modell präsentiert.

Die beiden Phasen interagieren miteinander durch Ein-Wege-Kopplung oder Zwei-Wege-Kopplung. Bei der Ein-Wege-Kopplung gibt es im Gegensatz zur Zwei-Wege Kopplung keine Rückkopplung der Partikel auf die Gas-phase.

Verifizierung und Validierung sind unabdingbare Grundlagen für die Untersuchung der Genauigkeit und Verlässlichkeit numerischer Simulationen. Die neu implementierten Modelle und Löser werden anhand externer Quellen verifiziert und validiert, um Aussagen über die Qualität der Lösungen zu erhalten und mögliche Fehler zu minimieren. Das Programm TINA von Fluid Gravity Engineering (FGE) wird für die Verifizierung des Impuls- und Wärmeübertragungsmodells des Partikel-Lösers verwendet. Das Modell zur Berechnung des Wärmeübergangs auf die Partikel unter Berücksichtigung lokaler relativer Überschallströmungen um die Partikel wird verglichen mit Ergebnissen aus dem DSMC-Code DS2V. Die Gleichgewichtskonstanten des Chemiemodells werden mit dem CEA-Code (Chemical Equilibrium with Applications) der NASA validiert.

Mit den beschriebenen Modellen werden dann Parameterstudien mit variierenden Einströmbedingungen der Partikel wie Position, Geschwindigkeit, Größe und Material durchgeführt und deren Einfluß auf die Partikel-Wand Interaktion untersucht. Der konvektive Wärmefluss auf die Partikeloberfläche und die Strahlungskühlung werden diskutiert und die Änderung der Temperatur der Teilchen für verschiedene Parameter wird für unterschiedlich große Partikel präsentiert. Ebenso wird der Massenverlust und die damit einhergehende Größenänderung der Partikel durch Sublimation beschrieben. Schließlich wird der Wärmefluß auf eine feste Wand und die Erosion eines Ablators aufgrund auftreffender Partikel für verschiedene Anströmbedingungen berechnet und diskutiert.

Acknowledgments

Above all, I am grateful to The Allah Almighty, without HIS help and mercy it would not have been possible for me to complete this work.

This thesis would not have been completed without the help, support, guidance, and efforts of many people. I cordially want to thank my "Doktorvater" Professor Dr. Hans-Peter Röser for giving me the opportunity to work at the Institute of Space Systems and his support during the entire time. I greatly appreciate his kindness and very positive thinking.

It is with immense gratitude that I acknowledge the support and help of professor Dr.-Ing. Jean-Marc Moschetta. Without his kindness and assistance it would not have been possible for me to finish my thesis in time. I am also thankful for him regarding his valuable suggestions to improve the quality of thesis.

I am indebted to my many colleagues who supported me to finish my research work. I would like to thank Torsten Stindl for his invaluable support during my entire stay. His suggestions and advice always help me to improve my work. It gives me great pleasure in acknowledging the support and help of my "RTT" group. Every body was very supportive. I will really miss all of them. I am very much grateful for their kindness and assistance at every step.

My sincere thank also goes to Dr. James beck of Fluid Gravity Engineering Ltd. for his valuable support and cooperation. He provided me the opportunity to make a code to code comparison in order to verify and validate models and results.

Many thanks to SUPARCO and the Higher Education Commission (HEC) of Pakistan for financially supporting this research. Without their help it was not possible for me to work on this thesis. A heartfelt thank to Mr. Mujeeb-ur-Rehman and Mr. Amin Bahadur for their help and kindness. Their support allowed me to focus on my studies. Also I want to say thanks to DAAD (German Academic Exchange Service) for providing continuous administrative support during my entire stay in Germany.

I also want to say thanks to German people and Germany. I have learned lot of things from your rich culture. This will help me throughout my life. Especially I want to say thanks to my neighbors Mr. Razzaq and his family who were very friendly throughout my stay in Esslingen. My warm thanks are due to Mr. Rauf and his wife Fazila. Their kindness and generosity are very much appreciated.

Acknowledgments

The last and certainly the most, I owe my loving thanks to my wife Maria. She lost a lot due to my research abroad. Without her encouragement and understanding it would have been impossible for me to finish this work. My daughter Hania who come in this world during my stay in Germany really enlightened my life. She deserves a special praise whose smiles and talks were a source of energy for me.

Contents

CONTENTS

Nomenclature

Symbols

a	speed of sound $(\frac{\text{m}}{\text{s}})$
a_c	acceleration $(\frac{\text{m}}{\text{s}^2})$
a_n	restitution coefficient in normal direction $(-)$
a_τ	restitution coefficient in tangential direction $(-)$
A	activation energy $(\frac{\text{kJ}}{\text{mol}})$
$A_{in,\perp}$	cell area perpendicular to inflow (m^2)
$\vec{B}$	magnetic induction $(\frac{\text{A}}{\text{M}})$
B^*	dimensionless collision integral ratio $(-)$
c	species concentration $(\frac{\text{mol}}{\text{m}^3})$
c_i	molar concentration of species i $(\frac{\text{mol}}{\text{cm}^3})$
c_p	specific heat capacity at constant pressure $(\frac{\text{J}}{\text{kgK}})$
c_v	specific heat capacity at constant volume $(\frac{\text{J}}{\text{kgK}})$
C_d	drag force coefficient $(-)$
D	coefficient of diffusion $(\frac{\text{m}^2}{\text{s}})$
D_0	dissociation energy $(\frac{\text{J}}{\text{mol}})$
$\vec{D}_i$	effective diffusion coefficient of species i $(\frac{\text{m}^2}{\text{s}})$
$\vec{D}_{ij}$	multi component diffusion coefficient $(\frac{\text{m}^2}{\text{s}})$
$\overline{D}_n$	particle average diameter (m)
D_p	effective particle diameter (m)
E	energy (J)
E_i	ionization energy $(\frac{\text{kJ}}{\text{mol}})$
E_p	particle energy source term $(\frac{\text{J}}{\text{m}^3\text{s}})$
f	degree of freedom $(-)$

NOMENCLATURE

$\vec{f}_d$ — drag force (N)

f_n — number frequency $(-)$

$\vec{F}$ — inviscid/viscous fluxes $(\frac{\text{kg}}{\text{m}^2\text{s}}, ..., \frac{\text{Ns}}{\text{m}^2\text{s}}, ..., \frac{\text{J}}{\text{m}^2\text{s}})$

$\vec{F}_{p,cell}$ — momentum source term in a cell (N)

F_m — fractional mass of particles (kg)

$F_{x,y,z,p}$ — particle momentum source terms $(\frac{\text{J}}{\text{m}^3\text{s}})$

g — degeneracy $(-)$

h — mass specific enthalpy $(\frac{\text{J}}{\text{kg}})$

h_L — latent heat of evaporation $(\frac{\text{J}}{\text{kg}})$

H_e — volume specific enthalpy of electron $(\frac{\text{J}}{\text{m}^3})$

H_t — volume specific total enthalpy $(\frac{\text{J}}{\text{m}^3})$

$\vec{j}$ — diffusion mass flux $(\frac{\text{kg}}{\text{m}^2\text{s}})$

j — current density $(\frac{\text{A}}{\text{m}^2})$

k_b — backward reaction rate constant $(\frac{1}{\text{s}}[\frac{\text{mol}}{\text{m}^3}]^{1-\sum \nu_{ij}''})$

K_c — equilibrium constant $([\frac{\text{mol}}{\text{m}^3}]^{\sum(\nu_{ij}''-\nu_{ij}')})$

k_f — forward reaction rate constant $(\frac{1}{\text{s}}[\frac{\text{mol}}{\text{m}^3}]^{1-\sum \nu_{ij}'})$

m — mass (kg)

$\dot{m}$ — rate of mass loss of the particle $(\frac{\text{kg}}{\text{s}})$

M — mach number $(-)$

M_{evp} — particle mass loss source term $(\frac{\text{J}}{\text{m}^3\text{s}})$

$\overline{M}$ — mean molar mass $(\frac{\text{kg}}{\text{kmol}})$

M_{ratio} — mixing ratio of particles in gas $(-)$

M_{rel} — relative Mach number $(-)$

n — number density $(\frac{1}{\text{m}^3})$

$\dot{n}$ — numbers of particles in cell per unit time $(\frac{1}{\text{s}})$

n_{mol} — number of molecules $(-)$

N — total number of particles to be injected $(-)$

N_{u_0} — Nusselt number for continuum region $(-)$

N_u — Nusselt number with rarefaction effects $(-)$

N_{cell} — number of particles in a cell $(-)$

p — pressure $(\frac{\text{N}}{\text{m}^2})$

p_t — total pressure $(\frac{\text{N}}{\text{m}^2})$

$\vec{P}$ — particle position $(-)$

$\vec{P}_{1-4}$ — position vectors $(-)$

$P_{K,1-9}$ — coefficient to determine equilibrium constant $(-)$

$P_{\overline{\Omega},1-5}$	curve fits coefficients for collision integral $(-)$
$q_{c,cell}$	convective heat flux in a cell (N)
$\vec{q}$	source term $(\frac{\text{kg}}{\text{m}^3}, ..., \frac{\text{Ns}}{\text{m}^3}, ..., \frac{\text{J}}{\text{m}^3})$
$\vec{q_r}$	radiative flux $(\frac{\text{J}}{\text{m}^3})$
Q_c	convective heat flux $(\frac{\text{W}}{\text{m}^2})$
$\dot{Q}_{net}$	rate of net heat transfer $(\frac{\text{W}}{\text{m}^2})$
Q_r	radiative heat flux $(\frac{\text{W}}{\text{m}^2})$
Q_{c-v}	chemical-vibrational energy exchange term $(\frac{\text{J}}{\text{m}^3\text{s}})$
Q_{t-v}	translational-vibrational energy exchange term $(\frac{\text{J}}{\text{m}^3\text{s}})$
Q_{v-v}	vibration-vibration energy exchange term $(\frac{\text{J}}{\text{m}^3\text{s}})$
Q_{e-v}	electron-vibration energy exchange term $(\frac{\text{J}}{\text{m}^3\text{s}})$
r_p	radius of the particle (m)
Re_{rel}	relative Reynolds number $(-)$
s, r, A^*	modeling parameters for Park's TT_{vib} model(-)
S	speed ratio $(-)$
$\vec{S}$	source term $(\frac{\text{kg}}{\text{m}^3}, ..., \frac{\text{Ns}}{\text{m}^3}, ..., \frac{\text{J}}{\text{m}^3})$
S°	standard entropy $(\frac{\text{J}}{\text{molK}})$
t_c	characteristic time for chemical reactions (s)
t_f	characteristic time for fluid motion (s)
t_v	characteristic time for vibrational relaxation (s)
T	temperature (K)
T_{shock}	gas temperature including shock effects (K)
$\dot{T}_{rate}$	rate of temperature change $(\frac{\text{K}}{\text{s}})$
V	volume of a cell (m^3)
$\vec{V}$	total velocity $(\frac{\text{m}}{\text{s}})$
$\vec{X}$	solution vector $(\frac{\text{kg}}{\text{m}^3}, ..., \frac{\text{Ns}}{\text{m}^3}, ..., \frac{\text{J}}{\text{m}^3})$
z_{mol}	number of molecules $(-)$
z_r	number of reactions $(-)$
z_s	number of species $(-)$

Constants

k	Boltzmann constant $(1.3806504 \times 10^{-23}\frac{\text{J}}{\text{k}})$
$\Re$	universal gas constant $(8.314472\frac{\text{J}}{\text{molK}})$
σ	Stefan Boltzmann constant $(5.670400 \times 10^{-8}\frac{\text{W}}{\text{m}^2\text{K}^4})$

Greek Symbols

α_p	volume fraction of disperse phase $(-)$

NOMENCLATURE

Δt	time step (s)
Δm_a	ablator sample mass loss (kg)
Δm_{ref}	ablator mass loss for dust-free flow (kg)
γ	specific heat ratio $(-)$
λ	coefficient of thermal conductivity $(\frac{W}{mK})$
μ	gas viscosity $(\frac{kg}{ms})$
ν	general stoichiometric coefficient $(-)$
ν'	stoichiometric coefficients of a source component $(-)$
ν''	stoichiometric coefficients of a product component $(-)$
$\dot{\omega}$	reaction rate $(\frac{mol}{m^3 s})$
$\overline{\Omega}_{ij}^{(l,s)}$	collision integral (average effective collision cross section)(m^2)
ρ	density $(\frac{kg}{m^3})$
σ	electrical conductivity $(\frac{S}{m})$
τ	relaxation time (s)
τ_{ij}	shear and normal stresses (Pa)

Superscripts

$+$	value after wall interaction
$-$	value before wall interaction
eq	equilibrium
i, j	species index
$n+1$	current state
n	previous state

Subscripts

0	ground / standard state
$2way$	2 way coupling effect
app	'appearing', i.e. formed during reaction, product substance
ch	chemical contribution
e	electron
eff	effective
f, b	forward , backward
g	gas
ij	indices represents x & y directions
i, j, k, l	species
int	internal energy
mr	molecular species

p	particle
r	reaction index
rel	relative
va	'vanishing', i.e. decomposed during reaction, starting substance
v, vib	vibrational
x, y, z	coordinates

Acronyms

CEA	Chemical Equilibrium with Applications
CLL	Cercignani-Lampis-Lord
DS2V	Bird's DSMC code with graphical user interface
DSMC	Direct Simulation Monte Carlo
FGE	Fluid Gravity Engineering Ltd.
HERTA	High Enthalpy Radiation Transport Algorithm
IRS	Institut für Raumfahrtsysteme
JAXA	Japan Aerospace Exploration Agency
Mars C.O.	Mars Climate Orbiter
Mars G.S.	Mars Global Surveyor
Mars Obs.	Mars Observer
Mars R.O.	Mars Reconnaissance Orbiter
MSRO	Mars Sample Return Orbiter
NIST	National Institute of Standards and Technology
NASA	National Aeronautics and Space Administration
PARADE	PlasmA RAdiation DatabasE
RSA	Russian Space Agency
SINA	Sequential Iterated Non-equilibrium Algorithm
TPS	Thermal Protection Systems
TINA	Thermochemical Implicit Non-Equilibrium Algorithm

CONTENTS

Chapter 1

Introduction

Inspired by the search for extraterrestrial life, Mars has been the most frequently visited planet in the solar system. The exploration of Mars is an important part of the space exploration programs of many countries across the world. Dozens of robotic spacecrafts, including orbiters, landers, and rovers, have been launched towards Mars since the 1960s. No less than thirty five attempts have been made to orbit or land on the surface of the red planet by National Aeronautics and Space Administration (NASA), the European Space Agency (ESA), the Russian Space Agency (RSA) and Japan Aerospace Exploration Agency (JAXA, Japan) [1; 2]. The summary of these missions is presented in table 1.1.

Within the next years, further interplanetary missions to Mars are also planned, like the Mars Science Laboratory (MSL) in 2011 by NASA [3], the Mars Atmosphere and Volatile EvolutioN (MAVEN) mission in 2013 by NASA [3], ExoMars (Exobiology on Mars) in 2018 by ESA [4] and Phobos-Grunt, the joint Russian and Chinese mission, that is rescheduled to be launched in 2011 [5] and others. These missions aim at gathering data about current atmospheric /geological conditions and answering questions about the history of Mars as well as a preparation for a possible manned mission to Mars. Since the 1990s many initiatives have been announced for space exploration that are to culminate in landing men on Mars in near future.

Table 1.1: Summary of Previous Mars Entry Missions

Flight	Agency	Entry Date	Notes
Korabl 4	RSA	Oct.10,1960(L)	Launch failure
Korabl 5	RSA	Oct.14,1960(L)	Launch failure

1. INTRODUCTION

Korabl 11	RSA	Oct.24,1962(L)	Launch failure
Korabl 13	RSA	Nov.4,1962(L)	Launch failure
Mars 1	RSA	Nov.1, 1962(L)	Controllers lost contact
Mariner 3	NASA	Nov.5,1964(L)	Launch failure
Mariner 4	NASA	July 14,1965	First successful mission
Zond 2	RSA	Nov.30,1964(L)	Controllers lost contact
Mariner 6	NASA	July 31,1969	Successful mission
Mariner 7	NASA	Aug.5,1969	Successful mission
Mars 1969A	RSA	Mar.27,1969(L)	Launch failure
Mars 1969B	RSA	April2, 1969(L)	Launch failure
Mariner 8	NASA	May8,1971(L)	Launch failure
Kosmos 419	RSA	May10,1971(L)	Launch failure
Mariner 9	NASA	Nov.14,1971	Successful mission
Mars 2	RSA	Nov.27,1971	Lander crashed
Mars 3	RSA	Dec.2,1971	Operated for 20 sec.
Mars 6	RSA	Mar.12,1974	Lander crashed
Mars 7	RSA	Mar.6,1974	Targeting error
Viking I	NASA	Jul.20,1976	Successful mission
Viking II	NASA	Sep.3,1976	Successful mission
Phobos 1	RSA	Jul.7,1988(L)	Controller failure
Phobos 2	RSA	Jan.29,1989	Partially successful
Mars Obs.	NASA	Sep.25,1992(L)	lost contact
Mars G.S.	NASA	Sep.12,1997	Highly successful
Mars96	RSA	Nov.16,1996 (L)	Launch failure
Pathfinder	NASA	Jul.4,1997	Successful mission
Mars C.O.	NASA	Dec.11,1998 (L)	Math. convers. failure
MPL	NASA	Dec.3,1999	Failure during descent
DS-2	NASA	Dec.3,1999	Lost after separation
Mars Odyssey	NASA	Oct.24,2001	Successful mission
Nozomi	ISAS	Dec.14,2003	Wrong thrust predict.
Beagle	ESA	Dec.25,2003	Lost after separation
MER-A	NASA	Jan.3,2004	Roving across Mars
MER-B	NASA	Jan.24,2004	Roving across Mars
Mars R.O.	NASA	Mar.10,2006	Successful mission
Phoenix	NASA	Aug.4,2007	Successful mission

When the hypersonic flow encounters a vehicle, the kinetic energy associated with hypervelocity flight is converted into increasing the temperature of the air and into endothermic reactions, such as dissociation and ionization of the air near the vehicle surface. The mechanism for this conversion includes adiabatic compression and viscous energy dissipation. Heat is transferred from the high temperature air to the surface. The rate at

which heat is transferred to the surface depends upon many factors, including the free stream conditions, the configuration of the vehicle and its orientation to the flow, the difference between the temperature of the air and the temperature of the surface, and the surface catalycity. This is very important for the successful mission that the heat fluxes onto the vehicle surface during hypersonic reentry should be addressed appropriately. The Thermal Protection Systems (TPS) are used to protect the vehicle surface because the material of the reentry vehicles cannot withstand very high heat loads or temperatures.

Of all successful entries into the Martian atmosphere to date, only the first two (Viking I and II) have entered the orbit of the planet prior to atmospheric entry. The decision to enter the Viking spacecraft from Mars orbit was made in part due to concerns about the severity of the entry heating environment in a (then) relatively unknown atmosphere. All subsequent missions have entered Martian atmosphere directly on a hyperbolic trajectory, which leads to higher entry velocities, and, therefore, higher heat fluxes and mechanical loads, than an orbital entry. This trajectory lowers the needed total mass of the spacecraft by eliminating the fuel and propulsion system necessary to perform the Mars Orbit Insertion (MOI) maneuver. However, the thermal protection system (TPS), which shields the spacecraft from the intense heat generated during the entry, becomes heavier as the entry velocity (and therefore encountered heating rate) increases. Still the velocities on the order of 7-9 km/s are possible for future crewed missions [6], for which the desire for reduced mission duration may be more important than minimizing fuel consumption. However this will require larger TPS and the larger TPS mean increase in radiative heat flux.

The design of a low mass and reliable (low risk) TPS system for Martian atmospheric entry requires an accurate prediction of the aerothermal environment encountered. The peak heat flux (along with surface pressure and shear stress) will determine the thermal protection material selected for the heatshield, while the total integrated heat load determines the required material thickness .

1.1   Dust storms in Martian atmosphere

Earlier missions to Mars commenced with the Korabl and Mariner of the 1960s. In 1965, the first successful flyby of Mars, Mariner 4, provided the first closeup images of another planet. Along with the Mariner 6 and 7 flybys in 1969, it provided images of a moon like planet pocked with impact craters. In the 1971 Mariner 9 orbiter provided evidence of dry flood channels and volcanism on Mars. It was the first spacecraft to go into orbit

around another planet. However, excitement for its arrival was subdued by a dark cloud. A Martian dust storm, which had started in late September 1971, had grown to cover the entire planet and this storm lasted for more than 3 months. The occurrence of global dust storms on Mars is one of the most spectacular meteorological events in the solar system. Each year, as the planet nears perihelion, numerous small-scale dust storms develop in the southern hemisphere, and one or several of these, for reasons not fully understood, occasionally grows to global proportions in a matter of days. As they approach maturity, these storms spread dust over much of the planet, suspending micron-sized particles to heights in excess of 40 km and obscuring surface features for weeks at a time [7]. Typically, several months pass before pre-storm conditions are reached. It seems remarkable that the rare Martian atmosphere, which exerts a mean surface pressure of about 6 mbar, is capable of producing such intense and long-lived events. Serious interest in the nature of global dust storms began after the Mariner 9 spacecraft documented the decline of what appears to be one of the most intense storm on record.

1.2 Issues concerning hypersonic entry into dusty atmosphere

During interplanetary missions, high speed atmospheric entry is an important event. When entering the atmosphere of a planet, the thermal load onto the space vehicle is a critical design parameter and has to be determined in advance for a successful mission. The structure of the Martian atmosphere and its composition are known [8; 9]. The dust particles, with sizes of up to 20µm, consist of iron oxides and silicon oxides are present to high altitudes in the Martian atmosphere [10; 11; 12]. It is evident that they affect the load on the heat shield during entry. Recent investigations have shown that the presence of small particles (with a size of a micron or fractions of a micron) in a hypersonic flow may cause a significant increase of the heat flux to the front surface of a probe even if the particles have low mass concentration [13].

Besides the effect of extra heating on the surface of the vehicle, the particles may change the geometry of the surface at micro level. Due to impingement of the particles on the vehicle surface, the particles will increase the roughness, which will change the flow field behavior around the vehicle. In addition boundary layer transition will occur from laminar to turbulent that may result not only increasing the heat flux but also in modifying the aerodynamic characteristic of the flowfield surrounding the object. In this

way, the particles have an indirect effect on the vehicle and it is very important to study these effects associated with dust particles during atmospheric entry flows.

1.3 State of the art

After the Mars mission probes encountered dust storms, the experimental and numerical investigations were initiated in order to determine the impact of dust particles on the vehicle during hypersonic entry. Various groups across the world made experimental investigations on the influence of solid particles in high temperature gas flows, e.g. Gorimir [14], Keller [15] and others. The experimental work mostly focused on the erosion of TPS material due to solid particles impingement. At the Institut für Raumfahrtsysteme (IRS), experiments were performed by Endlich [16] during her research work in order to observe and analyze the interaction between the solid particles and TPS test piece in plasma. The mass loss and increase in heat flux of the particles were observed. Besides experimental work, Papadopoulos et al. [17] numerically analyzed the influence of dust particles onto the vehicle during Martian entry and found a significant increase of heat flux due to impingement of the particles. However, the work of Grant et al. [18] opposed the findings of Papadopoulos [17] by stating that the heat flux due to impingement of the particles onto the entry vehicle surface was overestimated previously. They also stated, that the results are for a specific vehicle flying a specific trajectory at a specific point in time. Keeping in view the difference of opinions and to get a detailed insight of the issues concerning influence of dust particles in hypersonic Martian entry flows, there was a need to make further investigations.

1.4 Objectives of the thesis

Regarding future Mars missions (specially manned missions), it is very important to consider all possible or foreseeable events that may occur during the mission. The experimental work done so far was either mission specific or were performed in a narrow window of inflow conditions. As far as numerical investigation is concerned, the works done and published was always task specific and provides a narrow picture of the problem. Also the difference of opinion about the results exists among the researchers. Therefore, it is very important to make a detailed investigation and provide a comprehensive overview of the problem.

The dust particle simulation during hypersonic entry flows is a two phase flow problem. A lot of research has been made in this field, but only in subsonic flows. However the limited number of people have worked on the two phase problem of solid particles in hypersonic or high temperature gas flows. Therefore, there is a need to make a detailed investigation in this field not only to determine the impact on the heat shield material due to impingement of solid particles, but also to provide a numerical tool for future research.

At IRS, there is no tool available that can be used for the simulation of solid particles in Martian atmosphere. Therefore, the first and foremost task is to extended the capabilities of SINA* (Sequential Iterated Non-equilibrium Algorithm) to be used for the atmospheres other than Earth such as Martian atmosphere. The entry velocity to the Martian atmosphere is hypersonic. Due to hypersonic flow, the gas temperature increases sharply because a strong bow shock forms in front of vehicle. The chemical and thermal non equilibrium processes have to be taken into account due to high temperature gas. Therefore, the chemical part of SINA has to be modified. This is also intend to make it more flexible so that it can simulate any species or environment. The chemical kinetics model for the Martian atmosphere is needed to be implemented. This requires not only implementation of reaction scheme for the chemical solver but also an update of the data files needed for the computation of transport coefficient.

For two-phase flow applications, a new particle solver has to be developed and loosely coupled with SINA code. This particle solver should have the capability to simulate solid particles in hypersonic or high temperature gas flows. The parameters of the particle may change drastically downstream the shock and this has to be investigated carefully and throughly. The particle solver is also intended to be make as maximum as possible general, so that its application may be extended to simulate solid particles in nozzle or plasma flows etc.† Verification and validation are the primary means to assess accuracy and reliability of models developed. Therefore, the new implemented solvers in SINA has to be verified and validated with external sources.

1.5　Thesis outline

Two-phase flow modeling is necessary in order to take into account particle influence in hypersonic entry flows. One phase is the gaseous flowfield and the solid particles are treated as the second phase. In chapter 2, a brief overview is given about the gaseous

---

*SINA could simulate only Earth entries with 11 species air model.

†Different models have been implemented depending on the type of application.

phase. For the flowfield simulation, the SINA is used. This code not only has the capability to simulate viscous flows using Navier-Stokes equations but it also can be used for thermal and chemical non-equilibrium flows. Since the entry velocity for Mars is hypersonic, the thermal and chemical non-equilibrium of the flows have to be taken into account. Modifications in the code are made in such a way that all gaseous flow information, i.e. species composition, grid info, reaction scheme etc. required by the code are moved to input data files. The solvers implemented in the code are loosely coupled with each other. This type of coupling provides the liberty to introduce different modules in the code without any problem. The new CVE-solver (Chemical, Vibration and Electron) developed are also presented and discussed.

Chapter 3 lays down all relevant details about the development of the CVE solver to simulate Martian atmosphere. The major constituent of this atmosphere is carbon dioxide (CO_2) which is present around (95.3%). Small amounts of other species are also present, but only in a very small quantity and can usually be neglected, therefore only CO_2 is taken as a flowfield medium. CO_2 is a three atomic molecule and it has three modes of vibration. However previously in the SINA code there was no provision to take into account vibrational energies for the three atomic molecule. The necessary modifications in the code are made and capabilities of the code are enhanced in order to simulate vibrational energies of molecules having three atoms.

Chapter 4 is dedicated to address the solid particles simulation in high temperature gas flows. The Lagrangian approach is used for the particle phase simulation because it involves a small number of empirical equations and is more suitable for providing detailed information on discrete phase than the other approaches. Not only one-way coupling (gas influence onto the particle) but also two-way coupling (the effect of the particles onto the gas) is taken into account. During the development of this solver, the attempt was made to develop this solver as general as possible so that it could be used for other two-phase flow problems. Therefore, depending on the type of problem, different models are developed for the injection of the particles into the flow field. The particle-wall interaction is also discussed and different models being implemented in the code are presented.

Verification and validation are the primary means to assess accuracy and reliability in computational simulations by comparison with known solutions and is centered on the accumulation of evidence that a specific calculation is correct and accurate. Therefore, in chapter 5 verification and validation is done for all new solvers being implemented in the code. For the comparison of the flowfield solver for the Martian atmosphere, CEA (Chemical Equilibrium with Applications) program developed by NASA is used.

1. INTRODUCTION

This is one of the best code for determination of chemical equilibrium of all species of a composition for various ranges of temperatures. The Navier-Stokes code TINA of Fluid Gravity Engineering ltd. and DS2V (a DSMC code) are used in order to verify the particle solver SINA.

The particle behavior when introduced during hypersonic entry flows are studied in chapter 6. A parametric analysis is made by varying the particle initial conditions in the flowfield. The particle trajectories and influence of high temperature gas onto the particles is studied under different conditions. The continuous injection of the particles is also made in order to see the impact on the vehicle surface due to impingement of these particles. The heat fluxes due to hitting of the particles are also computed and presented. Using the two-way coupling, the effect of the particles on the gaseous phase is also addressed.

The summary and conclusion are provided in the last chapter i.e. chapter 7. The development and implementation of the Martian atmosphere and the particle solver are presented and discussed concisely. The conclusions made on the basis of the results obtained from the particle simulation in the Martian atmosphere are also listed.

Chapter 2

Flow Field Solver, SINA

For the flow field solver, the program system SINA is used. It was developed at IRS in order to numerically simulate the complex thermal and chemical phenomena in the plasma wind tunnel facilities at IRS [19]. SINA consists of different independent semi-implicit and explicit solvers which are loosely coupled [20]. Taking advantage of the loose coupling between the solvers, the capabilities of SINA are not only extended [21] to simulate gases other than air such as H_2, CO_2 etc., but also for two-phase flow applications such as aluminum particles in solid rocket motors or dusty plasma flows. For this purpose, major modifications in the program system SINA were required. The main limitation of the code was that it can simulate only air flows on basis of eleven species model[*] N_2, O_2, NO, N, O, N_2^+, O_2^+, NO^+, N^+, O^+, e^- and was mostly hard coded[†]. Therefore, the first and foremost task was to make the code more flexible in such a way that it should be independent of any gas or species information. All these information is now provided by input files.

2.1   Structure of the program system SINA

SINA was developed for plasma flows that are partially in thermal and chemical non-equilibrium. The different solvers (i.e. Navier-Stokes, chemical ,particle etc) are employed in this code which are loosely coupled. This leads to a more flexible, modular structure of the code and different solvers can be employed with moderate effort. In addition to the

---

[*]Park's air model consisting of 11 species

[†]Hard coding refers to the software development practice of embedding input or configuration data directly into the source code of a program, or fixed formatting of the data, instead of obtaining that data from external sources.

27

simulation of hypersonic plasma flows in thermal and chemical non equilibrium, the code can also be employed for two-phase flow problems or electric discharge in plasma flows*.
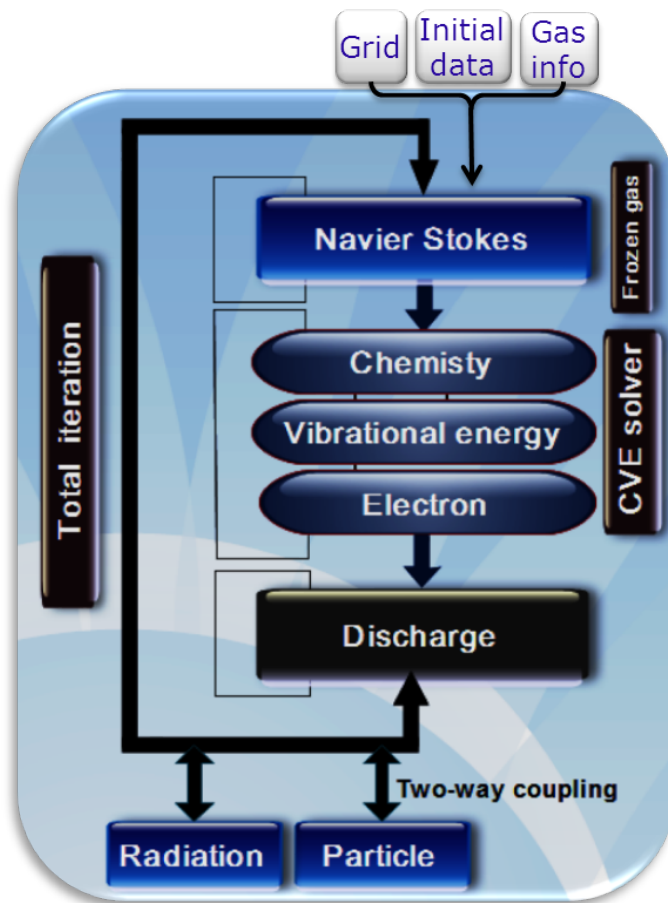

Figure 2.1: Loosely coupled iteration scheme of the program system SINA

The iteration scheme of the loosely coupled program system SINA is shown in figure 2.1. The SINA code consists of different solvers that are explained as followings:

- The first solver within this loop computes the flowfield with the assumption of a frozen flow. This so called Navier-Stokes solver accounts for total mass, total momentum and total energy conservation according to the Navier-Stokes equations.

- The second solver includes the equations that are necessary to describe the real gas effects: the chemical reactions, the equations for vibrational energy of the molecules

---

*Yet to be implemented

and an electron energy balance equation. While this so called CVE*-solver runs, the conserved quantities from the first solver are kept untouched.

- The third solver, which is the last within one total iteration loop, solves the discharge equation of an electric arc and delivers the source terms for the energy conservation equation and the momentum conservation equation of the first solver for the next total iteration loop. (This solver is not yet adapted to the changes in the first two solvers and its development is in progress) [21].

- The fourth solver is used for two phase flow simulations. It is named particle solver. It can be used with the flowfield solvers in two ways, depending upon the type of the coupling i.e. one-way or two-way. For one-way coupling, it is used after the above three solvers have converged to a steady state solution of the flowfield. The Navier-Stokes equations provide a solution to the transport problem over a fixed computational grid while the particle model uses the Lagrangian equations. However, if the volume fraction of the disperse phase is relatively higher (explained in section 4.1), then two-way coupling is essential. Here due to the particles, the changes in mass, momentum and energy terms are again included as additional source terms in the flowfield solver equations.

- To calculate the radiative heat transfer from the gas, the SINA code will be loosely coupled to PARADE†(PlasmA RAdiation DatabasE) [22] and HERTA‡(High Enthalpy Radiation Transport Algorithm) [23].

2.1.1 Flowfield solver

In order to obtain solutions of the flowfield between the bow shock wave and the surface of a vehicle traveling at hypersonic speeds, it is necessary to develop the governing equations of motion and the appropriate flow models. For the development of the basic governing equations, the flow is assumed to be a continuum. This solver provides the solution for the mass, momentum and energy conservation equations.

Generally on the left hand side of the conservation equation, the time rates of the conservative equations are written. On the right hand side, the convective and viscous fluxes as well as the source terms are provided. Therefore, this equation has the following general form:

---

*Chemical, Vibration and Electron energy conservation
†This program calculates the spectral distribution of electromagnetic radiation from the gas.
‡It is a Monte Carlo program that calculates radiation transport.

$$\frac{\partial \vec{X}}{\partial t} = \vec{v}\nabla\vec{X} + \vec{F} + \vec{S}, \tag{2.1}$$

where $\vec{X}$ represents the solution vector, the convective fluxes are expressed by $\vec{v}\nabla\vec{X}$, $\vec{F}$ is used for viscous fluxes and $\vec{S}$ stands for source terms. This time-dependent form of the conservation equations describe the time-dependent processes. In the present study, however, only the steady state are considered and calculated.

2.1.2 Navier-Stokes equations

For the description of the three-dimensional axisymmetric, viscous and chemically reacting flow the following form of the Navier-Stokes equations for the finite volume method in Cartesian coordinates has been used [19]. The first terms on the left hand side of the equations 2.2, 2.3, 2.4, 2.5 and 2.6 represent time rates of change of the conserved quantities (total density, momentum and total energy) while the second term includes the changes on the basis of convective fluxes. On the right hand side of these equations different source terms are involved depending on each type of equation.

- Mass conservation

$$\frac{\partial}{\partial t}\rho + \nabla\rho\vec{v} = \underbrace{M_{evp,2way}}_{\text{particle}} \tag{2.2}$$

- Momentum conservation in x-direction

$$\frac{\partial}{\partial t}\rho u + \nabla\rho u\vec{v} = -\frac{\partial p}{\partial x} + \frac{\partial \tau_{xx}}{\partial x} + \frac{\partial \tau_{xy}}{\partial y} + \frac{\partial \tau_{xz}}{\partial z} + j_y B_z - j_z B_y + \underbrace{F_{x,p,2way}}_{\text{particle}} \tag{2.3}$$

- Momentum conservation in y-direction

$$\frac{\partial}{\partial t}\rho v + \nabla\rho v\vec{v} = -\frac{\partial p}{\partial x} + \frac{\partial \tau_{yx}}{\partial x} + \frac{\partial \tau_{yy}}{\partial y} + \frac{\partial \tau_{zz}}{\partial z} + j_z B_x - j_x B_z + \underbrace{F_{y,p,2way}}_{\text{particle}} \tag{2.4}$$

- Momentum conservation in z-direction

$$\frac{\partial}{\partial t}\rho w + \nabla\rho w\vec{v} = -\frac{\partial p}{\partial x} + \frac{\partial \tau_{zx}}{\partial x} + \frac{\partial \tau_{zy}}{\partial y} + \frac{\partial \tau_{zz}}{\partial z} + j_x B_y - j_y B_x + \underbrace{F_{z,p,2way}}_{\text{particle}} \tag{2.5}$$

- Energy conservation

$$\frac{\partial}{\partial t}\rho e_t + \nabla H_t \vec{v} = \nabla \lambda \nabla T + \sum_{r=mol} \nabla \lambda_{v,r} \nabla T_{v,r} + \nabla \lambda_e \nabla T_e$$
$$+ \frac{\partial}{\partial x}(u\tau_{xx} + v\tau_{xy} + w\tau_{xz}) + \frac{\partial}{\partial y}(u\tau_{yx} + v\tau_{yy} + w\tau_{yz})$$
$$+ \frac{\partial}{\partial z}(u\tau_{zx} + v\tau_{zy} + w\tau_{zz}) + \nabla \sum_{i=1}^{zs} \vec{j}_i h_i \qquad (2.6)$$
$$+ \frac{j^2}{\sigma} + \vec{v}(\vec{j} \times \vec{B}) - \nabla \vec{q}_r + \underbrace{E_{p,2way}}_{\text{particle}}$$

where the viscous terms τ_{ij} represent [24]

$$\tau_{xx} = 2\mu \frac{\partial u}{\partial x} - \frac{2}{3}\mu \nabla \vec{v}$$
$$\tau_{yy} = 2\mu \frac{\partial u}{\partial y} - \frac{2}{3}\mu \nabla \vec{v}$$
$$\tau_{zz} = 2\mu \frac{\partial u}{\partial z} - \frac{2}{3}\mu \nabla \vec{v}$$
$$\tau_{xy} = \tau_{yx} = \mu\left(\frac{\partial u}{\partial y} + \frac{\partial v}{\partial x}\right) \qquad (2.7)$$
$$\tau_{xz} = \tau_{zx} = \mu\left(\frac{\partial u}{\partial z} + \frac{\partial w}{\partial x}\right)$$
$$\tau_{yz} = \tau_{zy} = \mu\left(\frac{\partial v}{\partial z} + \frac{\partial w}{\partial y}\right)$$

The variables τ_{xy}, τ_{zy} etc are used to denote the shear stresses and τ_{xx}, τ_{yy} and τ_{zz} are used to express the normal viscous stresses which are related to velocity gradients in the flow via equation 2.7.

On the right hand side of mass conservation equation 2.2, there is no source term from the flowfield because the overall mass flow due to diffusion and the net rate of production of all species is zero. However $M_{evp,2way}$ is included in this equation as a source term from the particle solver. This term is added here because of the two-way coupling effect and represents the mass lost by the particles if these are heated enough that evaporation of the particles takes place. In this case mass loss of the particles will be added up in the mass of the gas. In the momentum conservation equations 2.3, 2.4 and 2.5 the terms on the right hand side include both the pressure forces and viscous forces acting on a surface in a space (both of which are surface forces). The pressure calculation is based on Dalton's law of partial pressure:

2. FLOW FIELD SOLVER, SINA

$$p = \sum_{i=1}^{zs} (n_i k T) + n_e k T_e, \qquad (2.8)$$

where p is the pressure, n is the number density and T represents temperature. On the right hand side of the momentum equations the terms $F_{x,p,2way}$, $F_{y,p,2way}$ and $F_{z,p,2way}$ are included as source terms of momentum exchange from the particle solver in order to take into account the effect of two-way coupling. On the left hand side of the energy conservation equation 2.6 the conserved quantity and total enthalpy are presented. The total enthalpy (volume specific) is represented by the equation $H_t = \rho e_t + p_t$. On the right hand side of this equation, the first three terms represent conduction of energy over the cell walls due to temperature gradients. The 4th to 6th terms are the source terms of viscous fluxes. The effective diffusion of the individual components also causes a transport of energy, which is modeled in the seventh term. The 8th and 9th term appear only in the modeling of the plasma source including electric discharge. The 10th term is about the volumetric heating that might occur, by the absorption or emission of radiation by the gas. The last term is the source term of the particle solver in order to account for two-way coupling effects. This is the amount of the energy in the form of convective heating that particles have given back to the gas.

The volume specific total energy in thermal and chemical non equilibrium is the sum of kinetic, translational and latent energies of the heavy particles and electrons, vibrational and rotational energies of the molecules and mathematically presented as:

$$
\begin{aligned}
\rho e_{tot} = {} & \frac{1}{2} \rho v^2 + \sum_{\substack{i=1 \\ i \neq e^-}}^{zs} \rho_i \Big(\frac{3}{2} R_i T + h_{0,i} \Big) \\
& + \rho_e \Big(\frac{3}{2} R_e T_e + h_{0,e} \Big) + \sum_{j=1}^{n_{mol}} \rho_j e_{vib,j} + \sum_{k=1}^{n_{mol}} \rho_k e_{rot,k},
\end{aligned}
\qquad (2.9)
$$

where e_{tot} represents total energy, h_0 is the standard enthalpy and e_{vib} & e_{rot} are used to express vibrational and rotational energies respectively.

For the inviscid flux calculations an AUSM+ scheme with 2nd order reconstruction of MUSCL-type a TVD limiter of van Albada(briefly presented in B) and for the viscous fluxes a central difference scheme is employed. The time integration is performed by an explicit 4-step Runge Kutta scheme [25]. The transport properties are determined via the simplified model of Yos [26] or with a Chapman-Cowling formula [27]*. The data for the

---

*Depending on the nature and complexity of the problem, any model from these two can be selected.

transport coefficients depends on the type of the flowfield gas. For example for air it is taken from Yos, Gupta et al [28; 29] and for CO_2 from Wright [30].

2.2 CVE-solver in SINA

Subsequently to the computation of the flowfield by the first solver, the CVE-solver (Chemical, Vibration, Electron) is called. This solver accounts for the chemistry, vibrational and electron energy conservation. It has the capability to simulate chemical and thermal non-equilibrium flows. The chemical composition of the gas is also determined by the CVE solver. This solver was originally developed for the 11 component air model of Park [31]. With the recent modifications*, it is rebuilt more flexible using external files for the definition of the reaction scheme in order to expand the range of applications of SINA to hydrogen driven electric plasma sources or Martian atmosphere entry simulation, to name just a few.

The wide temperature range from ambient up to about 50,000 K and a pressure from hPa up to the MPa range represents a great challenge for the modeling of transport coefficients. For the computation of non equilibrium reacting flows, the rotational temperature is considered to be equal to heavy particle translational temperature T because it tends to equilibrate very fast with translational temperature. Electron temperature T_e deviates from heavy particle translational temperature T because of the slow rate of energy transfer between electrons and heavy particles. This temperature is determined through its energy distribution. The vibrational temperature T_v departs from both electron temperature T_e and heavy particle translational temperature T because of the slow equilibration of vibrational energy with electron and translational energies. The vibrational temperature of the neutral molecules is computed from their respective vibrational energies and for all the ionized molecules, the average temperature of the neural molecules is considered.

2.2.1 Physical model of the CVE solver

Not only new subroutines for the calculation of the thermal and chemical non equilibrium have been added, but also a new solver using a semi implicit-Euler method to solve stiff equations of convective fluxes and chemical source terms is developed. Additionally an Euler time stepping is provided for stability. At the same time the whole chemistry part

---

*In cooperation with Uwe Bauder, a PhD student in IRS, Universität Stuttgart, Germany

2. FLOW FIELD SOLVER, SINA

of SINA has been transferred from a 2D rotational symmetric finite difference formulation to a 3D finite volume formulation with boundary conditions for rotational symmetry.

The vibrational energy equation and the electron energy equation describe the thermal non-equilibrium. The vibrational temperatures and the electron temperature are derived from the resulting vibrational energies and electron energy. The chemical composition is determined by solving the balance equations

$$\frac{\partial}{\partial t}c_i = \nabla c_i \vec{v} + w_i + \nabla \sum_{i=1}^{zs} \vec{j}_i \qquad (2.10)$$

for the molar concentration c_i of each species. Here, the first term on the right hand side is the convective transport, followed by the rate of production w_i and the term for the diffusion of the components. The rate of production is given by

$$w_i = \sum_{j=1}^{m} (\nu''_{ij} - \nu'_{ij}) \left[k_{fj(T,T_e,T_{vib})} \prod_k c_k^{\nu'_{kj}} - k_{bj(T,T_e,T_{vib})} \prod_k c_l^{\nu''_{lj}} \right], \qquad (2.11)$$

where the summation is done over all m reactions. The stoichiometric coefficients are ν'_{ij} for the forward reaction j of the species i and ν''_{ij} for the backward reaction. Accordingly, the rate coefficients are k_{fj} for the forward reaction j and k_{bj} for the backward reaction. They are computed employing the rate constants and the equilibrium constants. The molar concentrations are transformed back to number densities after determination of the new chemical composition .

The second part of the CVE-solver accounts for the vibrational temperatures of the uncharged molecules. This is done by solving the balance equation for the vibrational energy

$$\frac{\partial}{\partial t}E_{v,r} = \nabla E_{v,r}\vec{v} + \nabla \lambda_{v,r} \nabla T_{v,r} + \nabla \sum_{i=1}^{zs} \vec{j}_i + Q_{c-v,r}$$
$$+ Q_{t-v,r} + Q_{v-v,r} + Q_{e-v,r}. \qquad (2.12)$$

where E_v is the vibrational energy, λ is used for thermal conductivity and Q_{c-v}, Q_{t-v}, Q_{v-v}, Q_{e-v} represent energy exchange between chemical, translational, vibrational and electronic modes. Thus, the change of vibrational energy in time is caused by convective transport, vibrational heat conduction, diffusion, energy gains or losses due to chemical reactions, coupling between vibrational and translational energy, relaxation processes between the vibrating molecules and by the coupling between vibrational and electron energy. Assuming a harmonic oscillator model, the resulting vibrational energy leads directly to the vibrational temperatures.

The last part of the CVE-solver is responsible for the solution of the electron energy balance equation

$$
\begin{aligned}
\frac{\partial}{\partial t} E_e = {} & \nabla H_e \vec{v} + \nabla \lambda_e \nabla T_e + \nabla \sum_{i=1}^{zs} \vec{j_i} \\
& - \sum_{s=ion} Q_{e-v,s} - \sum_{r=mol} \frac{M_r}{M_e} \frac{E_{v,s} - E_{v,r}}{\tau_{e-r}} \\
& + 3 m_e n_e k (T - T_e) \sqrt{\frac{8kT_e}{\pi m_e}} \sum_{i \neq e} \frac{n_i}{m_i} \sigma_{e,i} - \nabla \vec{q_r} + \frac{j^2}{\sigma},
\end{aligned}
\tag{2.13}
$$

where E_e is the electron energy, Q_{e-v} represents the energy exchange between chemical and electron energy modes and q_r is used to denote radiative heat fluxes. On the left hand side of this equation the temporal change of electron energy is presented. On the right hand side, this equation accounts for the convective transport, the heat conduction of the electrons, the diffusion and the energy gained or lost during ionization reactions. The fifth term represents the coupling of electrons and vibrating molecules as already seen at the vibrational energy conservation equation. After that, the coupling with the heavy particles' translational energy follows. The last two terms are the source terms for radiation and ohmic heating by an electric discharge, respectively. The electron temperature is derived from the electron energy using

$$
E_e = \frac{3}{2} n_e k T_e.
\tag{2.14}
$$

2.2.2 Energy exchange terms

As the gas particles move through the flowfield, chemical reactions or the exchange of energy among the various modes, e.g., translational, rotational, vibrational, and electronic, of the atoms and of the molecules may occur. The transfer of energy between the various energy modes is accomplished through collisions between the molecules, the atoms, and the electrons within the gas. The accommodation time is determined by the frequency with which effective collisions occur. In a case, where the gas density is low, chemical and thermal states do not necessarily reach equilibrium. Non equilibrium processes occur in a flow when the time required for a process to accommodate itself to local equilibrium conditions within a particular region is of the same order as the time it takes the gas particles to cross that region, i.e., the transit time. If the accommodation time is very short compared to the transit time, the process is in equilibrium. If the accommodation

time is long with respect to the transit time, chemical composition is "frozen" as the flow proceeds around the vehicle.

The energy exchange between the vibrational degree of freedom and other modes of freedom and also with the chemical source terms can be summarized as

$$S_{v,k} = S_{t-v,k} + S_{v-v,k} + S_{c-v,k} + S_{e-v,k}, \tag{2.15}$$

where $S_{t-v,k}$ is the energy transfer between the vibrational and translational degrees of freedom, $S_{v-v,k}$ is the rate of vibrational energy exchange between the vibrational modes of different molecules, $S_{c-v,k}$ is the vibrational energy variation in the process of chemical reactions and $S_{e-v,k}$ is the energy transfer between the electrons and different modes of vibration. Additional energy exchange source terms arise for the exchange of energy between the energy balance equations due to inelastic collision. SINA employs standard models from literature which are mainly of Landau-Teller type, see e.g. Kanne et al. [32] and references therein.

Translational-vibration energy exchange

The model used for calculating the energy exchange between translational and vibrational modes has the Landau/Teller form [32] [33]

$$S_{t-v,k} = c_k \frac{\epsilon_{v,k}^{eq}(T) - \epsilon_{v,k}(T_{v,k})}{< \tau_k >}, \tag{2.16}$$

where $\epsilon_{v,k}^{eq}$ is the molar vibrational energy in equilibrium and $< \tau_k >$ is the average vibrational relaxation time, that it consists of two parts:

$$< \tau_k >= \tau_{k_{MW}} + \tau_{cr}. \tag{2.17}$$

The first part of the relaxation time is based on Millikan and White [34] and is valid up to approx. 5000 K. For its computation, the following correlation is used.

$$\tau_{k_{MW}} = \frac{\sum_{s=1}^{n_{mol}} c_r}{\sum_{s=1}^{nmol} \frac{c_r}{\tau_{ksMW}}} \quad \text{where } \tau_{ks_{MW}} = \frac{1}{p. \left[A_{rs} \left(T^{-1/3} - 0.015 \mu_{rs}^{1/4} \right) - 18.42 \right]}. \tag{2.18}$$

The total pressure p in the equation 2.18 is used in [atm]. The parameter A_{rs} and reduced molar mass μ_{rs} is calculated using the relation

$$A_{rs} = 1.16 \times 10^{-3} \mu_{rs}^{1/2} \theta_r^{4/3} \quad \text{and} \quad \mu_{rs} = \frac{M_r M_s}{M_r + M_s}. \tag{2.19}$$

At higher temperatures the relation provided by Millikan and White gives wrong results. Park [33] introduced a correction term in the relaxation time that is given as:

$$\tau_{cr} = \frac{1}{v_r \sigma_v n_{tot}} \quad \text{where} \quad \sigma_v = 10^{-21} \cdot \left(\frac{T}{50000}\right)^2. \tag{2.20}$$

The average particle velocity of the molecular species r is computed by $\bar{v}_r = \sqrt{\frac{8\Re T}{\pi M_r}}$ and n_{tot} is the total density of the gas.

Vibration-vibration energy exchange

The equation used for the vibration-vibration exchange is

$$S_{v-v,k} = \sum_{t \neq k}^{mol} \left[P_{r,k} N_A \sigma_{k,t} \sqrt{\frac{8\Re T}{\pi \mu_{k,t}}} \frac{\rho_k \rho_t}{M_t} \left(\frac{e_{v,t} e_{v,k}^{eq}}{e_{v,t}^{eq}} - e_{v,k} \right) \right]. \tag{2.21}$$

where $P_{r,k}$ are the exchange probabilities and it is calculated from Rapp [35]

$$P_{r,k} = 3.7 \times 10^{-6} \; T_{vib,r} \frac{1}{\left[cosh\left(0.1208(\theta_r - \theta_s)\right) \right]^2}. \tag{2.22}$$

Chemical-vibration energy exchange

For determining the energies of the reacting species it is distinguished between formation and decomposition reactions and between the energy of decomposing (vanishing: index va) and forming (appearing: index app) species. If a particle is formed according to the generic reaction equation 2.26 from left to right, the species appears in the forward reaction and its energy depends on the energies of the starting substances on the left. The decomposition of the species occurs in the backward reaction. Hence, the starting substances are on the right, i.e. the energy of the decomposed species depends on the temperatures of the species on the right side of the equation. This can be expressed by

$$\nu > 0 \begin{cases} \dot{\omega}_{app,i} = \quad \nu_i \dot{\omega}_f, \; E_{app,i} = E(i, T_L) \\ \dot{\omega}_{va,i} = \; - \nu_i \dot{\omega}_b, \; E_{va,i} \quad = E(i, T_R) \end{cases} \tag{2.23}$$

for a formation reaction, where the indices L and R denote left and right side of the reaction equation 2.26, respectively. Similarly, one obtains

$$\nu < 0 \begin{cases} \dot{\omega}_{app,i} = \quad \nu_i \dot{\omega}_b, \; E_{app,i} = E(i, T_R) \\ \dot{\omega}_{va,i} = \; - \nu_i \dot{\omega}_f, \; E_{va,i} \quad = E(i, T_L) \end{cases} \tag{2.24}$$

for a decomposition reaction. Given the mean molar energy of the forming and decomposing species, the chemical-vibrational exchage energy source term can be expressed by

$$S_{c-v,k} = \sum_{r=1}^{z_r} \dot{\omega}_{app,i,r} E_{int,app,i,r} - \dot{\omega}_{va,i,r} E_{int,va,i,r}. \tag{2.25}$$

2.2.3 Chemical source terms

A mixture of gases at a point is in local thermal equilibrium when the internal energies of each species form a Boltzmann distribution for the heavy-particle translational temperature T across each of their respective energy spectra. However, when the distribution of vibrational energies does not fit the Boltzmann distribution for temperature T, thermal non equilibrium effects are present at that point. There is also a model with two temperatures T and T_e, which is more often refer to as a two-temperature model. For the two-temperature model, the distribution of vibrational energies still forms a Boltzmann distribution but at a different temperature T_v. Thermal equilibrium exists when $T = T_v$.

A mixture of gases at a point is in local chemical equilibrium when the chemical species concentrations at that point are a function of the local pressure and of the local temperature alone. Chemical equilibrium occurs when the chemical reaction rates are significantly faster than the time scales of the local fluid motion, so that the species conservation equations reduce to a balance between production and destruction of the species due to chemical reactions. If the effects of convection and of diffusion affect local species concentrations, the flow is in chemical non equilibrium.

Combining these two definitions, the conditions for local thermochemical equilibrium can be defined at a point in the flowfield. The characteristic time scales for the fluid motion, the vibrational relaxation process, and the chemical reactions are denoted by t_f, t_v and t_c , respectively. Thermal equilibrium requires $t_v << t_f$, everywhere. Similarly, chemical equilibrium requires $t_c << t_f$.

In general, species balance equations have to be solved if the relaxation time of chemical reactions is in the same order or greater than the flow residence time in the volume cells, i.e. if the assumption of chemical equilibrium is not justified. The number of species balance equations depends on the definition of the species. It is possible to solve species equations for each quantum state of the chemical species under consideration, see e.g. [36]. The disadvantage of such a model is that a vast number of species equations results

which leads to unacceptable computing time even for two dimensional flow problems. Therefore, the CFD schemes usually distinguish only between chemical species.

An arbitrary chemical reaction can be formulated by

$$\sum_{i=1}^{z_s} \nu_i' X_i \underset{k_b}{\overset{k_f}{\rightleftharpoons}} \sum_{j=1}^{z_s} \nu_j'' X_j, \tag{2.26}$$

where X is a placeholder for the species under consideration. The reaction rate can be obtained from the forward reaction rate coefficient k_f and the backward reaction rate coefficient k_b. The multiplication factors ν_{ij}' and ν_{ij}'' are the stoichiometric coefficients of the sources and the products, respectively. The speed of the forward and backward reaction rates depends on the reaction rate coefficients k_f and k_b. The reaction rate is proportional to the concentration c_i of the source/reactant species. With the reaction rate coefficients the reaction rates can be expressed by

$$\dot\omega_f = k_f \prod_{i=1}^{z_s} c_{X_i}^{\nu_i'} \qquad \text{and} \qquad \dot\omega_b = k_b \prod_{i=1}^{z_s} c_{X_i}^{\nu_i''} \tag{2.27}$$

for a forward and a backward reaction, respectively. It was an experimental finding that the reaction rate constants

$$k \propto e^{-\frac{A}{RT}} \tag{2.28}$$

are independent from composition and depend exponentially on the inverse of temperature. The constant A which is usually given in $\frac{kJ}{mol}$ is called activation energy in case of exothermic reactions. For the determination of the reaction rates it is useful to introduce the general stoichiometric coefficients

$$\nu_{ij} = \nu_{ij}'' - \nu_{ij}', \tag{2.29}$$

and the effective reaction rate

$$\dot\omega_{eff} = \dot\omega_f - \dot\omega_b. \tag{2.30}$$

The chemical source term of the species

$$\dot\omega_i = M_i \sum_{r=1}^{z_r} \nu_{i,r} \dot\omega_{eff,r}, \tag{2.31}$$

is obtained from the stoichiometric coefficients and the reaction rates by summation of all reactions and multiplication with the species' molar mass.

2.2.4   Numerical model

As we are dealing with very stiff equation, the time step taken for the explicit Euler method may be very small that will result in very slow convergence. In order to get rid of this problem, the semi-implicit Euler method is used. It is called semi-implicit because it involves derivatives of the source terms. For the numerical model, the right hand side of equation 2.1 can be written as $\dot{\vec{X}}$ which represents the rate of change $\frac{\partial}{\partial t}\vec{X}$ computed by SINA. This method can be presented by the equations

$$\left[\frac{1}{\Delta t}I_{mt} - \left\{\partial\dot{\vec{X}}/\partial\vec{X}\right\}\right]\Delta X = \dot{\vec{X}}^n, \tag{2.32}$$

$$\vec{X}^{n+1} = \vec{X}^n + \Delta X, \tag{2.33}$$

that determines a new $\vec{X}^{n+1}$ so that $\dot{\vec{X}}$ is zero. Here, the vector $\vec{X}$ represents the solution variables. From the equation 2.32 it is clear that as the time step reaches ∞, this will reduces to Newton implicit equation and at time zero, we will get the explicit Euler equation. The drawback of this method is that the derivatives of $\dot{\vec{X}}$ are needed. The derivatives of the chemical source terms are determined analytically because these source terms are very stiff in nature. The derivatives are for all the other terms appearing on the right hand side of the equations 2.10, 2.12, 2.13 and 2.14 are determined numerically. The reason for using the numerical derivations is their simplicity to model and implement in the code and results obtained are in a acceptable accuracy. The equation system that appears in the equation 2.32 is solved using LU decomposition of the matrix based on a variant of Gaussian elimination algorithm.

Step size control

Due to very stiff equations, the solution may become unstable, therefore a step size controls is provided in order to stabilize the solution and to avoid instabilities. As explained before that the code is designed in such a way that it could be used to simulate reentry flows into the atmosphere consisting of any type of gases. Therefore the chemical solver should be robust enough that no matter how stiff the differential equations are, it should have the capability to deal them properly.

An adapted time stepping algorithm [37] [38] is implemented in the code after testing different constraints and time stepping techniques. The first thing involving the step size control is to establish the error estimation criteria, because the magnitude of the error

from the previous time step will lead to define the next step size. The error ratio is estimated using the equation

$$q_{err} = \frac{\varepsilon_h}{\epsilon_\rho}, \tag{2.34}$$

where ε_h is the error emerged due to the time stepping and ϵ_ρ limits the maximum allowable variation in the partial densities of the species and species energies.

The ε_h is based on the estimation of local error by evaluating a difference in solutions obtained when a full-step and half-step is used. This technique is very useful for step length adjustment. At each selected step length, the code is first run by using the full step length. Next, the same case is performed in two steps of length $\frac{h}{2}$. The absolute error is then calculated by

$$\varepsilon_h = |\Delta x(h) - 2\Delta x(\frac{h}{2})|. \tag{2.35}$$

The tolerance ϵ_ρ is provided for the the partial densities by taking into account maximum allowable changes in the total density of the gas. The ϵ_ρ is determined using the correlation

$$\epsilon_\rho = \max(\varrho_1 \vec{X}, \varrho_2 \rho), \tag{2.36}$$

where ϱ_1 is the factor by which the limiting value of the total density is set and ϱ_2 is the minimum tolerance in the partial densities. The values of ϱ_1 and ϱ_2 must be carefully tested and set. These values may vary depending upon the stiffness of the equation and convergence of the solution. In general, the strategy is to increase the time step if the error is small and decrease it if the error is too large. The ϵ_ρ defines the criteria for the time stepping for the chemical solver and is presented in the equation 2.37.

$$
\begin{aligned}
\varepsilon_h < \epsilon_\rho \qquad &\Longrightarrow \qquad \text{solution accepted} \\
\varepsilon_h > \epsilon_\rho \qquad &\Longrightarrow \qquad \text{solution not accepted}
\end{aligned}
\tag{2.37}
$$

The relative increase or decrease in the values of h (time step) are also flexible and may vary depending upon the type of the problem under consideration. As shown in the equation 2.37, for the cases where $\varepsilon_h > \epsilon_\rho$ the result is not accepted and the computation is repeated with the half control step $h/2$. The advantage of doing half step computation is that only one computation is needed because the new computation needed for the full control step h is available from the previous run. However, for increasing the time step, a special care has to be taken because in order to avoid large oscillation and slow

convergence. The solution my be destabilized if the time step is increased to very high values but at the same time the step size should not be so small that it may hinder the convergence and performance of the solver. Once a step is accepted, the proposed step length for the next step is chosen as

$$h = \frac{h}{\min\left[(4q_{err})^{-0.25}, 3\right]},$$
(2.38)

permitting an increase in h when $q_{err} < 0.25$ and possibly an acceleration by a factor of 3 when $q_{err} << 1$. The factor of 4 in equation 2.38 and the empirical restriction on the maximal increase were used as safety margins to avoid selection of too large steps that might be rejected (that is, lead to q_{err} values larger than 1).

This is worthy to mention here that this numerical method is not optimized. For very stiff problems it is very time consuming and convergence is relatively slow. Therefore for future extension of the code, it is recommended to implement other numerical methods like two-step diagonally implicit Runge Kutta method (DIRK2) etc. for the robustness and better convergence of the code.

Chapter 3

CO$_2$ Solver Implementation

As a result of intense future exploration missions to Mars, new and thorough studies on flow dynamics, chemical kinetics, thermal non-equilibrium, and radiation of high-temperature gases present in the shock layer of any space vehicles entering the Martian atmosphere are necessary in order to evaluate both the convective and the radiative heating to the surface of the vehicles. The Martian atmosphere consists mainly of carbon dioxide (95.3%), molecular nitrogen (2.7%) and argon (1.6%)[39]. Small amounts of other species are also present, but can usually be neglected.

The flowfield about the orbiter entering a planetary atmosphere is indeed complex. Its analysis requires the simultaneous treatment of a three-dimensional, non-steady and non-equilibrium viscous flow. In order to cope with such a complex assignment, it is necessary to make several simplifying assumptions reducing the physical modeling to a manageable task. First, the flowfield about the orbiter is modeled as symmetric around the axis of the orbiter. Then, the Mars atmosphere composition is reduced to pure CO$_2$.

The entry velocity of past missions in the Martian atmosphere is depicted in the table 3.1. Minimum energy flight trajectories from Earth to Mars result in a Martian entry velocity of 5-7 km/s or slightly higher [40]. Such a flight trajectory requires a one-way mission time of nearly one year. For a manned mission, such a long journey is undesirable. A fast mission is possible using a high-energy trajectory, but such fast missions result in a higher entry velocity. The compromise between the mission time and the entry velocity leads to a scenario requiring a one-way flight time of 5-8 months, and an entry velocity between 7-9 km/s [40].

Table 3.1: Entry velocity of past missions in Martian atmosphere

Flight	Agency	Entry Date	V_{rel} (km/s)
Mars 2	RSA	Nov.27,1971	6.0
Mars 3	RSA	Dec.2,1971	5.7
Mars 6	RSA	Mar.12,1974	5.6
Viking I	NASA	Jul.20,1976	4.5
Viking II	NASA	Sep.3,1976	4.5
Pathfinder	NASA	Jul.4,1997	7.5
MPL	NASA	Dec.3,1999	6.9
DS-2	NASA	Dec.3,1999	6.9
Beagle	ESA	Dec.25,2003	5.6
MER-A	NASA	Jan.3,2004	5.6
MER-B	NASA	Jan.24,2004	5.6
Phoenix	NASA	Aug.4,2007	5.5

3.1 Chemical modeling

As explained before, the entry velocities to Mars are approximately 5-7 km/s. For such velocities, the gas in the shock layer is expected to be highly reactive. The computations of the flowfield are then done considering that the gas is composed of a mixture of CO_2 products that are vibrationally excited and chemically reacting. Keeping in view the entry velocities, the ionization can be ignored as the expected maximum temperature of the considered flow is less than 8000 K [41]. Moreover, no turbulence models are taken into account, and therefore the obtained results correspond to a laminar flow. Solving this limited model is still a challenge.

The dissociation of CO_2 starts at about 1800 K (at 7.87 Pascal pressure[*]). Keeping in view the fact that ionization is not taken into account and entry velocity in the Mars atmosphere is around 5-7 km/s, the five species model (carbon dioxide (CO_2), molecular oxygen (O_2), carbon monoxide (CO), oxygen (O) and carbon (C)) from Charbonnier [42] is decided to be used[†]. The other advantage of using this model, is to allow for a

---

[*]The entry pressure for MSRO mission in Martian atmosphere

[†]In case of higher entry velocities a more detailed model that includes ionization(such as [39]) may also be used.

fair comparison with published results based on this chemistry modeling and to avoid introducing additional bias when comparing simulated data.

A 18 reactions scheme for the chemistry set is shown in table A.1 from Charbonnier[42]. The chemical equilibrium constant is determined based on the the Gibbs free energy method. The data required for the determination of the chemical equilibrium constant is taken from the CEA NASA Thermobuild Table [43]. The data required for the computation of standard enthalpy and entropy is provided in table A.2. However the detailed output of the data can be taken from [43] if needed. The determination of reaction rate and equilibrium constants is explained in detail in sections 3.1.1 and 3.1.2 respectively.

3.1.1 Reaction rate coefficients

The excitation of internal degrees of freedom reduces the activation energy of chemical reactions. An established ansatz for determining the reaction rate constants is the extended Arrhenius law

$$k(T) = C \cdot T^s e^{\frac{-A}{RT}}, \tag{3.1}$$

where C and s are constants. The constant s mainly accounts for the influence of temperature on collision frequency. From measurements the reaction rate constants in thermal equilibrium have been evaluated. In order to account for the influence of internal excitation within a multi-temperature model the reaction rate constants have to be determined as a function of the translational and the vibrational temperatures. Currently in the code a model developed by Park [44; 31] for coupling the internal energies i.e. vibration is implemented. Parks $T\,T_{vib}$ model for the determination of the reaction rate constants can be represented by

$$k(T, T_v) = CT^{(s-r)}T_{vib}^r e^{-\frac{A-A^*}{RT} - \frac{A^*}{RT_{vib}}}, \tag{3.2}$$

where A^* and r are modeling parameters which have to be determined from physical considerations. A^* may be interpreted as a part of the activation energy which needs to be exceeded by vibrational energy. It can be easily shown, that the extended Arrhenius equation 3.1 follows for the case of equilibrium between translation and vibration, i.e. $T = T_{vib}$. If T_{vib} is lower than T, the reaction rate constant falls below the equilibrium value. In the opposite case the reaction rate constant exceeds the equilibrium value.

Since Park uses $T_a = T$ for exchange reactions as well as for associative ionization reactions and $T_a = T_e$ for electron impact ionization, SINA employs

$$T_a = T^r T_{vib}^{1-r},$$
(3.3)

to allow for a uniform description of the reaction rates via

$$k_f(T, T_v) = C(T^r T_{vib}^{1-r}) e^{-\frac{A}{\Re T^r T_{vib}^{1-r}}},$$
(3.4)

with $r = \frac{1}{2}$ for dissociation reactions and $r = 1$ for all other.

In chemical equilibrium the forward reaction rate $\dot{\omega}_f$ and the backward reaction rate $\dot{\omega}_b$ are equal. Therefore, equilibrium constant can be defined via

$$K_c = \frac{k_f}{k_b} = \left(\frac{\prod_{i=1}^{z_s} c_{X_i}^{\nu_i''}}{\prod_{j=1}^{z_s} c_{X_j}^{\nu_j'}} \right)_{eq} = \left(\prod_{i=1}^{z_s} c_{X_i}^{\nu_i} \right)_{eq}.$$
(3.5)

The equilibrium constant can be determined with high accuracy both experimentally as well as with the methods of chemical energetics. Data required for the calculation of the equilibrium constants can be found from Cox [45], the NIST database [46] or can be calculated from CEA NASA Thermobuild Table [43]. In contrast to the evaluation of the equilibrium constants the determination of the reaction rate constants is much less accurate. In addition to experimental methods a number of classical, analytical methods for the determination of the reaction rate constants like the collision theory or the transition state theory do exist. In addition, direct numerical methods are employed in recent years, see e.g. [47]. Like forward reaction rate, the backward reaction rate can also be determined from equation 3.4 with little modifications. However, keeping in view the fact that possible errors in the determination of k_f and k_b might lead to wrong computation of equilibrium constant k_c, the backward reaction rate k_b is determined employing

$$k_b = \frac{k_f}{K_c}.$$
(3.6)

3.1.2   Equilibrium constant K_c

As discussed before, Park's TT_{vib} model is currently used in SINA. Originally the Park's model was developed for air only. However, this is general model and does not involve any empirical values or correlation associated with air flows only. Therefore, the same model

is used for the Martian entry flows (CO_2 gas instead of air). The following polynomial fit [48] is used for the computation of equilibrium constant.

$$
\begin{aligned}
K_c(T) = \exp\Bigg(& P_{K,1} + P_{K,2}\ln\left(\frac{T}{1000}\right) + P_{K,3}\left(\frac{T}{1000}\right)^{-1} \\
& + P_{K,4}\left(\frac{T}{1000}\right)^{-2} + P_{K,5}\left(\frac{T}{1000}\right)^{-3} + P_{K,6}\frac{T}{1000} \\
& + P_{K,7}\left(\frac{T}{1000}\right)^{2} + P_{K,8}\left(\frac{T}{1000}\right)^{3} + P_{K,9}\left(\frac{T}{1000}\right)^{4} \Bigg)
\end{aligned}
\tag{3.7}
$$

The values for polynomial coefficients $P_{K,1}$ to $P_{K,9}$ are provided by Park for air. For CO_2, these coefficients have to be determined. For this purpose the standard Gibbs free energy method is used. A measure of the free energy, the potential energy of a reaction, can be used to predict properties of chemical reactions. In the late 1800's, J. W. Gibbs showed that free energy (G) of a system can be defined as

$$
G = H - TS.
\tag{3.8}
$$

in which S refers to the entropy of the system. Since H, T and S are all state functions, so is G. Thus for any change in state, we can write the relation:

$$
\Delta G = \Delta H - T\Delta S,
\tag{3.9}
$$

From basic thermodynamics, it can be derived that:

$$
\delta q = de + p\ dv.
\tag{3.10}
$$

When adding an amount of heat to 1 kg of a gas at constant pressure, the temperature of the gas increases. The relation for the specific heat capacity is

$$
c_p = \frac{\delta q}{dT}.
\tag{3.11}
$$

From equations 3.10 and 3.11, we can write

$$
dH = c_p\ dT.
\tag{3.12}
$$

After integrating we get

3. CO_2 SOLVER IMPLEMENTATION

$$h^0(p, T) = h^0 + \int_{T_0}^{T} c_p \, dT. \tag{3.13}$$

The values of the enthalpy h^0 are based on a function of pressure and temperature. There are different resources/methods available for the determination of these values e.g. [46; 43]. In SINA, the computation of these variables are based on NIST data. In this data the curve fitting coefficients for the large number of atoms and molecules are given. Taking into account these coefficients, the enthalpy of formation using the equation 3.14 is computed.

$$h^0(p, T) \left(\frac{kJ}{mol} \right) = A \left(\frac{T}{1000} \right) + \frac{B}{2} \left(\frac{T}{1000} \right)^2 + \frac{C}{3} \left(\frac{T}{1000} \right)^3$$
$$+ \frac{D}{4} \left(\frac{T}{1000} \right)^4 + E \left(\frac{1000}{T} \right) + F. \tag{3.14}$$

Since entropy is a state variable, it must be uniquely related to other state variables. For a system in equilibrium, entropy can be expressed as a function of T and p, even for calorically or thermally perfect gases where enthalpy and internal energy are functions of temperature only. Using the laws of thermodynamics, the entropy can be defined as [49]

$$dS = c_p \frac{dt}{T} - \Re \frac{dp}{p}. \tag{3.15}$$

Using equation 3.12 and after integrating we get

$$S(p, T) = \underbrace{S^0 + \int_{T_0}^{T} c_p \, dT}_{S^0(p_0, T)} + \Re \, ln(\frac{p_0}{p}). \tag{3.16}$$

For constant pressure of $p_0 = 1atm = 101300pa$ the relation for the entropy is

$$S^0(p_0, T) \left(\frac{J}{molK} \right) = A \, ln \left(\frac{T}{1000} \right) + B \left(\frac{T}{1000} \right) + \frac{C}{2} \left(\frac{T}{1000} \right)^2$$
$$+ \frac{D}{3} \left(\frac{T}{1000} \right)^3 - \frac{E}{2} \left(\frac{1000}{T} \right)^2 + G, \tag{3.17}$$

where the coefficients from A to G are available from NIST database [46] or can be calculated from CEA NASA Thermobuild Table [43]. In order to make use of Gibbs energies to predict chemical equilibrium, one has to determine the free energies of the

individual components of the reaction. Now the standard enthalpy of formation h^0 and the standard entropy of a substance S^0 can be combined using equation 3.9 to get its standard free energy of formation. Then, determination of the standard Gibbs energy of the chemical reaction is followed by the stoichiometric addition of the free energies of the reactants and products

$$\Delta G(p,T) = \underbrace{\sum_{i=1}^{z_s}(\nu_i'' - \nu_i')\Big[H_i(p_0,T) - TS_i(p_0,T)\Big]}_{\Delta_R G} - \sum_{i=1}^{z_s}(\nu_i'' - \nu_i')\Re T \; ln\Big(\frac{p_0}{p_i}\Big). \qquad (3.18)$$

The thermodynamic proof of this equation is complex and therefore not presented here. However it could be found in [50] and [51]. In equilibrium condition ($\Delta G(p,T) = 0$), equation 3.18 can be written as

$$\frac{\Delta_R G^0}{\Re T} - ln\left(\frac{\prod_{i=1}^{z_s}\left(\frac{p_0}{p_i}\right)^{\nu_i''}}{\prod_{j=1}^{z_s}\left(\frac{p_0}{p_j}\right)^{\nu_j'}}\right)_{eq} = 0. \qquad (3.19)$$

The equation for the partial pressure p_i is

$$p_i = c_i\Re T. \qquad (3.20)$$

Using equation 3.20 in 3.19, we get

$$\left(\frac{\prod_{i=1}^{z_s}c_i^{\nu_i''}}{\prod_{j=1}^{z_s}c_j^{\nu_j'}}\right)_{eq} = exp\left[-\frac{\Delta_R G^0}{\Re T} + \sum_{i=1}^{z_s}(\nu_i'' - \nu_i') \; ln\Big(\frac{p_0}{\Re T}\Big)\right]. \qquad (3.21)$$

The coefficient needed for the computation of equilibrium constant are provided as followings:

$$P_{K,1} = \sum_{i=1}^{z_s}(\nu_i'' - \nu_i')\Big(\frac{G_i}{\Re} - \frac{A_i}{\Re}\Big) + \sum_{i=1}^{z_s}(\nu_i'' - \nu_i') \; ln\Big(\frac{101300 P_a}{\Re}\Big), \qquad (3.22)$$

$$P_{K,2} = \sum_{i=1}^{z_s}(\nu_i'' - \nu_i')\frac{A_i}{\Re} - \sum_{i=1}^{z_s}(\nu_i'' - \nu_i'), \qquad (3.23)$$

$$P_{K,3} = -\sum_{i=1}^{z_s}(\nu_i'' - \nu_i')\frac{F_i}{\Re}, \tag{3.24}$$

$$P_{K,4} = \sum_{i=1}^{z_s}(\nu_i'' - \nu_i')\frac{E_i}{2\Re}, \tag{3.25}$$

$$P_{K,5} = 0, \tag{3.26}$$

$$P_{K,6} = \sum_{i=1}^{z_s}(\nu_i'' - \nu_i')\frac{B_i}{2\Re}, \tag{3.27}$$

$$P_{K,7} = \sum_{i=1}^{z_s}(\nu_i'' - \nu_i')\frac{C_i}{6\Re} \tag{3.28}$$

$$P_{K,8} = \sum_{i=1}^{z_s}(\nu_i'' - \nu_i')\frac{D_i}{12\Re}. \tag{3.29}$$

3.2   Transport properties

Gradients of physical properties in the flowfield produce a molecular transport which is directly proportional to the gradient but in the opposite direction. The transport of the momentum of the flow which is proportional to the velocity gradient, as represented by the laminar shear stress, results in the coefficient of viscosity. The transport of thermal energy which is proportional to the temperature gradient results in the thermal conductivity. In diffusion, the transport of molecules in proportion to the concentration gradient of the molecules gives rise to the diffusion coefficient. Thus, the coefficient of viscosity, the thermal conductivity and the diffusion coefficients are known as transport properties. Since the transport of momentum, energy and chemical species is due to collision processes among particles that make up the flowfield, the theoretical prediction of the transport properties requires a knowledge of the potential energy curves which describe the interaction between the various colliding particles.

The macroscopic transport properties can be derived in kinetic theory from the Boltzmann equation. The Chapman-Enskog expansion is used to obtain a solution of the Boltzmann equation. According to Chapman-Enskog theory [52], the transport properties of a dilute gas mixture can be computed to first-order accuracy with the knowledge of just

three binary interaction parameters: the diffusion collision integral $\overline{\Omega}^{(1,1)}$, the viscosity collision integral $\overline{\Omega}^{(2,2)}$ and the dimensionless collision integral ratio $B^* = (5\Omega^{1,2} - 4\Omega^{1,3})/\Omega_{1,1}$. In order to obtain these collision integrals from the interaction potentials of two colliding particles three subsequent integrations have to be performed. Due to the large computational work needed, this cannot be done during the flowfield simulation. Therefore average collision integrals $\overline{\Omega}_{i,j}^{(1,1)}$ and $\overline{\Omega}_{i,j}^{(2,2)}$ are implemented in the code. The underlying collision integrals are defined by

$$
\begin{aligned}
\Omega_{ij}^{(l,s)}(T_i, T_j) = &\frac{8\pi(l+1)}{(s+1)! \left[2l + 1 - (-1)^l\right]} \\
&\cdot \int\limits_0^\infty \int\limits_0^\infty e^{-\gamma^2} \gamma^{2s+3} (1 - \cos^l \chi(b,g)) b\, db\, d\gamma.
\end{aligned}
\tag{3.30}
$$

The variables used in equation 3.30 and the determination of the transport properties based on the Chapman-Enskog method can be found from Markus [27].

Implementation in SINA

Collision integrals for different pairs of species are available from the literature as a function of temperature. The least square method using a 5 degree polynomial fit is employed for the computation of the collision integrals in SINA. The collision integrals for diffusion as a function of temperature in the polynomial form of least square is shown in equation 3.31, for the viscosity in equation 3.32 and for the dimensionless collision ratio in equation 3.33. The values for the diffusion collision integral $\Omega^{1,1}$ and viscosity collision integral $\Omega^{2,2}$ are taken from [30]. Table A.4 and A.6 show the values for the collision integrals for the neutral-neutral interactions over the temperature range 300-20000 K. The dimensionless collision integral ratio B^* is only a weak function of temperature. Therefore, a constant value of $B^* = 1.15$ is used to represent all neutral-neutral interactions [30].

$\Longrightarrow$ **Diffusion collision integral**

$$
\begin{aligned}
\overline{\Omega}_{ij}^{(1,1)} = 10^{-20} \exp \big(&P_{\overline{\Omega},1} (\ln T)^4 + P_{\overline{\Omega},2} (\ln T)^3 \\
&+ P_{\overline{\Omega},3} (\ln T)^2 + P_{\overline{\Omega},4} \ln T + P_{\overline{\Omega},5} \big)
\end{aligned}
\tag{3.31}
$$

$\Longrightarrow$ **Viscosity collision integral**

$$\overline{\Omega}_{ij}^{(2,2)} = 10^{-20} \exp \left(P_{\overline{\Omega},1}(\ln T)^4 + P_{\overline{\Omega},2}(\ln T)^3 \right.$$
$$\left. + P_{\overline{\Omega},3}(\ln T)^2 + P_{\overline{\Omega},4}\ln T + P_{\overline{\Omega},5} \right) \tag{3.32}$$

$\Longrightarrow$ **Dimensionless collision integral ratio**

$$B_{ij}^* = \exp \left(P_{B_{ij}^*,1}(\ln T)^2 + P_{B_{ij}^*,2}\ln T + P_{B_{ij}^*,3} \right) \tag{3.33}$$

3.3 Vibrational energy modes

The translational and rotational modes of the gas are assumed to be in equilibrium with each other at the translational-rotational temperature T. This is based on the assumption that the rate of rotational relaxation is very fast relative to the rate of fluid motion for conditions of interest and also the very few collisions are required for the rotational temperature in order to equilibrate with the translational temperature. Camac [53] showed that all vibrational modes of CO$_2$ relax at the same rate. Therefore, for all the vibrational modes only one vibrational temperature T_{vib,CO_2} is taken.

For vibrational energy computation, Park [44] assumed that the vibrational energy share depends on dissociation energy and reduces with rising translational energy. Therefore, he proposed

$$\hat{E}_{vib,i} = D_{0,i} - \Re T \tag{3.34}$$

for the determination of the energy of dissociation reactions. The relation for the vibration energy for an infinite harmonic oscillator derived on the basis of partition function is

$$E_{vib,in,f,i} = \frac{\Re \theta_{vib,i}}{e^{\frac{\theta_{vib,i}}{T_{vib,i}}} - 1}, \tag{3.35}$$

and heat capacity at constant volume is

$$c_{v,vib,in,f,i} = R_i \left[\frac{\frac{\theta_{vib,i}}{2T_{vib,i}}}{sinh\left(\frac{\theta_{vib,i}}{2T_{vib,i}}\right)} \right]^2. \tag{3.36}$$

For a harmonic oscillator truncated at the dissociation energy, the vibrational energy and heat capacity becomes

$$E_{vib,in,f,i} = \frac{\Re \theta_{vib,i}}{e^{\frac{\theta_{vib,i}}{T_{vib,i}}} - 1} - \frac{D_{0,i}}{e^{\frac{D_{0,i}}{\Re T_{vib,i}}} - 1} \tag{3.37}$$

and

$$c_{v,vib,in,f,i} = R_i \left(\left[\frac{\frac{\theta_{vib,i}}{2T_{vib,i}}}{sinh\left(\frac{\theta_{vib,i}}{2T_{vib,i}}\right)} \right]^2 - \left[\frac{\frac{D_{0,i}}{2\Re T_{vib,i}}}{sinh\left(\frac{D_{0,i}}{2\Re T_{vib,i}}\right)} \right]^2 \right) \tag{3.38}$$

The energy of decomposing and forming molecules is only equal in thermal equilibrium. As a consequence, the vibrational energies of the reacting particles are distinguished as well. From the investigation of state selective reactions Knab et al. [54] [55] obtained

$$E_{vib,va,i,r}(T, T_{vib,i}) = E_{vib,i}(T_{vib,i}) - \Re \frac{\partial \ln k_{f/b}(T, T_{vib,i})}{\partial \left(\frac{1}{T_{vib,i}}\right)} \tag{3.39}$$

if the energy level populations follow a Boltzmann distribution. Therefore, one obtains

$$E_{vib,va,i,r}(T, T_{vib,i}) = (1 - r_r) \left[s_r \Re T_{vib,i} + A_{0,r} \left(\frac{T_{vib,i}}{T} \right)^{r_r} \right] + \frac{\Re \theta_{vib,i}}{e^{\frac{\theta_{vib,i}}{T_{vib,i}}} - 1} - \frac{D_{0,i}}{e^{\frac{D_{0,i}}{\Re T_{vib,i}}} - 1} \tag{3.40}$$

from equations 3.4 and 3.37. The vibrational energy of particles formed within a reaction is determined via

$$E_{vib,app,i,r}(T, T_{vib,i}) = (1 - r_r) \left[s_r \Re T + A_{0,r} \right] + \frac{\Re \theta_{vib,i}}{e^{\frac{\theta_{vib,i}}{T}} - 1} - \frac{D_{0,i}}{e^{\frac{D_{0,i}}{\Re T}} - 1} \tag{3.41}$$

The equation 3.37 is used for all diatomic molecules. However CO_2 is a linear three atomic molecule as shown in figure 3.1 and has three vibrational modes, one of which is doubly degenerated. With the assumption that there is a unique vibrational temperature for each vibrational mode, the vibrational energy of CO_2 is expressed by

$$E_{vib,CO_2}(T_{vib,CO_2}) = E_{vib,CO_2,1}(T_{vib,CO_2}) + E_{vib,CO_2,2}(T_{vib,CO_2}) + E_{vib,CO_2,3}(T_{vib,CO_2}). \tag{3.42}$$

Two-atomic molecules have only one mode of vibration i.e *stretching / symmetric*. The vibrational energy equation presented in equation 3.37 is used to compute vibration energies of diatomic molecules. This equation has to be modified to be used for the computation of vibrational energies of molecules with more than two atoms. The triatomic molecules have two stretching *(symmetric and asymmetric)* and one *bending* mode of vibration. When we consider polyatomic molecules with more than three atoms, it is no

longer obvious how many modes of vibration they have. In fact, a linear molecule has $3N - 5$ normal modes of vibration and a non-linear molecule has $3N - 6$, where N is the number of atoms in the molecule [56]. For developing the Martian atmospheric model, CO_2 is the only molecule with three atoms and previously in SINA, there was no provision to take into account vibrational energies for the three atomic molecule. Therefore, a vibrational model for the three atomic molecule is developed and implemented in the code and is discussed in detail here. It has three modes of vibration, one of which is doubly degenerate as discussed previously. These modes of vibration for CO_2 are shown in figure 3.1.
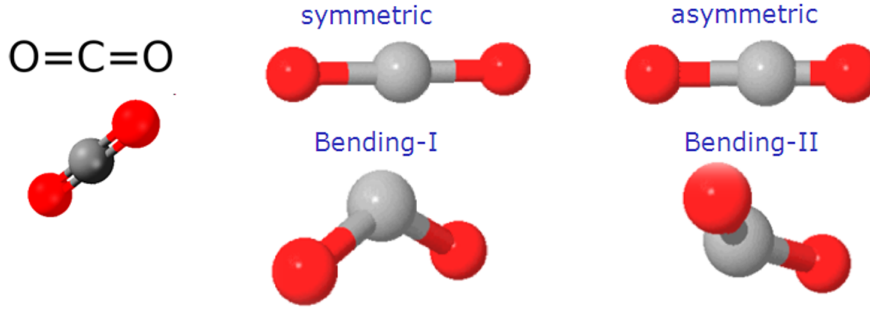
Figure 3.1: Vibrational modes of CO_2

Therefore equation 3.37 is modified in order to take into account three modes of vibration. The modified form is shown with equation 3.43. It is worthy to mention here that equation 3.43 is valid for linear three-atomic molecules i.e. CO_2 only. Small modifications have to be made for the molecules having more than three atoms.

$$E_{vib,CO_2,r} = g_r \frac{\Re\theta_{vib,CO_2,r}}{e^{\frac{\theta_{vib,CO_2,r}}{T_{vib,r}}} - 1} - \frac{D_{0,CO_2}}{e^{\frac{D_{0,CO_2}}{\Re T_{vib,CO_2}}} - 1}. \tag{3.43}$$

here, $\theta_{vib,CO_2,r}$ is the characteristic temperature of vibration of mode r of CO_2 and g_r is the degeneracy of that mode. The constants for $\theta_{vib,CO_2,r}$ and g_r are presented in table 3.2 from [57].

The rate at which these vibrational energies relax toward the translational energy is assumed to behave according to the Landau-Teller relaxation expression presented in equation 2.16. The relaxation time of species due to collisions with species r is determined from an expression due to Millikan and White is given in equation 2.17 and presented in detail in appendix 2.2.2. For the Millikan and White expression for carbon dioxide, the characteristic temperature of vibration of each mode should be used. Thus the three

Table 3.2: Vibrational energy constants

Species	$\theta_{vib}(K)$	g
	1313.67	1
CO_2	663.09	2
	2335.42	1
CO	2169.29	1
O_2	1580.19	1

modes of CO_2 will relax at different rates. However, the results of Camac [53] indicate that the three modes of carbon dioxide relax at the same rate with a characteristic time (in seconds) given by

$$ln\,\tau_{CO_2}\,p = 36.5T^{-1/3} - 17.71, \tag{3.44}$$

where p is the pressure in atmospheres. This expression yields a very different relaxation time than does equation 2.17. The data of Camac yield a relaxation time similar to that of the $\theta_{vib} = 945$ K mode. This indicates that vibrational energy is transferred to this mode from translational, then vibration-vibration coupling transfers energy to the other two modes. The result is that the CO_2 molecule relaxes considerably faster than predicted by the Millikan and White formula. The Camac relaxation time is used for the computation of the vibrational energy of the CO_2 molecules.

3. CO_2 **SOLVER IMPLEMENTATION**

Chapter 4

Particle Solver

A phase is a thermodynamic definition for the state of matter, which can be solid, liquid or gas. It is classified as continuous if it occupies continuously connected regions of space and is classified as disperse when it occupies disconnected regions of space. In a multi-phase flow several phases flow together. The continuous phase may be gaseous or liquid. The disperse phase is formed by particles. The numerical methods used in solving the dispersed multi-phase flow can basically be divided into Eulerian approach and the Lagrangian approach. The Eulerian approach is a way of looking at fluid motion that focuses on specific locations in the space through which the fluid flows. This can be visualized by sitting on the bank of a river and watching the water pass the fixed location. Either Navier-Stokes or Euler equations can be used to model the fluid motion. The Lagrangian approach is a way of looking at fluid motion where the observer follows individual fluid particles as they move through space and time. This can be visualized by sitting in a boat and drifting down a river.

4.1   Euler-Lagrangian method

The combined Euler-Lagrangian is the most suitable method for disperse flows. The Euler-Lagrangian approach has been chosen because it involves a minimum number of empirical equations only, and is more suitable for providing detailed information of the discrete phases. Here, the continuous phase is treated in an Eulerian manner, while the disperse phase is treated in a Lagrangian manner. In the Euler approach the flow variables are a function of space and time and thus are represented as flow fields. In the Lagrangian instead individual particles are considered and the parameters of the

each particle (i.e. position, velocity, temperature) are functions of time. In the Euler-Lagrangian approach, therefore, mass, momentum and energy conservation equation are solved for the continuous phase and for the disperse phase the position and velocity of each particle is obtained from Newton's second law. This requires the interpolation of the continuous phase velocity from the Eulerian grid to the local particle position.
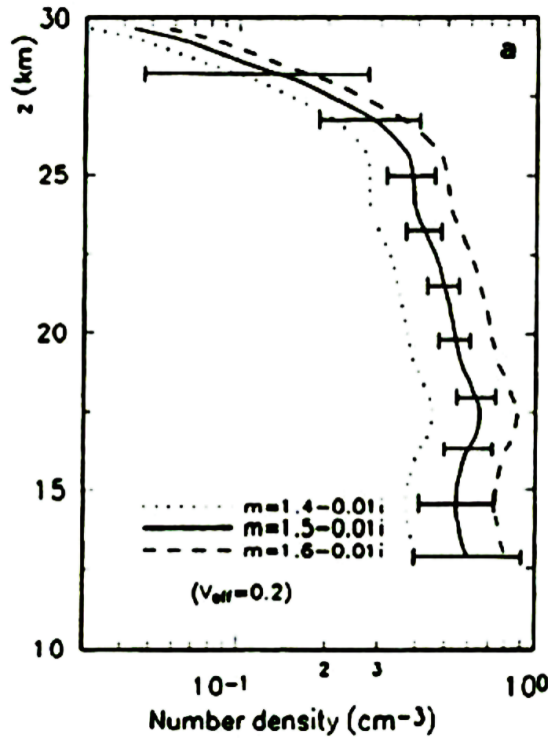
Figure 4.1: Mass mixing ratio of particles [58]

The Euler-Lagrangian approach can be classified [59] with respect to the kind of coupling between the phases. The simplest approach is the the so called one-way coupling. Here, the particle mass loading* respectively volume loading is assumed to be small enough that any effects of the dispersed phase on the continuous phase can be neglected. Thus the local velocity of the continuous phase has a direct impact on the particle motion while the reverse is neglected. If the effects of the particles on the flowfield gas can not be ignored, two-way coupling is required. So called four-way coupling additionally takes into account the particle-particle collision effects due to higher void fraction of the disperse phase and due to the turbulence modification by particles. A rough estimative approach

---

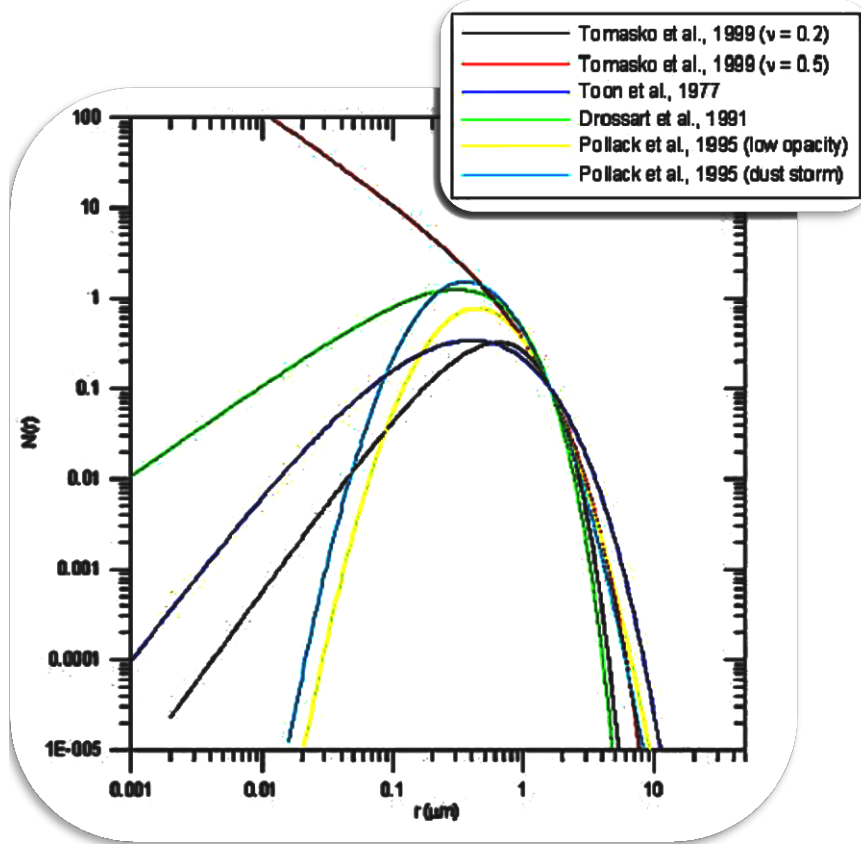*Loading represents the ratio of particle mass/volume to the gas mass/volume

Figure 4.2: Dust particle sizes in Martian atmosphere [58]

to decide about the appropriate coupling can be obtained from the volume fraction of the disperse phase. For very low values, $\alpha_p < 10^{-6}$, one-way coupling can be used while two way coupling may be a reasonable approach up to $\alpha_p \approx 10^{-3}$. For higher values, four-way coupling should be used [59].

The number density of dust particles at different altitudes in Martian atmosphere is shown in figure 4.1. In the constant haze has been quoted as $\approx 1-2\text{cm}^{-3}$ near the surface and between 1 and 0.2 cm^{-3} at altitudes of 15 - 25 km. Above ≈ 25 km, number density declines sharply. The dust mass density is $1.8.10^{-7}\text{kg/m}^{-3}$ in standard conditions and up to $7.10^{-5}\text{kg/m}^{-3}$ during a dust devil. Keeping in view Mar atmospheric density [58], the mass fraction α_p of dust particles is found to be around 1.10^{-4}. Therefore, two-way coupling is taken into account. However one-way coupling is also discussed because it has the significant advantage that the Eulerian velocity field can be computed independently of the particle tracking by a standard single-phase simulation. The continuous phase parameters (i.e. velocity, temperature, density etc) are obtained once at the beginning.

The trajectories of the individual particles are then computed independently from one another.

Based on the work of different groups, the plots for the dust particle sizes in Martian atmosphere are shown in figure 4.2. The sizes of particles varies from 0.01μm to 10μm. The mode radius (r_m) is around 0.4μm [58]. The sizes of bigger particles ranges from 4μm to 10μm. To see the impact of differently sizes particles onto the vehicle in Martian atmosphere, particles with different radii are taken into account for simulation.

4.2 Mathematical modeling

The form of the Lagrangian approach known as *trajectory method* is used for the modeling of the particle solver and it is discussed in detail here.

4.3 Basic assumptions

The main assumptions used in the present study are

1. The particle phase is treated as a discrete set of solid particles which are rigid spheres of equal radii r_p.

2. Only radiation cooling of particle i.e. radiative emission is considered but radiative absorption is not considered. The reason is that there is no radiative heat transfer model available in SINA code.

3. No inter-particle collisions are taken into account. Only one-way and two-way coupling effects are taken into account but four-way coupling is ignored. This is due to the fact that the particle loading ratio is of the order of $\approx 10^{-4}$ as explained in detail in section 4.1.

4. The particle motion is assumed to be translational only i.e. rotational motion is not considered. The reason is that rotational motion is prominent or needed to be taken into account when there is a inter-particle collision.

5. The Magnus force[*], added mass force[†], Basset or history force[‡], saffman lift force[§] and the external forces (gravitational, electric, magnetic) are not taken into account.

---

[*]Particle rotation by any means other than rotation e.g. contact with the wall
[†]Inertia added to particle due to movement
[‡]Force due to the lagging boundary layer development with changing relative velocity
[§]Force generated due to rotation of the particles

Due to smaller size of the particle and the particle rotation is not considered, these forces are not significant.

6. The gaseous flowfield parameters are assumed to be constant everywhere in a given volume cell for particle trajectory computation i.e. no interpolation is made from grid node or grid center to the particle position.

7. The wall of the vehicle is assumed to be fully smooth i.e. only reflection of the particle is considered and no dispersion is taken into account.

8. The particles preserve their shapes everywhere in the flowfield i.e. the uniform phase change (evaporation, melting or sublimation) and no disintegration of the particles take place during simulation.

9. The Biot number is assumed to be less than 0.1*. This is due to the fact that particles under consideration are of micro sizes.

4.3.1   Particle movement

The model of action of the flowfield gas on a particle includes the drag force $\vec{f}_d$ and heating of the particle. The translational motion of the particle is governed by Newton's second law

$$m_p \ d\vec{V}_p/dt = \vec{f}_d. \tag{4.1}$$

Here $m_p = (4/3)\pi\rho_p r_p^3$ is the mass of the particle. Drag force, velocity and new particle position [60] are computed by

$$\vec{f}_d = \frac{1}{2}C_d\pi\rho_p r_p^2 |\Delta\vec{V}|(\Delta\vec{V}), \tag{4.2}$$

$$\vec{V}_p^{n+1} = \vec{V}_p^n + (\vec{f}_d/m_p)\Delta t, \tag{4.3}$$

$$\vec{P}^{n+1} = \frac{1}{2}(\vec{V}_p^{n+1} + \vec{V}_p^n)\Delta t, \tag{4.4}$$

respectively. The $\vec{f}_d$ stands for drag force acting on the particle and $\Delta\vec{V}$ is the relative velocity between the particle and the flowfield velocity and C_d represents the drag coefficient.

---

*The Biot number is defined as hd_p/k_p where h is the convective heat transfer coefficient and k_p is the thermal conductivity of the particle. If the Biot number is less than 0.1, one can assume the internal temperature of the particle is uniform.

As discussed before in section 4.1, the sizes of the particles in the Martian atmosphere are in microns. Due to smaller sizes of particles, the values of relative Reynolds numbers may be very low and values for relative Knudsen numbers are expected to be higher. These low Reynolds number values will lead to very high drag coefficients as depicted in the standard drag curve in figure 4.3. Therefore, for the particle simulation, the model for drag coefficient computation should be capable of dealing with very low Reynolds number or very high Knudsen numbers.
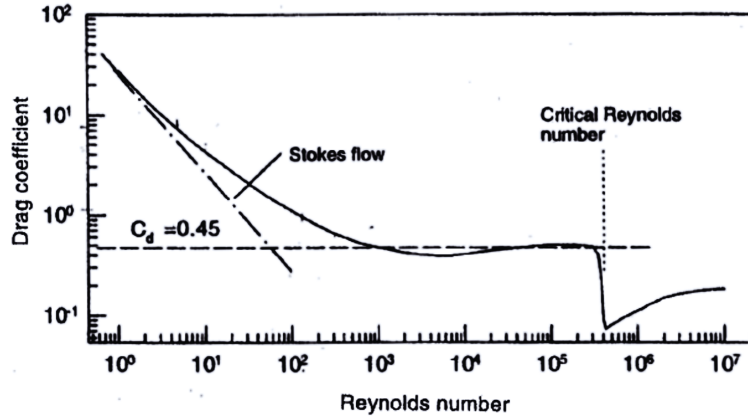
Figure 4.3: Variation of drag coefficient of a sphere with Reynolds number

The drag coefficient C_d is calculated from the approximation formulae proposed by Henderson [61]. Those are suitable for flow regimes ranging from continuum to free molecular flow including slip and transitional flows. The effect of a temperature difference between particle and gas on the drag is also considered. The drag coefficient relations for different flow regimes as described by Henderson are

$$C_d = \begin{cases} C_d^1 & 0 \leq M_{rel} \leq 1, \\ C_d^{12} & 1 < M_{rel} \leq 1.75, \\ C_d^2 & M_{rel} > 1.75, \end{cases} \tag{4.5}$$

where C_d^1 is the drag coefficient for the subsonic region. The equation for this coefficient has the form:

$$C_d^1(Re_{rel}, M_{rel}, T_p/T_g) = 24\left[Re_{rel} + S\left\{4.33 + \frac{3.65 - 1.53T_p/T_g}{1 + 0.353T_p/T_g}\right.\right.$$

$$\times \exp(-0.247 \times 2r_p\rho a/\mu\sqrt{\gamma/2})\bigg\}\bigg]^{-1} + \exp(-0.5(\mu|\Delta\vec{V}|)^{0.5}/a\sqrt{2r_p\rho})$$

$$\times \left[0.1M_{rel}^2 + 0.2M_{rel}^8 + \frac{4.5 + 0.38(0.03Re_{rel} + 0.48\sqrt{Re_{rel}})}{1 + 0.03Re_{rel} + 0.048\sqrt{Re_{rel}}}\right]$$

$$+ \left[1 - \exp(-\mu/2a\rho r_p)\right]0.6S \tag{4.6}$$

where M_{rel} is the relative Mach number, Re_{rel} stands for relative Reynolds number and S is used for the molecular speed ratio. C_d^2 is used to compute the drag coefficient at greater than Mach 1.75. No modification is necessary in this formula and it is reproduced from Henderson.

$$C_d^2(Re_{rel}, M_{rel}, T_p/T_g)$$
$$= \frac{0.9 + \frac{0.34}{M_{rel}^2} + 1.86\sqrt{\frac{M_{rel}}{Re_{rel}}} + \left[2 + \frac{2}{S^2} + \frac{1.058}{S}\sqrt{\frac{T_p}{T_g}} - \frac{1}{S^4}\right]}{1 + 1.86\sqrt{M_{rel}/Re_{rel}}}. \tag{4.7}$$

In the transonic/supersonic region at Mach numbers between 1 and 1.75 the drag coefficients are linearly interpolated using equation 4.11 and equation 4.7 and we get the following bridging relation for this region

$$C_d^{12}(Re_{rel}, M_{rel}, T_p/T_g) = C_{d_1}^1 + \frac{4}{3}(M_{rel} - 1)(C_{d_{1.75}}^2 - C_{d_1}^1), \tag{4.8}$$

where $C_{d_1}^1$ is the drag force coefficient evaluated at Mach number 1 and $C_{d_{1.75}}^2$ is the drag force coefficient evaluated at Mach number 1.75.

The relative velocity $\Delta\vec{V}$ between gas and particle is used for the computation of Mach and Reynolds numbers because it gives the net influence of the gas on the particle. The relative Mach and Reynolds numbers are computed by $M_{rel} = |\Delta\vec{V}|/a$ and $Re_{rel} = 2|\Delta\vec{V}|r_p\rho/\mu$, respectively, and the molecular speed ratio by $S = M_{rel}\sqrt{\gamma/2}$. Due to particle relaxation, there is a possibility that the velocity difference between flowfield and particle becomes either zero or very low. In this case, equation 4.11 tends to become infinite or unstable because it involves velocity terms in the denominator. In order to solve this problem, some modifications are made in equation 4.11, which is used for calculating the drag coefficient below Mach 1. The following equations are used to modify

this relation. The velocities terms involved in the denominator are replaced with other parameters:

$$C_d^1 = 24/A + B + C, \qquad (4.9)$$

where A, B and C

$$A = Re_{rel} + S\left\{4.33 + \frac{3.65 - 1.53T_p/T_g}{1 + 0.353T_p/T_g} \times exp(-0.247 \times 2r_p\rho a/\mu\sqrt{\gamma/2})\right\} = |\Delta\vec{V}|\tilde{A}, \qquad (4.10)$$

$$B = exp(-0.5(\mu|\Delta\vec{V}|)^{0.5}/a\sqrt{2r_p\rho})$$
$$\times \left[0.1M_{rel}^2 + 0.2M_{rel}^8 + \frac{4.5 + 0.38(0.03Re_{rel} + 0.48\sqrt{Re_{rel}})}{1 + 0.03Re_{rel} + 0.048\sqrt{Re_{rel}}}\right], \qquad (4.11)$$

and $$\qquad C = \left[1 - exp(-\mu/2a\rho r_p)\right]0.6S. \qquad (4.12)$$

From equation 4.9 it is clear that A is in the denominator of the term. If A becomes zero or too small, the solution will tend to become unstable. To remove this instability factor, equation 4.9 is multiplied by $|\Delta\vec{V}|$

$$C_d^1|\Delta\vec{V}| = (24/A)|\Delta\vec{V}| + B|\Delta\vec{V}| + C|\Delta\vec{V}|. \qquad (4.13)$$

After some modification in equation 4.10, one gets

$$\tilde{A} = \frac{2\rho r_p}{\mu} + \frac{\sqrt{\gamma/2}}{a}\left\{4.33 + \frac{3.65 - 1.53T_p/T_g}{1 + 0.353T_p/T_g} \times exp(-0.247 \times \frac{2r_p\rho a}{\mu\sqrt{\gamma/2}}\right\} \qquad (4.14)$$

in which there is no term that involves velocity terms. Therefore, $\tilde{A}$ can't get to zero any more. Using equation 4.14, the equation 4.13 can be rewritten as

$$C_d^1|\Delta\vec{V}| = 24/\tilde{A} + (B + C)|\Delta\vec{V}|, \qquad (4.15)$$

in order to avoid instabilities due to lower velocities. These modified equations are implemented in the solver and used to compute the drag coefficient for any flow regime.

4.3.2 Particle locating algorithm

To use the Eulerian-Lagrangian approach, the Eulerian control volume cell within which the particle stays at each Lagrangian time step has to be determined. This information is required for the Lagrangian computation, regardless of whether one-way or two-way coupling is used. This is due to the fact that the computation requires interpolating the flowfield gas transport properties at the current particle position at each Lagrangian time step [62]. In order to determine whether a particle is within a given cell, care is taken about numbering the nodes of the cell in anticlockwise direction when viewing from the front (i.e. front mean in y-direction in case of two dimension grid). Vectors are defined from each particle to each node and also between the nodes as shown in figure 4.4a.

(a) The particle search in the grid   (b) The given cell boundary check for particle location
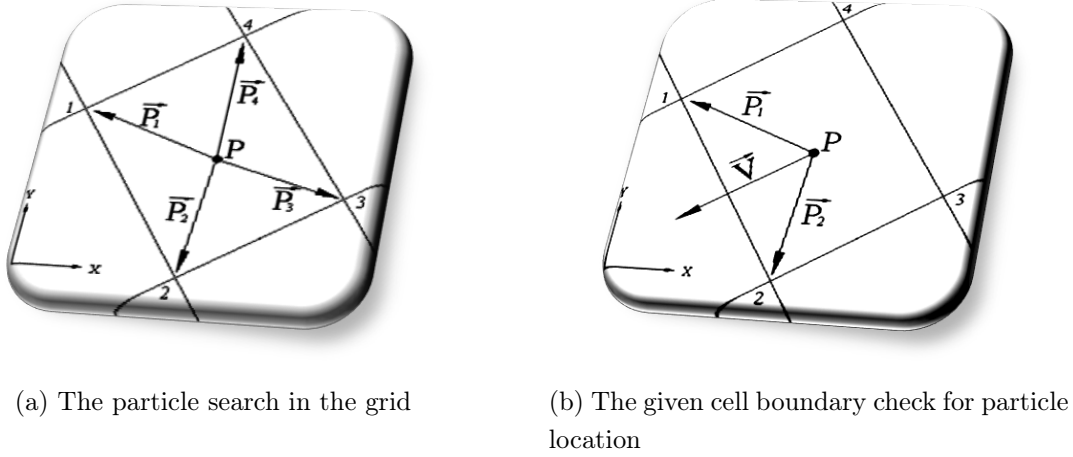
Figure 4.4: Particle locating algorithm description

The particle is inside the cell if it satisfies the following conditions:

$$\begin{aligned}
\vec{P_1} \times \vec{P_2} \geq 0 \\
\vec{P_2} \times \vec{P_3} \geq 0 \\
\vec{P_3} \times \vec{P_4} \geq 0 \\
\vec{P_4} \times \vec{P_1} \geq 0
\end{aligned} \tag{4.16}$$

This technique could be used at each time step but the algorithm will go through all cells until the particle is found, that is not efficient. Once the particle is located, we can check only the cells adjacent to the side the particle has crossed as depicted in Figure 4.4b. The particle has crossed the side of the cell that fulfills the following criteria:

$$\vec{P_1} \times \vec{V} \geq 0$$
$$\vec{P_2} \times \vec{V} < 0 \qquad\qquad (4.17)$$
$$\vec{P_1} \times \vec{P_2} > 0$$

The same procedure is repeated for all sides of the cell until the side that the particle has crossed is found. Then equation 4.16 is used again to locate the particles in the adjacent cells of that side. In this way, we focus only at the neighboring cells of the particle previous position and we don't need to check the entire grid. This method is also used during the modeling of particle-wall interaction to locate the solid wall and the cell side at which the particle has hit the wall. The method presented here works efficiently with the current applications in the code. However there are many other techniques available for the same purpose, presented in [63] [64] [65].

4.3.3 Particle size distribution in the flowfield

Particle sizes can be a important parameter governing the flow of a dispersed two-phase mixture. For spherical particles a measure of the size is the diameter. For non spherical particles an equivalent diameter must be selected to quantify the size. The most general definition of the spread of the particle size distribution is monodisperse or polydisperse. A monodisperse distribution is one in which the particles are close to a single size whereas polydisperse suggests a wide range of particle sizes. For the particle size distribution, one has to choose size intervals, ΔD, which should be large enough to contain many particles yet small enough to obtain sufficient detail. The representative size for the interval is the diameter corresponding to the midpoint of the interval. The number of the particles in each size interval are counted, recorded, and divided by the total number of the particles to be injected. The result are plotted in the form of a histogram (bar chart) as shown in figure 4.5.

This is identified as the discrete number frequency distribution for the particle size*. The approach used to describe size distribution of particles is based on the particle mass (or volume) [66]. With this approach, the mass-average particle diameter is calculated by

$$\overline{D}_n = \sum_{i=1}^{N} D_{p,i} \tilde{f}_m(D_{p,i}), \qquad\qquad (4.18)$$

---

*This frequency distribution is often referred to as the probability density function or "pdf"
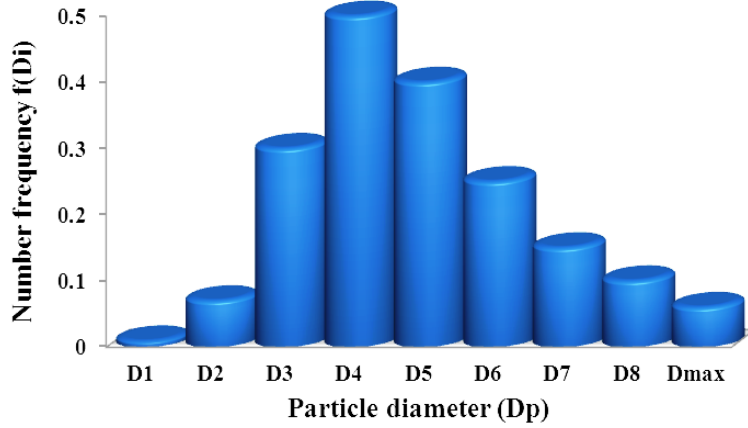
Figure 4.5: Discrete number frequency distribution

where $\tilde{f}_m(D_{p,i})$ represents the discrete mass frequency distribution. This method is intended to be implemented in the code for the particle size distribution. However, a mean/average diameter is used for the current simulations of the particles.

4.3.4 Particle injection

Different schemes are implemented in the code for the injection of the particles in the flowfield. To determine the physical behavior and trajectory analysis of particles, a single or a desired number of particles can be injected into the flowfield. All the injected particles can have different physical input parameters like mass, material, size, temperature or velocities. The models implemented for the injection of the particles in flowfield of the following types:

- **Limited injection of particles**: In order to analyze the particles' trajectories and influence of gas onto the particles, limited number of particles are injected in flowfield. This model is used for the verification and validation of different parameters like temperatures, heat fluxes etc. of the particles.

- **Continuous injection of particles**: The particles have to be injection continuously at the inflow boundary in order to simulate atmospheric entry flows. This model is used for determination of heat fluxes at the wall of the vehicle due to particle impingement.

- **Pointed continuous injection of particles**: This model is implemented in order to extend the capabilities of the particle solver. This model can be used to simulate solid particles in rocket nozzles or in plasma flows.

A rough estimation is made for the allocation of total number of particles in the computational domain [67]. These are found by integrating the gas density in the simulation volume and multiplying the result by the ratio of particle density to the atmospheric density using the equation

$$N = (M_{ratio} / \sum F_m m_p) \int \rho dV. \tag{4.19}$$

The number of particles to be injected at each time step at the inflow boundary are computed for each inflow boundary cell by

$$N_{cell} = (\rho A_{in,\perp} \vec{V}) \times (M_{ratio}/m_p) \times \Delta t, \tag{4.20}$$

where N_{cell} is the number of particles to be injected, M_{ratio} is the loading ratio of the particles. From the expression $\rho A_{in,\perp} \vec{V}$, the mass flux of gas for each cell at inflow is computed. At each time step based on the gas mass flux, the number of the particles are injected.

4.3.5 Heat balance of the particle

For the heat flux computation, convective heating and radiation cooling of the particle are taken into account. Radiation from the gas to the particle is not considered. The convective heat transfer Q_c and the temperature rate dT_p/dt of the particle are computed according to [66; 68; 69]

$$Q_c = N_u \pi d_p k (T_g - T_p) \qquad \text{and} \tag{4.21}$$

$$dT_p/dt = 6k N_u (T_g - T_p)/d_p^2 \rho_p c_{p_p}, \tag{4.22}$$

respectively. The Nusselt number $N_{u_0} = 2 + 0.6\sqrt{Re_{rel}}\sqrt[3]{P_r}$ is computed based on the Ranz-Marshall correlation [70] for forced convection effects and the Prandtl number required for the Nusselt number computation is computed by $P_r = c_p \mu / k$. Because of very high Knudsen number values due to the small sizes of particles and low gas densities during atmospheric entry of the vehicle, rarefaction effects have to be introduced for the Nusselt number calculation. The relation $N_u = N_{u_0}/(1 + 3.42 M_{rel}(Re_{rel} P_r))$ is valid over all flow regimes and yields the correct limit for free molecular flow [66].

The radiative cooling and rate of temperature decrease of the particle are determined from [66]

$$Q_r = -d_p^2 \pi \epsilon \sigma T_p^4 \qquad \text{and} \qquad (4.23)$$

$$dT_p/dt = -6\epsilon \sigma T_p^4 / d_p \rho_p c_{p_p}. \qquad (4.24)$$

The value of total emissivity is exemplary assumed to be at constant 0.8. The negative sign appears in the equations because radiation emitted from the particle is considered. To compute the heat fluxes or the particle temperature rates, the difference of convective heating Q_c and radiation cooling Q_r is taken.

4.3.5.1   Particle heating due to local shock

The convective heating of the particles is computed using equation 4.21. In this equation the Nusselt number is a dimensionless parameter that characterizes the intensity of convective heat exchange between the surface of a body and a flow of gas. This Nusselt number is based on the work of Ranz-Marshall [70] as explained before. Their work was based on the heating of the particle in a regime of subsonic flow. However in hypersonic flow, some other issues have to be addressed as well.

During high speed atmospheric entry, a strong bow shock exists in front of the vehicle. The gas velocity decreases sharply downstream the shock, however, due to inertia, solid particles try to maintain their own velocity. Depending on the size of the particles, the smaller particles may relax quickly downstream the shock. The larger particles maintain their velocity. Therefore, there may be a significant difference between the particle and gas velocity. The relative velocity between the particle and the flowfield may vary from subsonic to hypersonic. Due to this hypersonic effect, a local shock will be develop in front of the particle [67]. The temperature of the gas downstream the local shock will increase and the particle experiences higher gas temperature. To incorporate this temperature rise due to a bow shock in front of the particle surface, a simple normal stagnation point shock relation is introduced:

$$T_{shock} = T_g \big(1 + 0.5(\gamma - 1)M_{rel}^2 \big), \qquad (4.25)$$

where γ represents specific heat ratio and its local value in flowfield is used. It varies from 1.1 to 1.5 depending on flowfield parameters at different points.

However, this is a simple approximation. Therefore it is compared in chapter 5 with the DSMC code in order to verify it. In future development of the solver, this may revised and improved by using appropriate methods to take into account boundary layer effects.

4.3.5.2 Phase change of the particle

We are dealing with particle injection in hypersonic entry flows. There is a possibility for the particle to get heated more than its evaporation temperature. This overheating will result in a phase change and reduction in the mass of the particle [66]. The final form of the particle energy equation is

$$m_p c_{p_p} dT_p/dt = \dot{Q}_{net} + \dot{m} h_L, \tag{4.26}$$

where $\dot{Q}_{net}$ is the total heating that the particle experiences in the flowfield and h_L is the latent heat of vaporization. It is the difference of convective heating and radiative cooling of the particle. During a change in phase, the particle temperature remains constant at the saturation/melting temperature. The heat transfer is just sufficient to balance the energy required for the change of the phase. The rate of change of the particle mass [71] is computed by

$$\dot{m} = \dot{Q}_{net}/h_L. \tag{4.27}$$

The mass loss of the particle provides the information about its size before hitting the wall of the vehicle. The heat flux experienced by the wall due to particle impingement is mainly the particle momentum heat flux. The accurate prediction of the particle size and mass at the wall lead to calculate the right value of heat flux. Also in some cases where the size of the particle is very small and gas temperature is much higher than the evaporation temperature, the particles may evaporate completely before reaching the wall. In the code, such particles are excluded from the computational domain.

Note that chemical reactions between the particles and the gas constituents are not taken into account. This means that in the two-way coupling, the generated gaseous mass has the actual composition of the gas in the corresponding grid cell. Also the surface of the particle is assumed to be fully catalytic.

4.4 Time stepping

In the particle solver different models are used for the computation of the particle movement and heat flux or particle temperature computation. In order to minimize the computational work, the time steps used for the advancement of the particles should be as large as possible. Different constraints have to be put on the movement of the particles in order to guaranty the stability of the Lagrangian solver. The following constraints are used to prevent solver instability problems:

1. To prevent the velocity of the particle to become negative, we limit the time step to

$$\Delta t_1 \leq |\Delta \vec{V}|/a_c, \tag{4.28}$$

   here $\Delta \vec{V}$ is the difference between the gas and particle velocities and a_c is the acceleration of the particles.

2. To ensure that the particle does not cross more than one cell in one time step, a constraint is used on the time step such that the particle movement step is not allowed to be bigger than minimum length of the cell

$$\Delta t_2 \leq -\frac{V_k}{a_{c,k}} + \left[\frac{V_k^2}{a_{c,k}^2} + \frac{2L_m}{a_{c,k}} \right]^{1/2}, \tag{4.29}$$

   here L_m is the minimum length of the cell and k represents x and z axis direction.

3. A third constraint

$$\Delta t_3 \leq |T_g - T_p|/\dot{T}_{rate} \tag{4.30}$$

   is used to prevent the particle temperature from becoming negative during the movement of the particle. The $\dot{T}_{rate}$ is the net rate of temperature decrease taking into account convective heating and radiative cooling of the particle.

The minimum value of the time steps obtained from equations 4.28, 4.29 and 4.30 is used for the advancement of the particles.

$$\Delta t = min(\Delta t_1, \Delta t_2, \Delta t_3) \tag{4.31}$$

4.5 Particle wall interaction

The boundary conditions for particles depend on the boundary type. If a particle crosses the outflow boundary, it is excluded from further considerations. If a particle collides with a solid wall boundary, there are several possibilities depending upon the material and physical conditions of the particle and the wall. The particle could either rebound (specularly or diffusively), penetrate into or stick to the wall. In addition, the particle could also disintegrate, after hitting the wall, resulting in fractional rebound while the rest remains on the wall [72].

Description of the implemented model

Tsirkunov et al. [60; 73] provided a semi-empirical particle-wall collision model for calculating the parameters of a particle just after its collision with the wall. This model is based on the laws of mechanics and the experimental data for the restitution coefficients of the normal and tangential velocity components of the particle gravity center as depicted in figure 4.6.
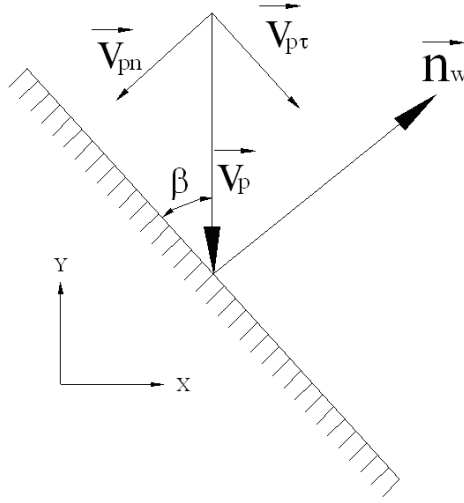

Figure 4.6: Normal and tangential components of particle velocity relative to surface element

The particle impart some part of energy to the wall and rebounds. This is valid at moderate and high particle impact velocities. The equations used for the calculation of the restitution coefficients a_n and a_τ are

$$a_n = 1 - \left[1 - exp\{-0.1(\vec{V}_p^-)^{0.61}\}\right]sin\beta \qquad \text{and}$$

$$a_\tau = C_0 + C_1(\hat{\beta})^2 + C_2(\hat{\beta})^4 + C_3(\hat{\beta})^6. \tag{4.32}$$

The angle $\hat{\beta}$ is computed by $\hat{\beta} = \pi/2 - \beta$ where β is the angle between particle velocity and the wall. The coefficients C_0 to C_3 depend on the wall and particle materials. Tsirkunov et al. [73] proposed a semi empirical model for the tangential restitution coefficients. These are given in table 4.1 for different materials[*]

---

[*]The average standard deviation of the measurements of the coefficients a_n and a_τ was equal to 0.17 and 0.08, respectively

Table 4.1: Coefficient values of different materials of the obstacle

Obstacle Material	Coefficients			
	C_0	C_1	C_2	C_3
Steel	0.690	-0.288	0.114	0.022
Copper	0.588	-0.354	0.076	0.055
Lead	0.430	-0.239	-0.076	0.108

The normal vector to the wall $\vec{n}_w$ is determined using the available mesh information. The normal and tangential velocity components $\vec{V}_{pn}^-$ and $\vec{V}_{p\tau}^-$ are computed according to

$$\vec{V}_{pn}^- = n_x u_p + n_z w_p, \qquad \text{and}$$

$$\vec{V}_{p\tau}^- = n_z u_p - n_x w, \tag{4.33}$$

where n_x and n_z are rectangular components of the wall normal vector $\vec{n}_w$ and particle velocity is expressed by its rectangular components u_p and w_p. The angle between particle velocity and wall is computed from $sin\beta = \vec{V}_{pn}^- / \vec{V}_p^-$ and absolute particle velocity as $\vec{V}_p^- = \left\{ (\vec{V}_{pn}^-)^2 + (\vec{V}_{p\tau}^-)^2 \right\}^{1/2}$. The final relations for the normal and tangential velocities of a particle after its collision take the form

$$\vec{V}_{pn}^+ = -a_n \vec{V}_{pn}^-, \qquad \text{and}$$

$$\vec{V}_{p\tau}^+ = a_\tau \vec{V}_{p\tau}^-, \tag{4.34}$$

where $\vec{V}_{pn}^+$ and $\vec{V}_{p\tau}^+$ are the velocity components of the particle after the collision with the wall. The particle new velocities in x and y direction are determined by

$$\vec{u}_p = \vec{V}_{pn}^+ n_x + \vec{V}_{p\tau}^+ n_z \qquad \text{and}$$

$$\vec{w}_p = \vec{V}_{pn}^+ n_z - \vec{V}_{p\tau}^+ n_x. \tag{4.35}$$

Keeping in mind the current work, usually ceramics or ablators are used as thermal protection materials. In case of ablators, no information about the restitution coefficient is known in literature. However, it is expected that the particles will not rebound, but will stick to the wall. Keller et al. [74] performed a series of experiments to determine the impact of particle impingement on ablative heat shield materials. They found that particles remove some material from the ablator. Based on the experiment data, the following correlation is proposed by Keller et al:

$$\Delta m_a = \Delta m_{ref} + 2.16 \times 10^{-8} u_p^2 D_p^{3.146} \rho_p^{1.86} \Delta M_p, \qquad (4.36)$$

where Δm_a is the ablator sample mass loss and ΔM_p is the ablator mass flow for dust free flow. It is important to mention here that this correlation is valid only under certain conditions because it involves only particle parameters at input conditions. There is no term in the correlation representing the flowfield or atmospheric conditions. The particle behavior varies under different atmospheric and input flow conditions. For example, the particle of small sizes will melt under peak heating conditions. Therefore, this correlation needs to be further investigated and developed in order to incorporate all the requisite parameters. This correlation is not used in the particle solver. It is intended to improve this correlation using the particle solver of SINA. This is left for future work.

4.6   Two-way coupling

As discussed before, taking into account dust particle concentration in the Mars atmosphere, the reverse effect of particles or the disperse phase onto the flowfield is significant. Therefore two-way coupling will be discussed and used for the particle simulation. However, it is important to mention that two-way coupling is very costly, because the particles being simulated are based on the parameters of the flowfield solution. The particles may change or modify the flowfield parameters like velocity, temperature etc. as a result of interaction with it during simulation. To take into account these modifications, the flowfield solvers are again simulated to find a new solution in order to cope with the changes or modifications introduced by the particle solver. The both solvers iterated simultaneously and continuously until a converged solution is achieved. The two-way coupling may take a long time compared with the one-way coupling. If two-way coupling is not necessary, then it is recommended to avoid it. Therefore, during the initialization of the solver, the selection of type of coupling is provided as a choice to the user. The mathematical model being implemented for the determination of two-way coupling effect will now be discussed briefly.

As a particle moves through a computational cell (in the Eulerian gas phase), and possibly evaporates, it contributes to the fluid phase mass, momentum and energy. Thus, the solution of the particle equations provide source terms to the gas phase conservation equations. The time averaging is also performed for the particle source terms in order to get adequate values. In some cases, when the particle loading is high enough, the source

terms from the particle solver are under relaxed. This under relaxation is provided in order to avoid instabilities that may occur in the flowfield solver. The different ways of coupling is discussed briefly here.

Mass coupling is the addition of mass through evaporation. The net evaporation rate between the beginning and end of a time step is given as

$$\Delta \dot{m} = \dot{n} \rho_p \pi \frac{d_{p,start}^3 - d_{p,end}^3}{6}. \tag{4.37}$$

The subscripts named *start* and *end* refer to the beginning and end of an integration time step. The number of particles in a given cell, represented by $\dot{n}$, is calculated from the mass flow rate condition. The source term for the gas-phase continuity equation is given by

$$M_{evp,2way} = \frac{\Delta \dot{m}}{V}, \tag{4.38}$$

where V is the volume of the cell in which the mass addition takes place and $\dot{m}$ is the accumulated mass source term for the cell. This term appears on the right hand side of equation 2.2 in addition to any other mass sources.

Momentum coupling is the result of drag force on the disperse and continuous phases. The momentum source term is evaluated as

$$\vec{F}_{p,cell} = \dot{n}(\vec{f_d} \Delta t), \tag{4.39}$$

where the drag force $\vec{f_d}$ is computed from equation 4.2 and the term $\vec{F}_{p,cell}$ represents the momentum force vector in the x, y and z direction. The source term for the gas-phase momentum conservation equation is given by

$$F_{x,p,2way} = \frac{\vec{F}_{p,cell}}{V}. \tag{4.40}$$

This term appears on the right hand side of equations 2.3, 2.4 and 2.5 in addition to any body force terms such as gravity or magnetic induction etc.

Energy coupling occurs through heat transfer between phases and is given as

$$\dot{q}_{c,cell} = \dot{n} Q_c, \tag{4.41}$$

where Q_c is the convective heat flux from the gas onto the particle and is computed from equation 4.21. The source term for the gas-phase energy equation is given by

$$E_{p,2way} = \frac{\dot{q}_{c,cell}}{V}. \tag{4.42}$$

4. PARTICLE SOLVER

This term appears on the right hand side of the equation 2.6 in the flowfield energy equation term in addition to any other source terms such as radiative source terms or magnetic induction.

Chapter 5

Verification and Validation

Sources of errors and uncertainties in results from simulations can be divided into two distinct sources: modeling errors and numerical errors. Modeling errors and uncertainties are due to assumptions and approximations in the mathematical representation of the physical problem (such as geometry, mathematical equation, coordinate transformation, boundary conditions, thermal models etc.) and incorporation of previous data (such as fluid properties) into the model. Numerical errors and uncertainties are due to numerical solution of the mathematical equations (such as discretization, artificial dissipation, incomplete iterative and grid convergence, lack of conservation of mass, momentum, and energy, internal and external boundary non-continuity, computer round-off, etc.). Therefore, one of the most important task in computational fluid dynamics is to compare and verify the physical models being implemented in the codes. Comparison and verification are the primary means to assess accuracy and reliability in computational simulations by comparison with known solutions and is centered on the accumulation of evidence that a specific calculation is correct and accurate. It implies detail surface and flowfield comparison with experimental or published results from different external resources. The results can be compared to experimental data or to published reference data or a code to code comparison can also be made in this regard. However, in any case computed values of a specific parameter are compared with some external sources. Some code developers prefer to compare the results computed using an established, reference(benchmark) CFD code. Comparisons with parameters computed using an established code play a useful role during the development of a CFD code. Basic purpose of the code verification is the error evaluation which is, looking for bugs, incorrect implementations of conceptual models, errors in inputs, and other errors in the code and usage. Assessment of the accuracy

of code solutions, given the underlying equations, is the basic objective of the validation assessment. Developing confidence that the code solution is accurate for problems other than verification tests is a key goal of this effort. Therefore, an obvious requirement is to perform the required verification activities in a way that maximizes confidence in the accuracy of new calculations. To rigorously verify a code requires rigorous proof that the computational implementation accurately represents the conceptual model and its solution. This, in turn, requires proof that the algorithms implemented in the code correctly approximate the underlying mathematical models, along with the stated initial and boundary conditions. In addition, it must also be proven that the algorithms converge to the correct solutions of these equations in all circumstances under which the code will be applied.

In chapter 3 the development of the CO_2 solver is discussed in detail and in chapter 4 development of the particle solver is presented. During the implementation of these solvers, in order to get higher confidence and to have a code with minimum bugs, the solvers are compared and verified with external established resources.

5.1 Verification of CO_2 solver

As discussed in chapter 3, in the code the Martian atmosphere model with five species carbon dioxide (CO_2), molecular oxygen (O_2), carbon monoxide (CO), oxygen (O) and carbon (C) is implemented. In order to verify that all the models and data are properly and correctly implemented in the code, the verification and validation of the solver is necessary. In hypersonic entry flows high temperature and non equilibrium gas flows are the major issues. The best way to test the chemical solver is to determine the equilibrium composition for different temperature ranges and compare it with a reference.

The NASA CEA (*Chemical Equilibrium with Applications*) [75] program is used as reference for the verification of equilibrium constant of the CO_2 solver. This program calculates chemical equilibrium product concentrations from any set of reactants and determines thermodynamic and transport properties for the product mixture. CEA represents the latest in a number of computer programs that have been developed at NASA Lewis (now Glenn) research center during the last 45 years. These programs have changed over the years to include additional techniques. Associated with the program are independent databases with transport and thermodynamic properties of individual species. Over 2000 species are contained in the thermodynamic database. The program is written in ANSI standard Fortran by Bonnie J. McBride and Sanford Gordon.

Both codes (SINA and CEA) at simulated at different temperature ranges i.e. from 300 K to 8000 K at a constant pressure of 7.87 pascals (this is the entry pressure for MSRO mission in the Martian atmosphere*). The mole fractions of each species corresponding to these temperatures are compared. The results are presented in figure 5.1.
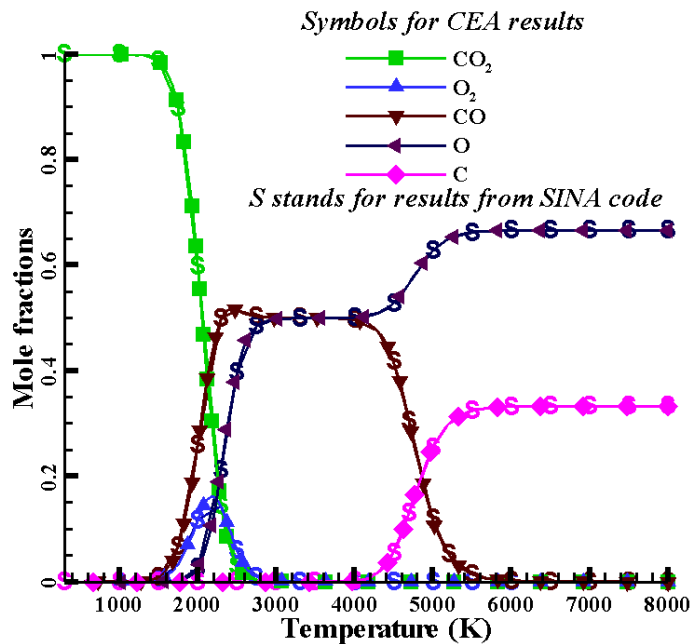

Figure 5.1: Equilibrium composition comparison between 300 K and 8000 K

The results from both of the codes are in a very good agreement with each other. This comparison verifies that the chemical part of the new CO_2 solver (as far as the chemical equilibrium constant is concerned) works properly and the results we get from the code are satisfactory. The present computation is made with 99.9996 % mole fraction of CO_2 and mole fractions for all other remaing species are 0.0001 %. From figure 5.1 it is clear that CO_2 starts dissociating just below 2000 K which results in the production of CO and O_2. The atomic oxygen started prodcuing above 2000 K. Around 3000 K almost all CO_2 is completely disappeared leaving CO and O the only species in the flowfield up to approximately 5000 K. The bevaiour of O_2 is also very interesting becasue it starts appearing just below 2000 K and around 3000 K nearly alongwith CO_2 it disappears. There is no carbon formation in the flowfield till nearly 4500 K. Above this point it starts forming becasue at the same temperature CO starts dissociating. Above 6000 K all the

---

*The same pressure is used for Martian entry simulation in chapter 6

molecules are completely dissociated and only atomic oxygen and carbon are available in the gas.

5.2 Particle solver verification

As discussed before, there are different sources to verify and validate the code such as reference data or experiments. Unfortunately, the author could not get reliable data from experiments that could be used for the verification and validation purposes. In this way there is no option left else to compare the data with an available reference data or to make code to code comparison. For this purpose, the code to code comparison and verification of the data is made with the code TINA (Thermochemical Implicit Non-Equilibrium Algorithm) of Fluid Gravity Engineering Ltd. (FGE). The purpose of comparison is also to discuss about the modeling of the particle solver from various aspects. In order to get a higher level of confidence, it is always helpful to know how others have solved the same problem and what kind of models they have used.

Gas inflow data

- Air is used as gaseous flowfield medium
- The 57 degree sphere with nose radius 1.7m is used
- Inflow velocity: $u_\infty = 6000$ m/s
- Density: $\rho_\infty = \ 3.1.10^{-4}$kg/m^3
- Temperature: $T_\infty = 247$ K

Particle information

- Particle sizes $D_p \in \{0.1, 1, 3, 5, 7, 9, 11, 13, 15, 20\}\mu$m
- Density: $\rho_\mathrm{p} = 2266$ kg/m^3
- Specific heat: $c_{pp} = 1000$ J/kgK
- Heat of fusion: $h_f = 1.88.10^5$ J/kg
- Melt temperature: $T_m = 1938$ K
- Heat of evaporation: $h_{vap} = 8.8.10^6$ J/kg

Based on the input conditions given above, the flowfield simulations are performed. For the discretization of the body, a grid with 51×61 volume cells was employed. The mesh is structured and finer near the wall to properly resolve the boundary layer. The cell size at wall is 5.10^{-7}m. The wall temperature is set to 2000 K. The plots of velocity and temperature are presented in figure 5.2. The inflow velocity contours of the flowfield are presented in figure 5.2a. Due to the hypersonic inflow conditions, a strong bow shock develops, resulting in a very high gas temperature in front of the vehicle as shown in figure 5.2b. Particle solver is used to simulate the influence of the flowfield on particles using the converged solution of the flowfield solvers. One-way coupling is used for the following code to code comparison.
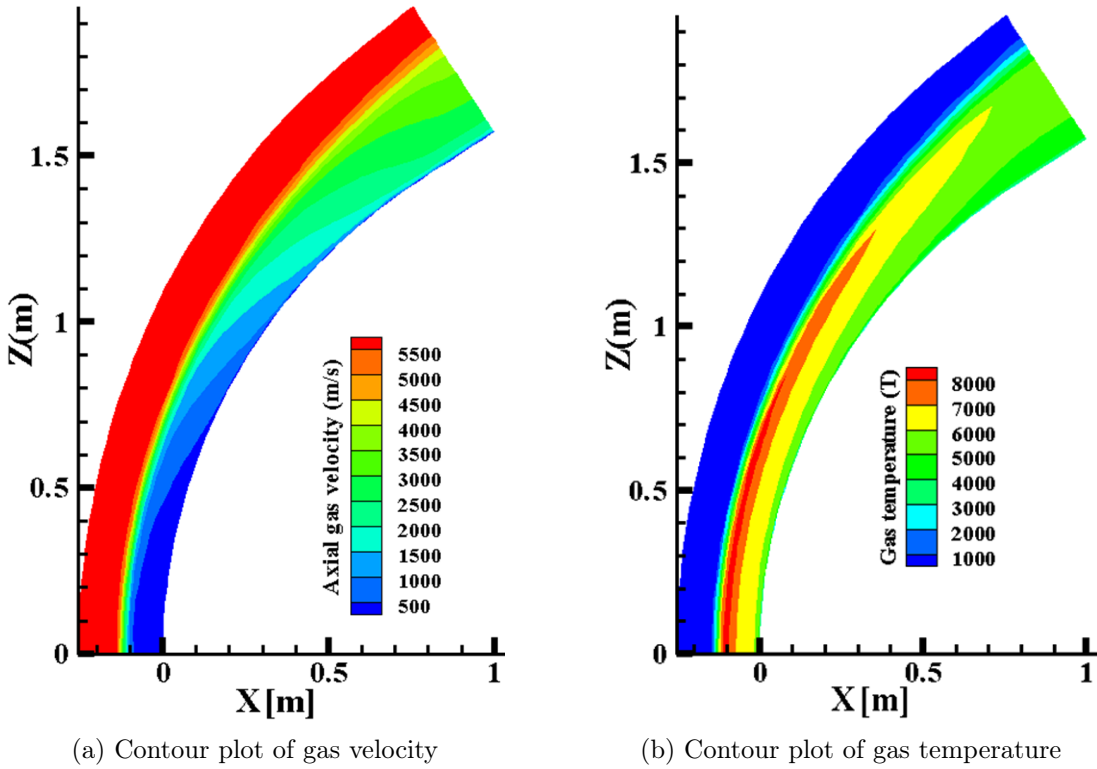

(a) Contour plot of gas velocity   (b) Contour plot of gas temperature

Figure 5.2: Contour plots of gaseous flow field

5.2.1 Particle momentum and temperature comparison

Particles of different sizes are injected at the inflow boundary. Velocity and temperature histories are compared at different locations with different input conditions. Velocity and

temperature history curve for the injected particle of size 3μm near the stagnation line is presented in figure 5.3.

(a) Particle velocity comparison
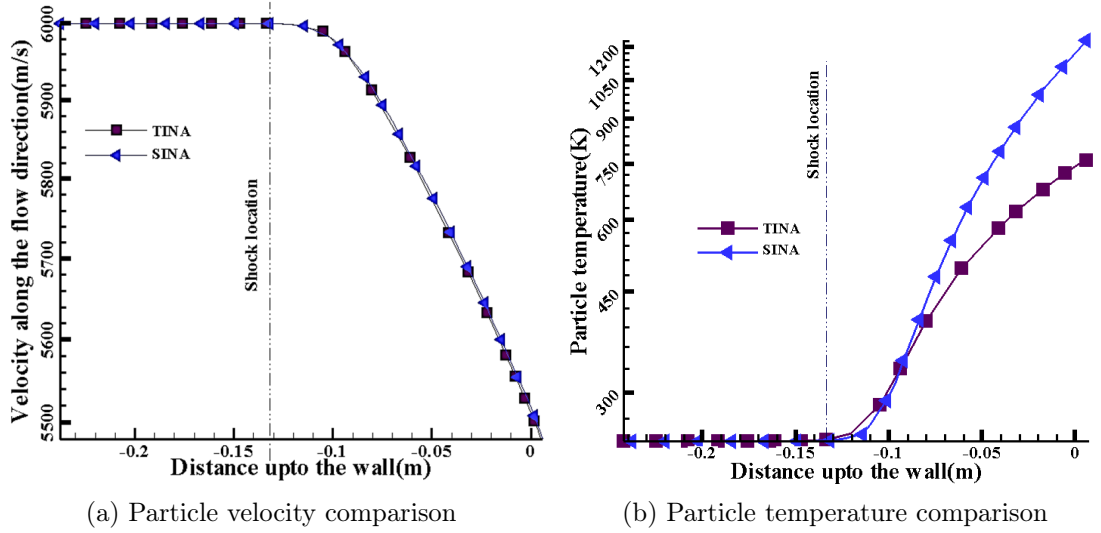
(b) Particle temperature comparison

Figure 5.3: Comparison of particle parameters between TINA and SINA

The velocity comparison is shown in figure 5.3a. Results from both codes (SINA and TINA) are in good agreements with each other. Both codes used the same model for drag coefficient computation. This comparison verifies that these models are implemented correctly. The temperature comparison is shown in figure 5.3b. Unlike the velocity curve the results of temperature don't match. Downstream the shock, the temperature curves start diverging from one another. The values computed by SINA are significanlty higher compared to the results from the TINA code of FGE.

For the convective heat transfer from the gas to the solid particle, the Nusselt number is the key parameter. The correlation used to determine the Nusselt number is $N_{u_0} = 2 + 0.6\sqrt{Re_{rel}}\sqrt[3]{P_r}$ and it is discussed in detail in chapter 4. In this relation the Prandtl number $P_r = c_p\mu/k$ and Reynolds number $Re_{rel} = 2|\Delta\vec{V}|r_p\rho/\mu$ are used that are based on the viscosity μ and thermal conductivity k. These variables are computed based on the model used for the determination of transport coefficients. In SINA these computations are based on the Chapman-Enskog theory. However, the models used in TINA code for the transport coefficients are not known to author. Due to limitation of time, it was not possible to make detail comparison of flowfield modeling of both codes. This is left for the future work. In order to make further verification, the heat transfer model is also compared to other approach DSMC (in section 5.2.2).

5.2.2   High speed flow effects on particle heating

In section 4.3.5.1 of chapter 4 the overheating onto the particle due to supersonic/hypersonic relative velocity is discussed and a simple correlation is also presented to take into account this effect.

Particles of different radii are injected into the flowfield and the trajectories of the particles are tracked. The results are shown in figure 5.4.
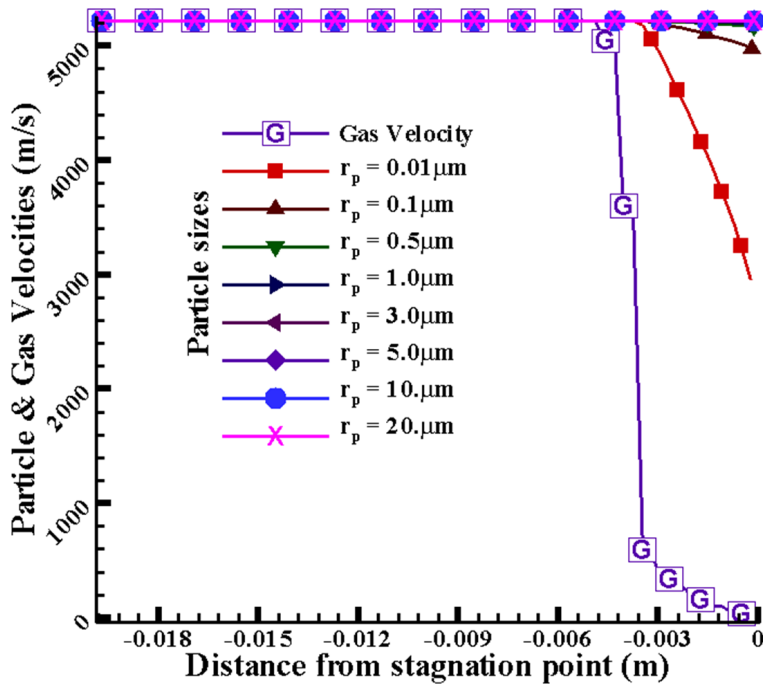

Figure 5.4: Particle and gas velocities in flowfield

The inflow velocities of gas and particles are the same, i.e. 6 km/s. After the shock the gas velocity reduces sharply. The smaller particles of radius 0.5µm relax quickly and follow the gas velocity, so their velocity also reduces to become very small. However, the particles of larger sizes don't relax quickly enough and tend to retain their own velocities because of higher inertia. As a result there is a notable difference between the velocity of the particle and the velocity of the gas. Because of this huge relative difference, the larger particles experience a local shock in front of them and get additional heating.

To the knowledge of the author the additional heating effect onto the particle due to local shock has never been discussed before. There is no reference literature available in order to compare or verify this effect. To verify or evaluate this effect, a Direct Simulation Monte Carlo (DSMC) method is used. It uses probabilistic (Monte Carlo) simulation to

solve the Boltzmann equation for high Knudsen number fluid flows. This approach is based on the technique for the modeling of a real gas by millions of simulated molecules. The velocity components and position of these molecules are stored and are modified with time as the molecules are concurrently followed through representative collisions and boundary interactions. This physical simulation approach is fundamentally different from convectional CFD which seeks to obtain a numerical solution of a continuum model of the gas, generally the Navier-Stokes equations. The computational task associated with the direct physical simulation becomes feasible if the density of the gas is sufficiently low or the physical dimensions of the flowfield is sufficiently small.

The DS2V code of GA Bird is also used for comparison and verification of particle heating in high temperature gas flows. This program is freely available [76] and known to be one of the wide spread codes for DSMC applications. The theoretical models on which this code mainly developed are presented in [77]. The outstanding feature of this code is that it is intended for use by non-specialists and, as far as possible, the computational parameters are generated automatically by the program. This minimizes poor calculations being made as a consequence of a poor data set.

The one of motives to make DSMC computations is to make comparison of the results with both codes (SINA and TINA). However, as discussed before, air was used as a flowfield medium in the TINA code. Therefore, in order to allow comparison between the different codes, air is used as a gaseous phase medium.

Description of input conditions

The DS2V code simulates the flow around objects of various shapes. There is no option available to move particles in the flowfield. Therefore, the flow around the particle is simulated in order to obtain heat fluxes onto the particle due to incoming gas. The same procedure is repeated in the particle solve of the SINA code for comparison purposes. The geometry and inflow conditions are described as followings:

- Solid sphere of diameter 20μm is simulated in general. However few simulations are also made with other particles of radii 10μm, 50μm etc.

- Surface temperature of the particle is fixed to 300 K in both codes in order to avoid the complexities involved with the solid-gas interactions and get a better comparison of heat fluxes.

- Free stream velocities and temperatures are varied in different cases from 1000 m/s to 8000 m/s and 1000 K to 8000 K respectively.

- The inflow density is $6.6245.10^{-3}$ kg/m^3 and the corresponding number density is $1.377300.10^{23}$/m^3 and mean free path is $1.2266.10^{-3}$m [78]. Keeping in view size of the particle (i.e. 20μm), the value of Knudsen number is around 0.6. This relatively higher value of Knudsen number indicates that flow can no more be treated as continuum.

- For DSMC calculations, diffusive reflection with full accommodation to the surface temperature is taken.

- Only two species are taken into account, i.e Nitrogen(N_2) 81% and Oxygen(O_2) 19%.

Based on the above input conditions, simulations are performed for different cases. These conditions represents the flow conditions after the shock and in this region temperatures are usually very high.
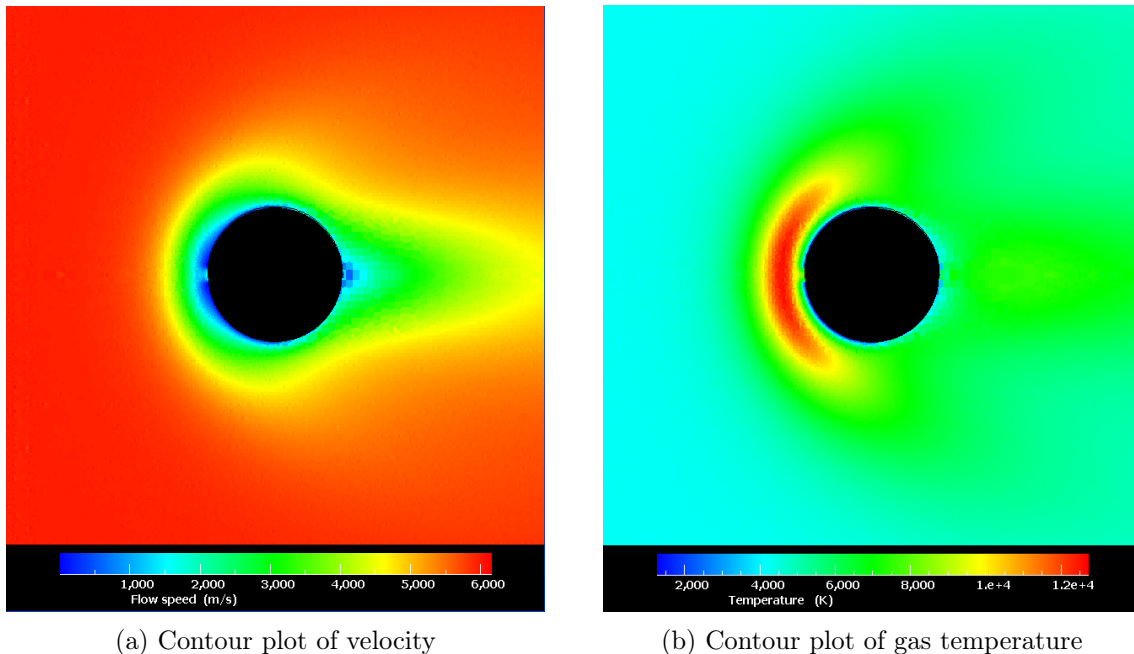

(a) Contour plot of velocity   (b) Contour plot of gas temperature

Figure 5.5: Contour plots of flowfield around a particle by DSMC code DS2V

The contour plots of temperature and velocity for the particle of radius 20μm with inflow velocity of 6000 m/s and temperature of 4000 K are shown in figure 5.5. The

relative velocity of the particles is also very high as previously discussed and shown in figure 5.4. A bow shock forms in front of the particle and gas velocity reduces to the smaller value which is visible in the velocity contour plot 5.5a. The temperature of the flowfield increases and the flow surrounding the particle is at higher temperature than the inflow gas temperature as obvious from the contour plot of temperature in figure 5.5b.

The particles under considerations are very small. In order to get information about the actual heating on these particles, it is important to see the total heating onto the particle. For the heat fluxes onto the particle, various simulations with both codes under different input conditions are presented in table 5.1.

Table 5.1: Comparison of heat flux computation between SINA and DS2V

			Heat flux		
Diameter	Velocity	Temperature	DS2V	SINA (with Shock)	SINA (w/o Shock)
μm	m/s	K	W	W	W
20	1000	4000	0.0202	0.0243	0.0214
	2000	4000	0.0471	0.0362	0.0236
	4000	4000	0.1726	0.0838	0.0267
	6000	4000	0.4536	0.1691	0.0290
	4000	1000	0.1148	0.0354	0.0029
	4000	2000	0.1352	0.0520	0.0092
	4000	4000	0.1726	0.0838	0.0267
	4000	6000	0.2007	0.1170	0.0489
	4000	8000	0.2354	0.1523	0.0750
10	1000	4000	0.0055	0.0072	0.0064
	6000	4000	0.1173	0.0448	0.0081
50	1000	4000	0.1023	0.1294	0.1149
	6000	4000	2.6058	0.9472	0.1710

The comparison is shown among three different approaches. The results from the particle solver of SINA code are shown with and without local shock heating effect. From table 5.1 it is clear that results computed by DSMC are higher as compared to the SINA particle solver results. However, the results computed by SINA in which the local shock effects are taken into account are relatively closer to the DSMC results. One reason for
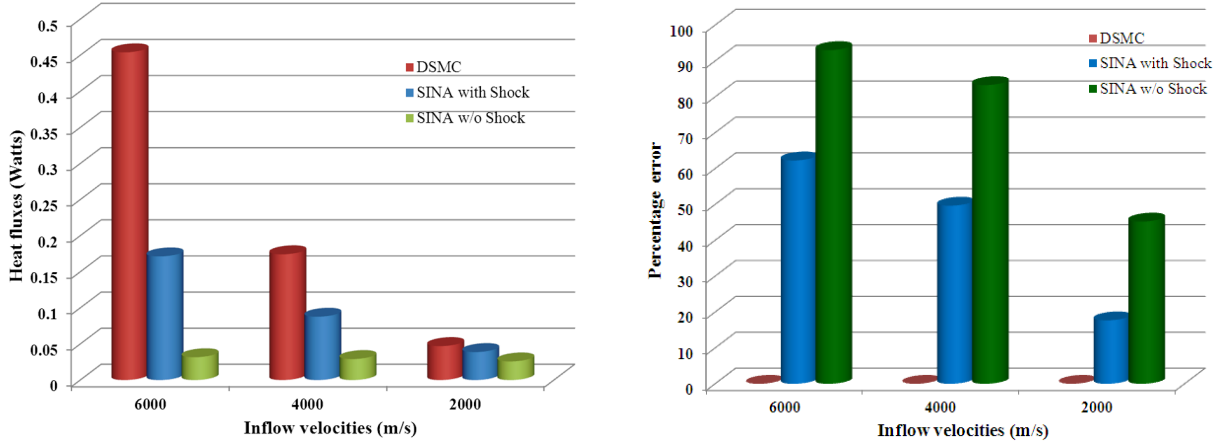
(a) Total heat flux comparison between SINA and DS2V

(b) Percentage error in heat flux values between SINA and DS2V

Figure 5.6: Plots for total heat flux comparison and relative error between results

the difference in results between the both results might be the correlation used in SINA code. This is an empirical correlation and its range of validity is limited.

The plots of selected simulation are also presented in figure 5.6 in order to further elaborate the variation in the values of heat fluxes among different approaches. The heat fluxes onto the particles of radius 20μm with three inflow velocities 2000 m/s, 4000 m/s and 6000 m/s are shown in figure 5.6a. The flowfield gas temperature was set to 4000 K because in some cases this is the value of temperature downstream the shock.

In figure 5.6a the difference of results between the approaches is significant. The results of SINA code including the shock effect are significantly closer to the results of DSMC code. This comparison ascertains the fact that the particle experiences extra heating due to development of local shock in front of the vehicle. In order to get a clear picture of the difference between the different methods, the relative error between the results is shown in figure 5.6b. The results from DS2V are taken as a reference because we are interested only in the relative difference of values. This figure reveals two interesting facts. One of which is that even by including simple stagnation point shock relation, our results are much improved and closer to the DSMC results. The other fact is that as the flow velocity increases, the difference in relative error also increases if the post shock temperature correlation is not used. This is because by increasing the relative velocity, the shock also gets stronger and after the shock the temperature also increases sharply.
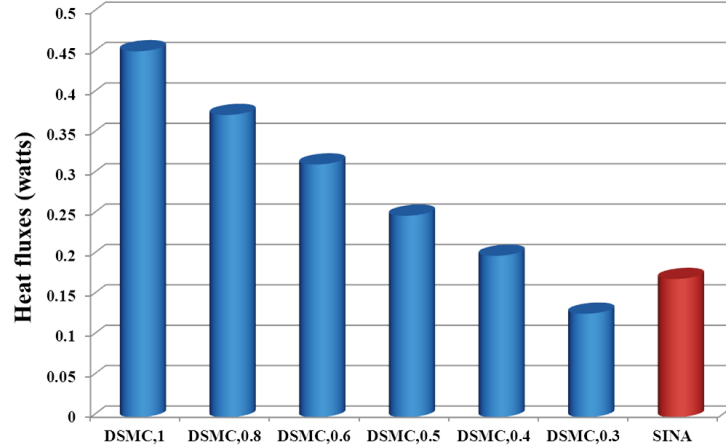
Figure 5.7: Heat fluxes due to variation in energy accommodation at wall

Effect of energy accommodation on heat fluxes

In DSMC calculations, full accommodation of energy to the particle surface is taken into account. For practical applications, the energy accommodation lies between 0 and 1. Due to unavailability of information regarding the energy accommodation values, it is assumed to be 1 for the simulation of DS2V code. However, it is worthy to determine the impact of the partial accommodation of energy on the particle surface. In DS2V code, the Cercignani-Lampis-Lord(CLL) method is available that takes into account partial accommodation of energy. The CLL model incorporates independent accommodation coefficients for normal and tangential velocity components. This method is explained in detail in [79]. Various simulations are made using DS2V code, with different energy accommodation values. These are presented in figure 5.7. For these simulations, same values for normal and tangential accommodation of energies are used. These values are varied starting from 1 (full accommodation of energy) to 0.3. A notable difference in heat flux values is observed. The major reason for the current simulations was to determine the value of accommodation energy at which the results of DS2V code matches with SINA results. From figure 5.7, it is clear that results of SINA lies between energy accommodation values of 0.3 and 0.4.

Chapter 6

Results and Analysis

Based on the models developed and implemented in SINA, the behavior of solid particles in Martian atmosphere during hypersonic entry is studied. For this purpose, a sphere of radius 0.05 m is used for current simulation. For the discretization of the flowfield, a grid with 26×42 volume cells is employed. The mesh is structured and finer near the wall to properly resolve the boundary layer.
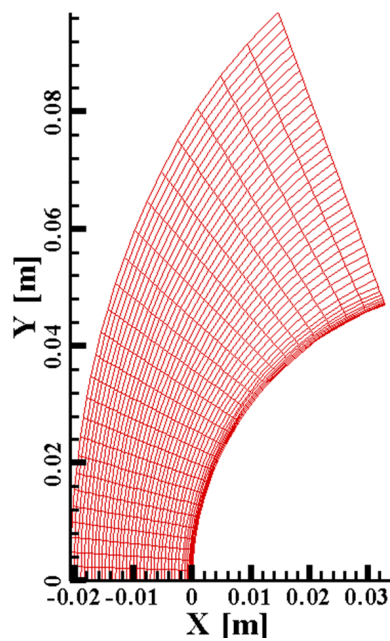

Figure 6.1: Grid for flowfield simulations

6. RESULTS AND ANALYSIS

Gas inflow data

- The simulations are made with thermal equilibrium and chemical non-equilibrium.

- The wall temperature: $T_w = 1500$ K

- Inflow velocity: $u_\infty = 5223$ m/s

- Density: $\rho_\infty = 2.933.10^{-4}$ kg/m^3

- Temperature: $T_\infty = 288$ K

- Pressure: $p_\infty = 7.87$ Pa

- Mole fractions of different species [42]

    1. $\psi_{CO_2} = 0.999998807907$
    2. $\psi_{O_2} = 1.00000000363$d-09
    3. $\psi_{CO} = 1.16885871648$d-06
    4. $\psi_O = 1.00000000363$d-09
    5. $\psi_C = 1.00000000363$d-09

Particle information

- To study the particle behavior in flowfield and to investigate particle trajectories, particle of the sizes $D_p \in \{0.01, 0.1, 0.5, 1, 3, 5, 10, 20\}\,\mu m$ are injected in the flowfield.

- Silicon dioxide S_iO_2 is considered as the particle material because it is the major constituent (43.4% [58]) of Mars soil. The detailed chemical composition of Mars soil is presented in A.8 from Alexander [58].

    * Density: $\rho_p = 2264$ kg/m^3
    * Specific heat: $c_{pp} = 1000$ J/kgK
    * Heat of fusion: $h_f = 1.88.10^5$ J/kg
    * Melt temperature: $T_m = 1938$ K
    * Heat of evaporation: $h_{vap} = 8.8.10^6$ J/kg

The flowfield velocity of the converged solution is shown in 6.2a. A strong bow shock develops due to the high entry velocity. The higher temperature values of the gaseous flow field shown in 6.2b result from the bow shock and the high entry velocity. The pressure also increases downstream the shock as presented in figure 6.3a. It is also interesting to

see the distribution of mole fractions of different species in flowfield. In figure 6.3b the mole fraction of CO_2 are presented. Downstream the shock, due to high temperature, the mole fractions of CO_2 starts decreasing and reaches to smaller values.

(a) Contour plot of velocity

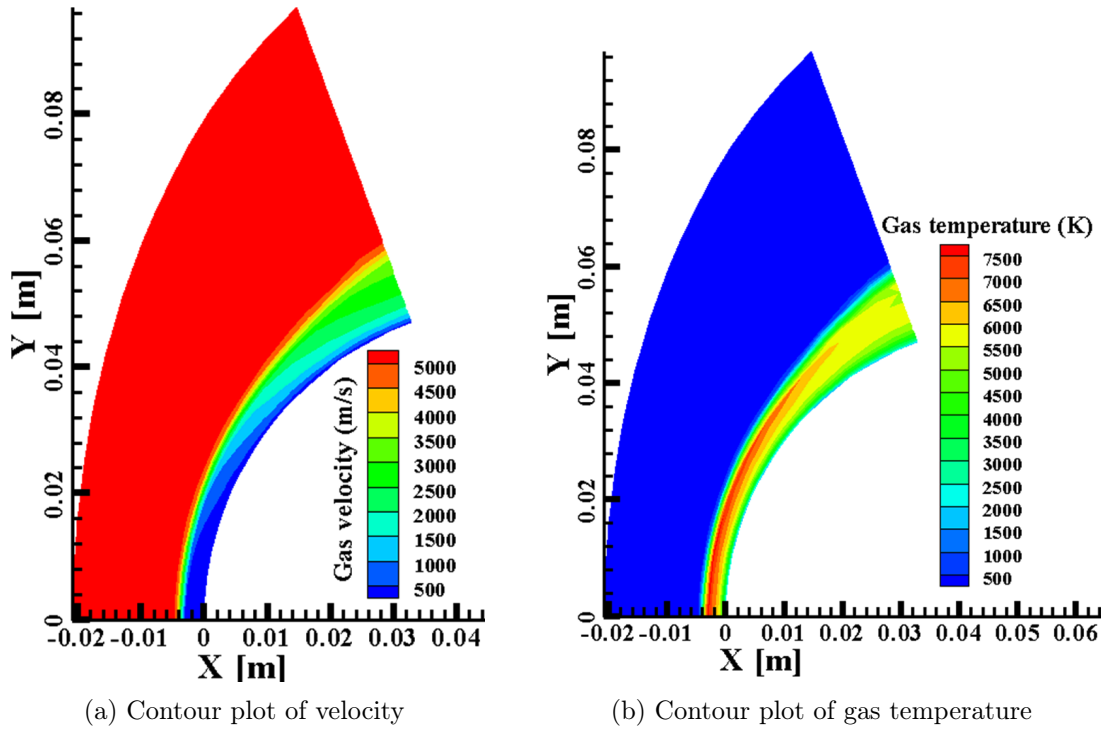(b) Contour plot of gas temperature

Figure 6.2: Contour plots of gas velocity and temperature in flowfield

The distribution of different parameters along the stagnation line is presented in figure 6.4. This is important in order to see and investigate the behavior of flowfield parameters. The distribution of temperature, pressure and velocity is shown in figure 6.4a. Upstream the shock, there is no change in the parameter as expected. Downstream the shock, temperature rises to around 8000 K, pressure increases to slightly 8000 Pa and velocity decreases sharply. Due to increase in temperature, the mole fraction of different species also changes. The mole fraction distribution along stagnation line is shown in figure 6.4b. Downstream the shock, dissociation of CO_2 starts resulting in production of other species. Due to decrease in gas temperature while reaching at object wall, slight changes in mole fractions of different species is observed.

(a) Contour plot of pressure

(b) Contour plot of mole fractions of CO_2
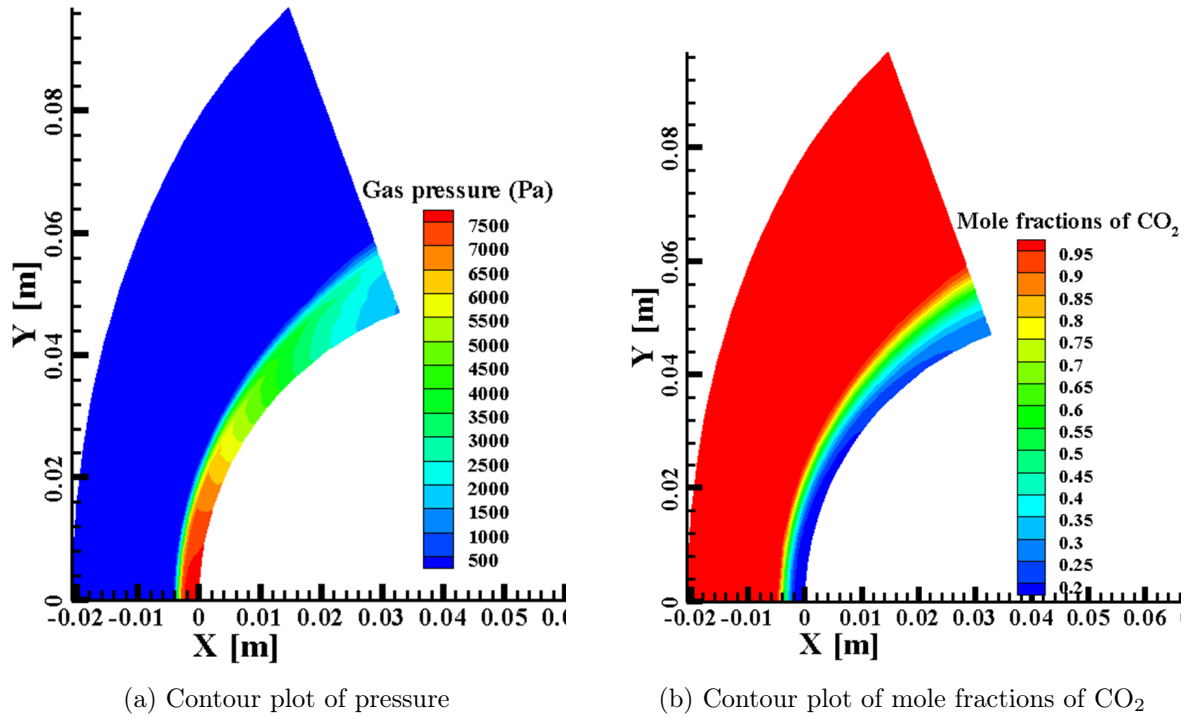
Figure 6.3: Contour plots of pressure and mole fractions of CO_2 in flowfield

(a) Gas temperature, pressure and velocity distribution
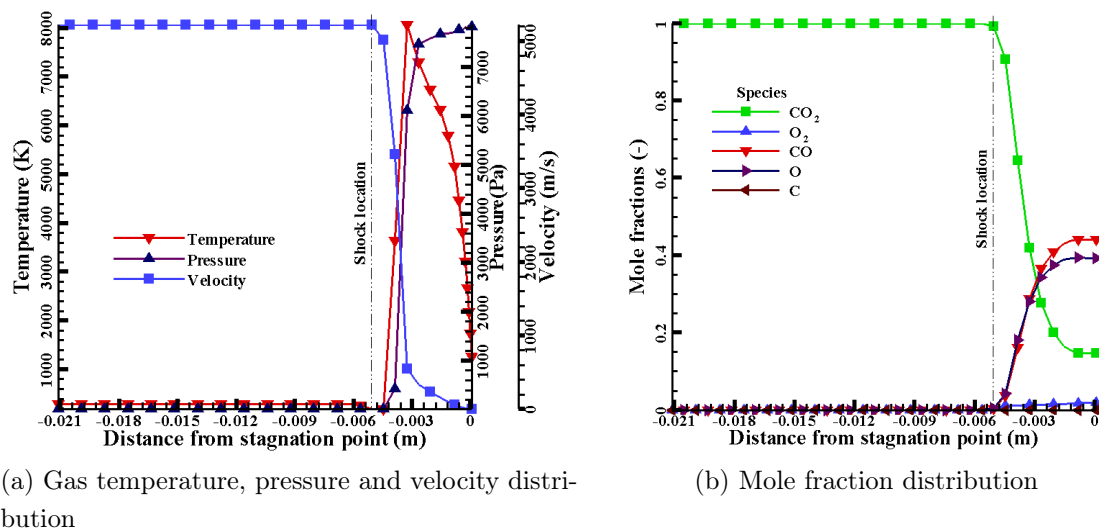
(b) Mole fraction distribution

Figure 6.4: Distribution of mole fraction and flowfield parameters along stagnation line

6.1 Parametric analysis of particle behavior in flowfield

The particle solver based on the discussed theoretical models is tested under various conditions and input parameters. To see the impact of the particle size on the trajectory, particles with different radii from 0.1µm to 50µm (in some cases 20µm) are injected in the flowfield near the stagnation line at the same position. The resulting particle paths are shown in figure 6.5a. The gray lines with arrows represent the stream traces of velocities while the particle movement is shown with dotted lines. The lightest particle of radius 0.1µm deflects very sharply and tries to follow the same path as the flow field velocity. As the particles become larger, deflection reduces accordingly. Particles deviate from the flowfield velocity significantly. It can be seen that, there is a critical size of the particle up to which it will not hit the wall and go out of the flowfield simulated area. However, after making several simulations with different flow field conditions, it is found that this critical radius depends mainly on the flowfield conditions as well as relative radii of particle and wall. The possibility to hit the wall is higher for bigger particles than for the smaller ones.

(a) Trajectories of differently sized particles in flow field

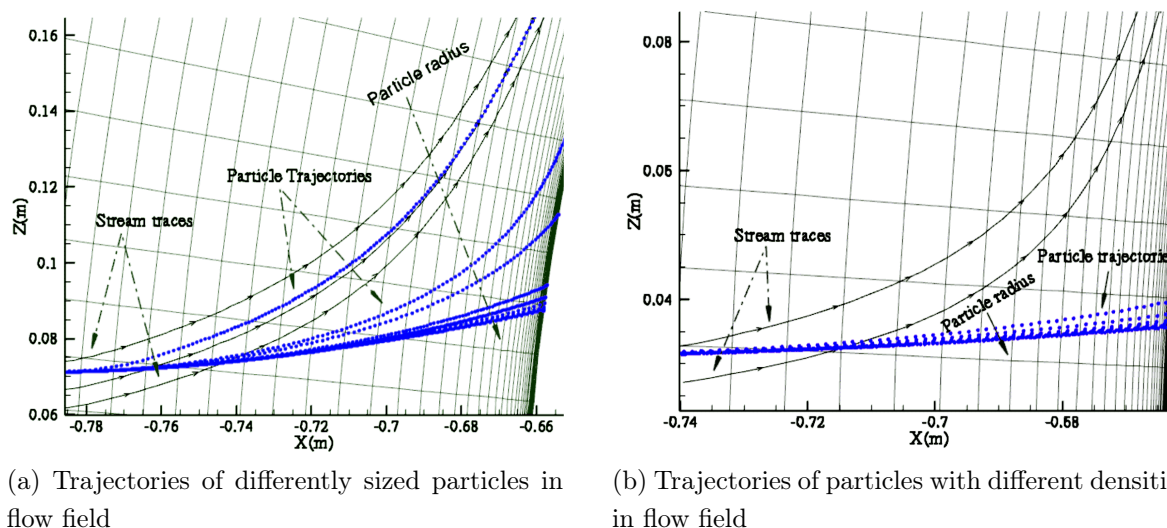(b) Trajectories of particles with different densities in flow field

Figure 6.5: Particle trajectories under different conditions

The possible reason for the deviation in the trajectories of differently sized particles is the drag force acting on the particles. There is significant difference in the drag forces values comparing smaller with larger particles. The relative difference in the drag values increases as the radius of the particle decreases due to their inertia. Larger particles have higher inertia and more force is required to change their trajectories as compared to

6. RESULTS AND ANALYSIS

smaller particles. More precisely, the acceleration of dust particles can be simply related to the local flow conditions as

$$a_c = \frac{SC_dV^2}{2m},\tag{6.1}$$

where m is proportional to D^3 and S is proportional to D^2.

To see the influence of the material, particles with different material densities ranging from 1000 kg/m^3 to 18000 kg/m^3 were injected into the flowfield and the trajectory of the particles were investigated as shown in figure 6.5b. No significant impact on the trajectories of the particles of higher densities was found.

The velocity behavior of differently sized particles across the shock is also analyzed. The velocity plots for differently sized particles are shown in figure 5.4. As the size of the particle increases, the velocity difference between the gas and particle velocities also increases. Downstream of the shock, smaller particles tend to follow the gas velocity but there is no significant influence observed on the bigger particles. The bigger particles retain their initial velocities and there is no deviation in their trajectories is observed.
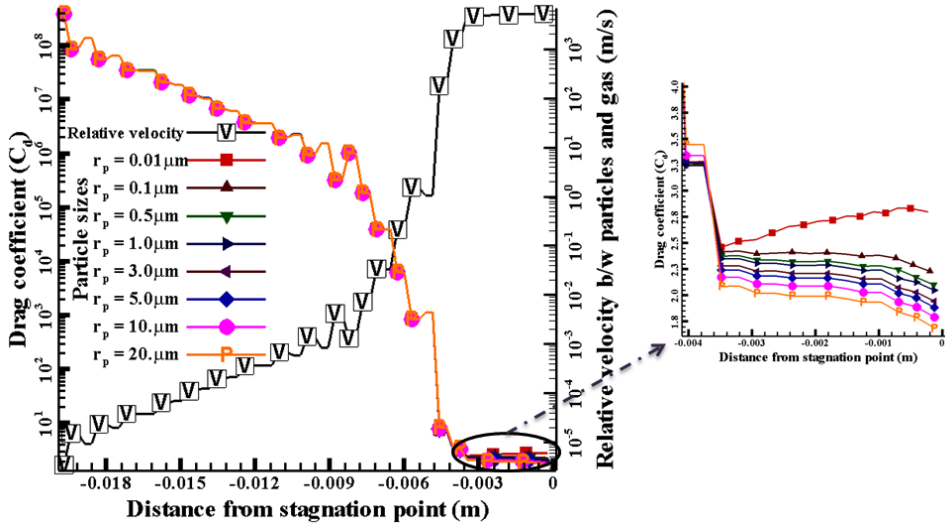
Figure 6.6: Drag coefficients for different sizes of particles along their trajectories

The drag coefficients are plotted for differently sized particles in figure 6.6. The values for drag coefficients look very high upstream the shock. Ideally these values should be zero. These higher values are due to very small values of relative velocity as explained previously and presented in figure 4.3. In reality, this relative velocity should be zero. However, we observe very low values of relative velocity approximately of the order of $\approx 10^{-5}$ in the

flowfield as shown in the same figure 6.6 on the second axis. The truncation and rounding off errors in numerical methods are the primary causes for these values. Keeping in view this problem, as adequate modification was made in the drag force computation as explained previously in section 4.3.1. These modifications were necessary in order to avoid instabilities in drag coefficient computation. However, it is important to mention here that even though the drag coefficients are very high for small relative velocities, the drag force is very negligible because it also involves sizes of the particles. Drag forces for differently sized particles are shown in figure 6.7a.

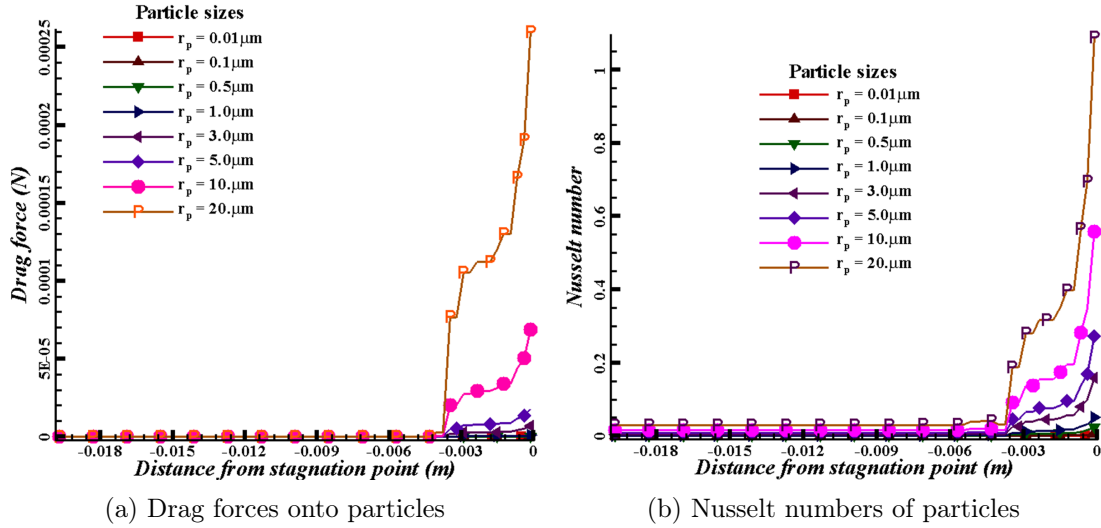(a) Drag forces onto particles   (b) Nusselt numbers of particles

Figure 6.7: Drag force and Nusselt number plots for differently sized particles

Downstream of the shock drag coefficient decreases sharply. This change in drag coefficient values is due to the sudden decrease in flowfield parameters (i.e. velocity, density, pressure and temperature) downstream of the shock. There is a significant difference in the drag coefficient values comparing smaller with larger particles. The relative difference in the drag values increases as the radius of the particle decreases. This is due to the fact that the Reynolds number for the larger particles is higher compared to the smaller particles as shown in figure 6.8b. The drag coefficient gradually starts decreasing near the wall due to the increase in the gas density and also the increase in the Reynolds number of the particles. The behavior of the smaller particle of radius $0.1\mu m$ is quite different from the other particles. This is due to the fact that the size of the particle is so small that it very quickly adapts to the flowfield gas velocity. The relative difference in velocities of the small particle and the gas approaches to very small values resulting in very high values of the drag coefficients.

(a) Particle Mach number in the flowfield

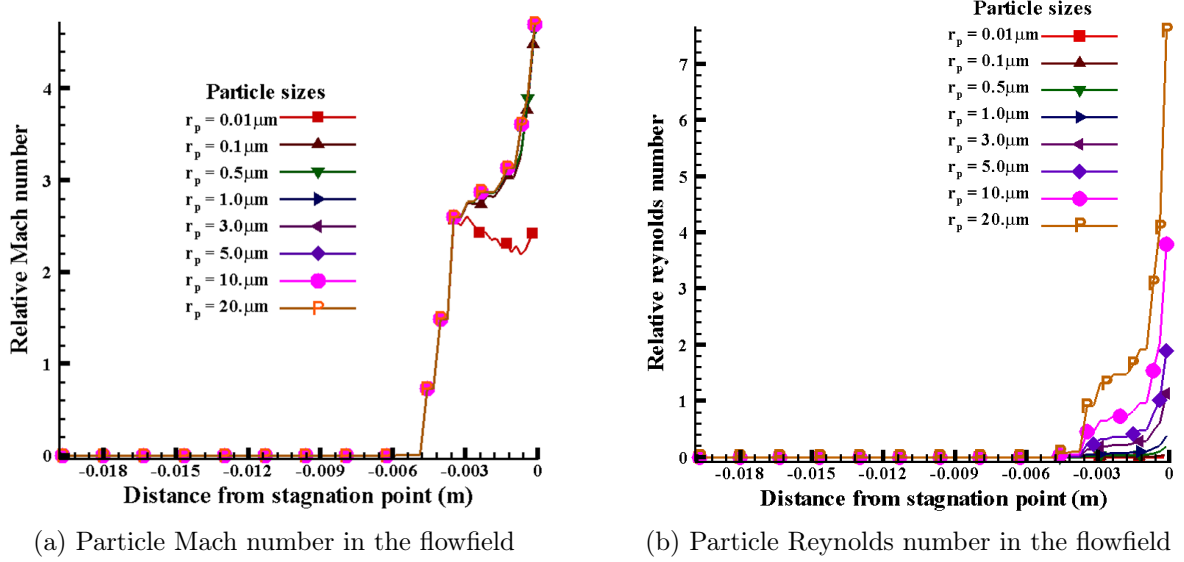(b) Particle Reynolds number in the flowfield

Figure 6.8: Mach and Reynolds number plots for differently sized particles

The Mach number curves of the different particle radii in the flowfield are shown in the figure 6.8a. Initially, the values of the Mach number are negligible because it is a relative Mach number and up to the shock the velocities of the particles and the gas are the same. However, downstream the bow shock, the gas velocity reduces sharply resulting in an increase of the relative Mach number. Near the wall a sharp increase in Mach number is observed for big particles due to significant decrease in the gas velocity while the particle velocity stays high. The smaller particle behaves entirely different. This is due to the fact that the smaller particle relaxes quickly and the velocity difference between this smaller particle and the gas becomes very small. The variation of relative Reynolds number along the trajectory of the particles is shown in figure 6.8b. Smaller particles have lower Reynolds numbers since it is directly proportional to the characteristic length of the object. In our case the characteristic length is the diameter of the particle. The Reynolds number inreases significantly downstream of the shock due to sudden increase in the relative velocity of the particle. It increases again sharply near the wall due to the high flow field density because Reynolds number is directly proportional to the gas density.

The variations in Knudsen number ($Kn \approx \frac{M_{rlt}}{R_{rlt}}$) for different particles in the flowfield up to the wall can be seen in figure 6.9. The values remain high along all of the trajectory of the particles. In general, our current case can be treated as transitional or at some points as rarefied regime. Only near the wall, the Knudsen number decreases due to the
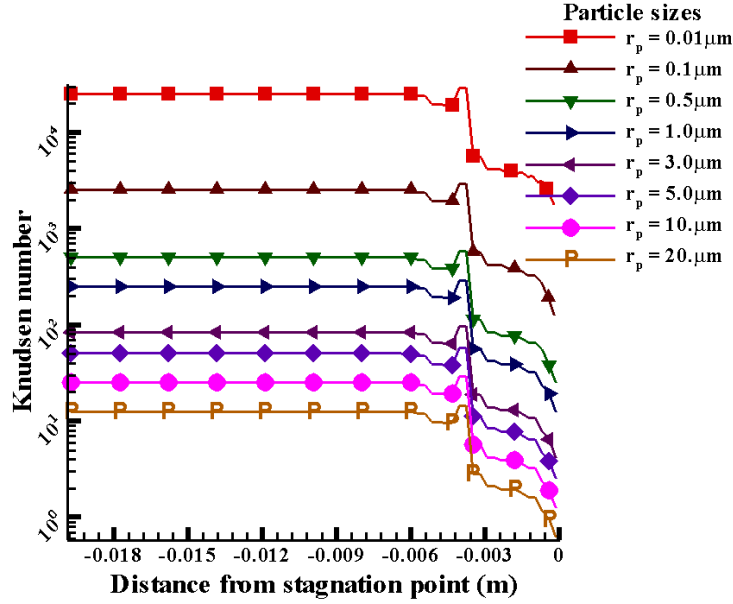
Figure 6.9: Knudsen number for the different sizes of the particles along their trajectories

higher values of the gas density near the wall. As the particle size increases, the Knudsen number decreases quite linearly. However, the very small particles act quite differently and their values tend to increase near the wall.
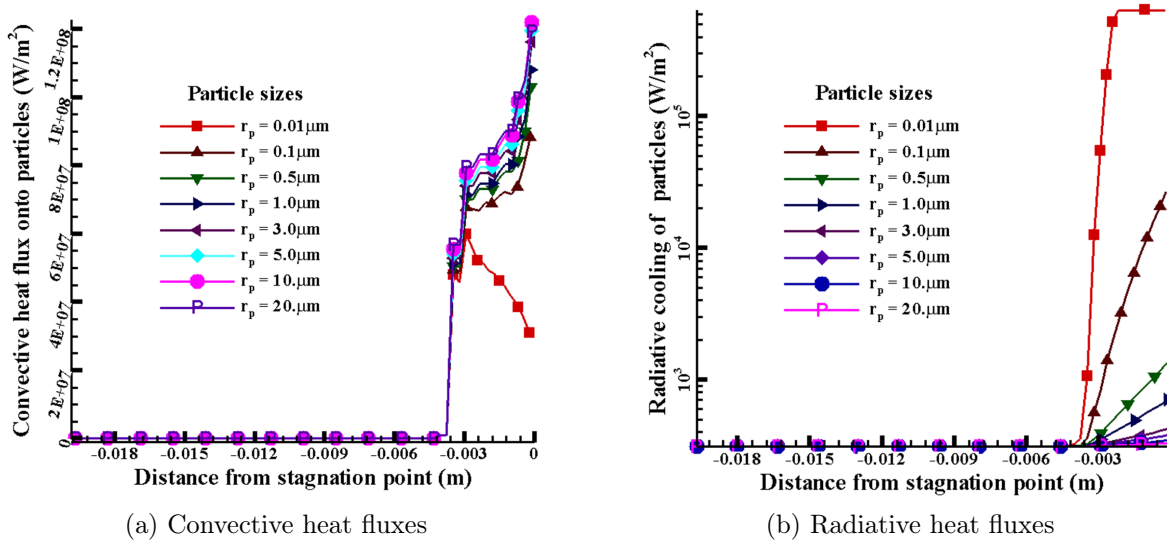
(a) Convective heat fluxes

(b) Radiative heat fluxes

Figure 6.10: Heat fluxes of different sized particles in the flow field

The computation of the heat fluxes and the temperatures of the particles in high temperature gas flows is important for predicting interaction of particles with vehicle surface.

6. RESULTS AND ANALYSIS

The convective heat fluxes for differently sized particles are presented in figure 6.10a. The particles are injected with the same velocity as that of vehicle atmospheric velocity, in order to simulate actual entry flows. Therefore, on the upstream of the shock, heat fluxes on the particles are zero. However, downstream the shock, the heat fluxes increase significantly due to the high temperature of the flowfield and the velocity difference. The convective heat fluxes to the smaller particles are lower as compared to bigger particles. This arises since the volume to surface ratio of a sphere is proportional to its radius. Therefore, more energy can be stored in bigger particles. As the wall temperature is set to 1500 K, the flowfield temperature decreases in the boundary layer. However, particle temperature is still higher than the gas temperature.

The radiative heat flux is shown in figure 6.10b. Unlike the convective heat transfer, the radiative heat transfer for the smaller particle is higher than for the bigger particles. This arises since the volume to surface ratio of a sphere is proportional to its radius. Therefore, more energy can be stored in bigger particles. The radiative heat flux is directly proportional to the fourth power of the particle temperature. The particle temperature in the flowfield downstream of the shock becomes very high and the radiative heat flux also increases. Here we can observe that as the radius of the particle increases, the difference in the radiative heat flux decreases and vice versa. For the smaller particle, radiative heat fluxes are very high and their values are of the same order as those of the convective heat fluxes. It could be said that smaller particles at some points during their trajectory reach a state of thermal equilibrium.

In figure 6.11 temperature plots for different particle sizes are shown. From the contour plot of the flowfield, we know that the maximum value of the gas temperature is around 7600 K and the free stream gas temperature is 288 K. Downstream of the shock, small particles relax quickly while the temperature of the bigger particles still increases. From the heating and particle temperature, it is found that the capability to store energy in the bigger particles is higher than in the smaller particles due to the volume to surface ratio. As the particle radius decreases, its temperature increases and hence the radiative fluxes increase. The temperatures of the particles greater than 2μm do not reach the vaporization temperature i.e. 2500 K. Therefore, no phase change of the bigger particles in the flowfield is expected in this condition.
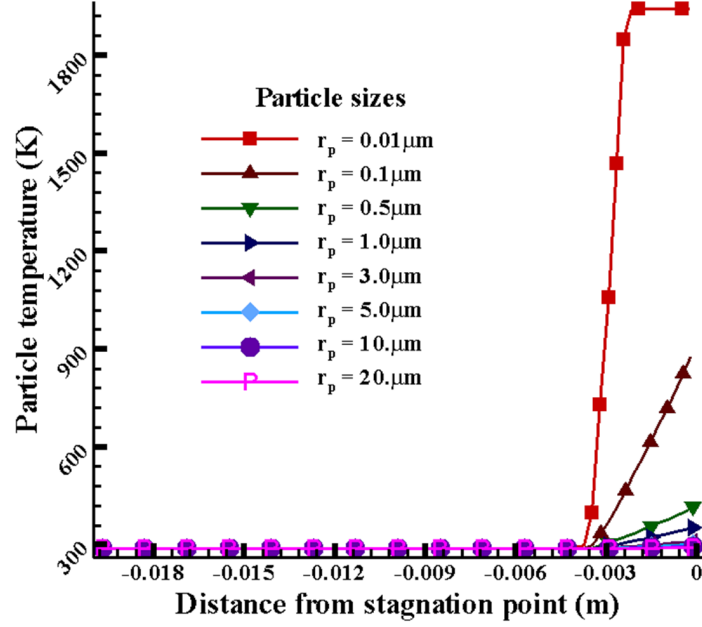
Figure 6.11: Temperature of differently sized particles along their trajectories

6.2 Particle-wall interaction

To determine the heat fluxes to the wall due to impingement of the particles, the particles of the same radii (0.4μm) are injected continuously at the inflow boundary. The heat fluxes are also computed along the curvature of the wall in order to have complete information of the energy transferred to the wall from the stagnation point up to the outflow boundary. In figure 6.12 heat fluxes to the wall computed by SINA for the flowfield gas and heat fluxes due to impinging particles are shown on different axis.

The overall trend of both heat fluxes is the same. However the heat flux from particles is quite low (roughly of the order of 8%). At the stagnation point, the heat flux due to particle is maximum. The reason is that, gas velocity is zero at this point and the relative difference in velocities of particles and gas is maximum. Particle heat flux curve is not very smooth near the stagnation area. The reason for this is, that we have axis symmetric 3D grid. The cells near the stagnation point have a comparatively small volume. The number of particles injected in a cell is proportional to the volume. Therefore frequency and number of particles hitting the wall near the stagnation point is also not high as compared to the particles injected near the outflow area. It is also worthy to mention here that particles with radii 0.4μm* are used for simulations. However, particles with

---

*The mode radius (r_m) of dust particles in Martian atmosphere is around 0.4μm [58]
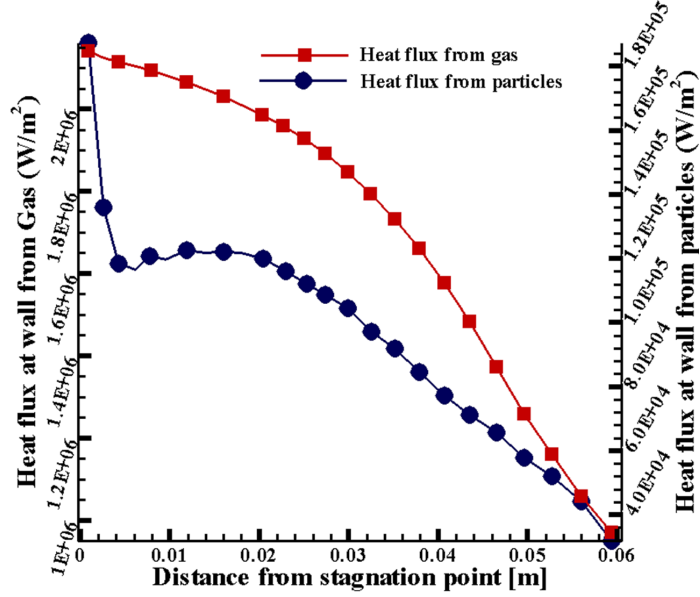
Figure 6.12: Comparison of Fourier heat fluxes due to gas with the energy transferred due to particles of radii 0.4μm along the curvature of the wall
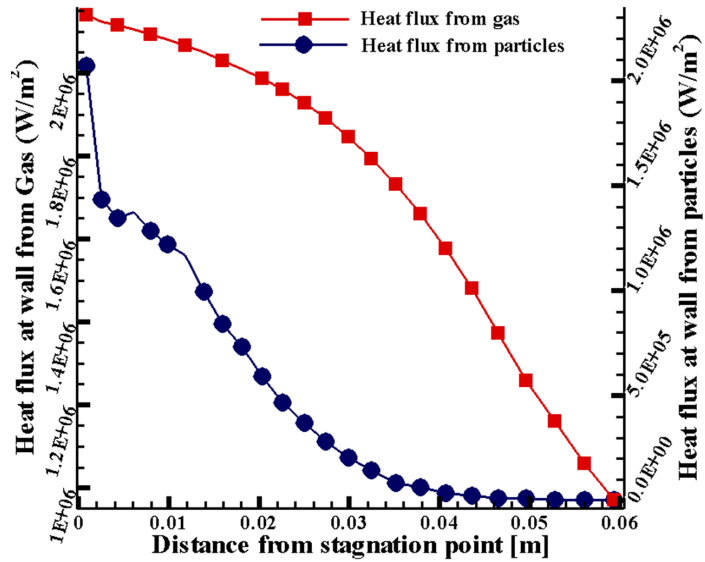
Figure 6.13: Comparison of Fourier heat fluxes due to gas with the energy transferred due to particles of radii 3μm along the curvature of the wall

bigger sizes are also present in the Martian atmosphere even though the number density of these larger particles is relatively very low (explained in detail in section 4.1). In order to see the impact of these particles onto wall of vehicle, particles with radii 3μm are also simulated in flowfield and results are presented in figure 6.13. From this figure it is clear

that heat fluxes from the particles are relatively very high and the values of heat fluxes from gas and particles are of the same order.

Based on the current available data, the number density of larger particles is relatively very low, hence fluxes due to impingement of particles are not significant. However the current work revealed the fact that particle sizes and loading ratio have a significant impact on the heat flux computation. Therefore, it is recommended to obtain as much as possible information about the dust particles in Martian atmosphere. This is very important for the successful mission that the heat fluxes onto the vehicle surface during hypersonic reentry should be addressed appropriately.

Besides heating effects, the particle could damage the wall surface. The bigger particles are not highly heated and also their velocity is not strongly reduced by shock layer, these could produce crater depth in the wall. Due to unavailability of material data, this phenomenon is not yet implemented in the code and left for future work.

Chapter 7

Summary and Conclusions

7.1 Summary

The impact of solid particles onto vehicles entering the Martian atmosphere at hypersonic
velocities is studied and discussed in detail. Two phase flow modeling is necessary in order
to take into account particle interaction with the gaseous flowfield. The one phase is the
gaseous flow field and the solid particles are treated as the second phase. For the flowfield
simulation, SINA code is used. This code not only has the capability to simulate viscous
hypersonic flows using the Navier-Stokes equations but also has the models to account for
thermal and chemical non-equilibrium flows. The entry velocity to Mars is hypersonic,
therefore the thermal and chemical non-equilibrium effects have to be taken into account.
Initially, SINA was developed to simulate air as gaseous flowfield medium only. The
eleven species of air were considered and the information for the species were hard coded.
There was no possibility to use SINA for gases other than air. Therefore, the first task
was to extend the capabilities of SINA in order to use it for other gases like CO_2 in our
case. The modifications in the code are made in such a way that all the gaseous flowfield
information, i.e. species composition, physical properties, inflow conditions, grid info etc.
required by the solvers are moved to inflow data files. In the current version of SINA code
all the solvers being implemented are independent of any type of flow and could be used to
simulate any gas with any number of species. This was necessary otherwise the simulation
of Martian entry flows was not possible. The solvers implemented in the code are loosely
coupled with each other. This type of coupling provides us the liberty to introduce
different modules in the code without any problem. The mathematical models used for

7. SUMMARY AND CONCLUSIONS

the different solvers along with their description are also presented in this thesis. The new CVE (Chemical, Vibration and Electron) developed is also discussed and presented.

To simulate Martian entry flows, only CO_2 is taken into account because it is the main constituent of the Mars atmosphere. At 1 atmospheric pressure dissociation starts at about 1800 K for CO_2. Keeping in view the fact that entry velocity in the Mars atmosphere is around 5-7 km/s, the dissociation of CO_2 have to be considered. Therefore, the five species model (carbon dioxide (CO_2), molecular oxygen (O_2), carbon monoxide (CO), oxygen (O) and carbon (C)) is implemented. The Park's two temperature model is used for the computation of the reaction rate coefficients based on the modified Arrhenius law. The transport properties are computed based on the Chapman-Enskog theory. The values needed for the collision integrals are taken from Wright [30]. The CO_2 is the three atomic molecule but previously the SINA code there was no provision to take into account vibrational energies for the three atomic molecule. A necessary modifications in the code are made and capabilities of the code are extended in order to simulate vibrational energies of molecules having three atoms.

There are two different ways with which the particle solver interacts with the flowfield solvers. These are named as one-way coupling and two-way coupling. In one-way coupling there is no effect onto the gaseous flowfield because of the particles. The particle solver extracts the necessary information from the converged solution of the flowfield for its simulation. However, in two-way coupling both phases interact with each other. The particles may change or modify the flowfield parameters like velocity, temperature etc as a result of interaction with it during simulation. To take into account these modifications, the flowfield solvers are again simulated to find a new solution in order to cope with the changes or modifications introduced by the particle solver. The both solves iterated simultaneously and continuously until a converged solution is achieved.

The Lagrangian approach is used for the particle phase simulation. This approach has many advantages over the other approaches like Eulerian approach because it involves a small number of empirical equations and is more suitable for providing detailed information of the discrete phases. Not only the one-way coupling but also two-way coupling is taken into account. The different particle distribution scheme are discussed due to the fact that sizes of the injected particles may vary from each other. The particles could be injected either in a limited numbers in order to analyze particle trajectories with detailed parametric studies or the may also be injected continuously to simulate flow fields containing solid particles. The continuous injection has also two options: either the particles could be injected all along the inflow periphery as it is needed to simulate vehicle entry

flows into dusty atmosphere or the user defined geometrical shapes like circle or square may also be used for solid particle injection into the flowfield (This may be required for powder injection into plasma generators or solid particle simulation in nozzle flows). The task that is necessary for the Euler-Lagrangian modeling is to locate the particles in the flowfield after injection. A mathematical model based on the vector products of all the sides of the volume cell is developed and implemented in the code and it works perfectly and efficiently for the location of the particles. The translational motion of the particle is governed by Newtons second law. The particle movement is characterized by transitional and rarefied flow properties due to the low gas densities and small particle sizes. The Henderson's drag correlation is implemented in the code because it has the capability to compute the drag coefficient not only in the continuum region but also it predicts drag values very good in the transitional and rarefied regions. Due to hypersonic entry flows, a strong bow shock is developed in front of the vehicle and the gas behind the shock heated up to the very high temperatures. Because of this effect, the particles entering the flowfield also experiences very high temperatures. An adequate heat transfer model is also included for particle temperature computation in high temperature gas flows. The rarefaction correction is also included in the Nusselt number computation for convective heat transfer model. It is also worthy to mention here that Nusselt number is the key parameter for measure of convective heat transfer. Many correlation for the computation of Nusselt number are available. However all of them are developed for subsonic flows. It cannot be directly used for solid particle simulation in high temperature gas flows because of relative supersonic flow between the gas and particles after the shock. Usually this effect is ignored however the results may vary significantly if this phenomenon is ignored. A stagnation point shock correlation is also introduced to take care of this effect. In the end of this chapter, particle-wall interaction is discussed and different models being implemented in the code are presented.

Verification and validation are the primary means to assess accuracy and reliability in computational simulations by comparison with known solutions and is centered on the accumulation of evidence that a specific calculation is correct and accurate. It implies detailed surface and flowfield comparison with experimental or published results from different external resources. Therefore, comparison and verification is done for all the new solvers being implemented in the code. To compare flowfield solver for the Martian atmosphere, CEA (Chemical Equilibrium with Applications) code developed by NASA is used. This is one of the best code for determination of chemical equilibrium of all the species of the composition for various ranges of the temperatures. The results are very

close to each other and a very good agreement is found between the the two codes. The TINA code of Fluid Gravity Engineering ltd. is used in order to verify the particle solver of the SINA code. The particle momentum and heating of the particles are compared. The results from both codes are in accordance as far as particle movement or particle trajectories in the flowfield is concerned. However, a marked difference is observed in the results while comparing the heating of the particles. The particle solver of the SINA code shows around 30 to 40% higher values of the particle heating as compared to the TINA code. The variation in the results is attributed to the parameters being used by the particle solver from flowfield gas. Due to relative velocity difference in the gas and particle, the development of the local shock may introduce extra heating to the particle. There is no reference availabe for such kind of problem and no CFD code was available for the result comparison purposes. The GA Bird' code DS2V is decided to be used for this purpose. For DSMC simulations particles of smaller sizes are placed in high temperature gas flows and the particle solver is also simulated with the same conditions. The results obtained by taking into account local particle heating are relatively closer to the DSMC results. Therefore, for hypersonic entry flows, it is important to take into account local heating onto the particle because of the relative velocity between the particle and the gas velocity.

7.2 Conclusions

- Capabilities of SINA code are extended to simulate

  1. Vibrational energy computation for three atomic molecule.
  2. Martian atmosphere.
  3. Solid particles (with different models).

- A code to code comparison of CO_2 and particle solver are made with different resources.

- The particle movement is characterized by transitional and rarefied flow properties due to the low gas densities and small particle sizes.

- The effect of local shock due to high speed relative speed may introduce higher temperature to particle.

- Due to high particle temperature, phase change of the particle of smaller radii is observed.

- The ratio of heat flux due to impingement of the particles compared to heat flux because of flowfield gas is found to be very low. Therefore, additional heat flux due to impingement of particles is negligible. However particles with larger radii may have significant heat fluxes onto wall of the vehicle. Therefore, it is important to obtain as maximum as possible the accurate information about dust mass mixing ratio and particle size distribution in Mars atmosphere.

- The particles may also change the geometry of the surface at micro level. Due to impingement of the particles on the vehicle surface, the particles will increase the roughness, which will change the flowfield behavior around the vehicle. In addition boundary layer transition will occur from laminar to turbulent that may result not only increasing the heat flux but also in modifying the aerodynamic characteristic of the flowfield surrounding the object. In this way, the particles have an indirect effect on the vehicle and it is very important to study these effects associated with dust particles during atmospheric entry flows.

References

[1] "Missions to Mars." URL `http://marsprogram.jpl.nasa.gov/missions/log/`. 19

[2] "Missions to Mars." URL `http://www.planetary.org/explore/topics/our_solar_system/mars/missions.html`. 19

[3] "NASA missons to Mars." URL `http://www.nasa.gov/mission_pages/mars/`. 19

[4] "The ESA ExoMars mission." URL `http://exploration.esa.int/`. 19

[5] "The Russion and Chinese Joint Mission to Mars (Fobos-Grunt)." URL `http://spectrum.ieee.org/aerospace/space-flight/`. 19

[6] BRAUN, R., POWELL, R., AND HARTUNG, L. "Effect of Interplanetary Trajectory Options on a Manned Mars Aerobrake Configuration." Technical report, NASA TP 3019, Aug. 1990. 21

[7] ROBERT, M., CONWAY, B., AND JAMES, B. "Some Effects of Global Dust Storms on the Atmospheric Circulation of Mars." ICARUS, International Journal of Solar System Studies, volume 50, 1982:pp. 332–367. 22

[8] SCHOFIELD, J.T. "The Mars Pathfinder Atmospheric Structure Investigation/Meteorology (ASI/MET) Experiment." Science, volume 278, 1997:pp. 1752–1757. 22

[9] FRANCOIS, F., FREDERIC, H., RICHARD, F., CHRISTOPHE, H., AND OLIVIER, T. "Improved General Circulation Models of the Martian Atmosphere from the Surface to above 80 km." Journal of Geophysical Research-Planet, volume 104, 1999:pp. 155–176. 22

[10] Fernández, W. "Martian Dust Storms: A Review." In Seventh UN/ESA Workshop on Basic Space Science. 1997. 22

[11] Robert, M.H. and Conway, B.L. "Some Effects of Global Dust Storms on the Atmospheric Circulation of Mars." ICARUS, International Journal of Solar System Studies, volume 50, 1982:pp. 322–367. 22

[12] Wuttke, M., Keller, H.U., Markiewicz, W.J., Petrova, E., Richter, K., and Thomas, N. "Properties of dust in the Mars atmosphere : a revised analysis of Phobos/KRFM data." Planetary and Space Science, volume Vol. 45, No. 3, 1997:pp. 281–288. 22

[13] Vasilevskii, E.B., Osiptsov, A.N., Chirikhin, A., and Yakovleva, L. "Heat Exchange on the Front Surface of a Blunt Body in a High-Speed Flow Containing Low-Inertia Particles." Journal of Engineering Physics and Thermophysics, volume Vol. 74, No. 6, 2001. 22

[14] Gorimir, G.C. Problems Of Aerothermoballistics, Radiation , Heat and Mass Transfer for Planet Sample Return Missions. ISTC N 1549-00. Research Institute of Mechanics (NIIMekh), 2003. 23

[15] Keller, K.e.a. "Dust Particle Erosion during Mars Entry." In 6th European Workshop on Thermal Protection Systems and Hot Structures. 2009. 23

[16] Endlich, P. "Untersuchungen zur experimentellen Simulation des Eintritts von Raumflugkörpern in die Marsatmosphäre." Ph.D. thesis, Universität Stuttgart, 2007. 23

[17] Papadopoulous, P., Tauber, M., and Chang, I.D. "Heatshield Erosion in a Dusty Martian Atmosphere." Journal of Spacecraft and Rockets, volume 30, No. 2, 1993:pp. 140–151. 23

[18] Palmer, G., Chen, Y.K., Papadopoulous, P., and Tauber, M. "Reassessment of Effect of Dust Erosion on Heatshield of Mars Entry Vehicle." Journal of Spacecraft and Rockets, volume 37, No. 6, 2000:pp. 747–752. 23

[19] Grau, T. "Numerische Untersuchung von Plasmawindkanalströmungen zur Wiedereintrittssimulation." Ph.D. thesis, Ph.D. thesis, Institut für Raumfahrsysteme, Universität Stuttgart, Germany, 2000. 27, 30, 124

REFERENCES

[20] BAUDER, U., FERTIG, M., AND AUWETER-KURTZ, M. "Examination of the Coupling of the Loosely Coupled Navier-Stokes Code SINA." In 40th Thermophysics Conference, Seattle, Washington, volume AIAA 2008-3931. 23 - 26 June 2008. 27

[21] BAUDER, U., MAJID, A., FERTIG, M., AND AUWETER-KURTZ, M. "Improvement and Extension of the Loosely Coupled Navier-Stokes Code SINA to Different Gases." In 10th AIAA/ASME Joint Thermophysics and Heat Transfer Conference,Chicago, Illinois, volume AIAA 2010-4518. 28 June - 1 July 2010. 27, 29

[22] PFEIFFER, B., FERTIG, M., WINTER, M., AND AUWETER KURTZ, M. "PARADE a program to calculate the radiation of atmospheric re-entry in different atmospheres." In ESA-SP-533. European Space Agency (ESA), 2003. 29

[23] GOGEL, T., DUPUIS, M., AND MESSERSCHMID, E. "Radiation transport calculation in high enthalpy environments for two-dimensional axisymmetric geometries." Journal of Thermophysics and Heat Transfer, volume vol. 8, no. 4, 1994:pp. 744–750. 29

[24] BERTIN, J.J. Hypersonic Aerothermodynamics. AIAA education series, 1994. 31

[25] WILLIAN, H.P. AND ET AL. Numerical Recipes : The art of Scientific Computing, volume edition 3. Cambridge University Press, 2007. 32

[26] YOS, J. "Transport Properties of Nitrogen, Hydrogen, Oxygen and Air to 30000K." Technical report, Tech. Rep. AD-TM-63-7, Research and Advanced Development Division AVCO Corporation, 1963. 32

[27] FERTIG, M., DOHR, A., AND FRÜHAUF, H. "Transport Coefficients for High-Temperature Nonequilibrium Air Flows." Journal of Thermophysics and Heat Transfer, volume vol.15 no.2, 2001:pp. 148–156. 32, 51

[28] GUPTA, R., YOS, J., THOMSON, R., AND LEE, K. "A Review of Reaction Rates and Thermodynamic Transport Properties for an 11-Species Air Model for Chemical and Thermal Nonequilibrium Calculations to 30000 K." Technical report, NASA Reference Publications 1232, 1990. 33

[29] FERTIG, M. "Analyse von Transportkoeffizienten modellen für Luft in einem Temperaturbereich von 25 K-30000 K." Technical report, Studientarbeit, Institut für Raumfahrtsysteme, Stuttgart, 1994. 33

[30] MICHAEL, J., HELEN, H., AND DAVID, W. "Recommended Collision Integrals for Transport Property Computations Part 2, Mars and Venus Entries." AIAA Journal, volume 45, No. 1, 2007:pp. 281–288. 33, 51, 104

[31] PARK, C. "Assessment of Two-Temperature Kinetic Model for Ionizing Air." In AIAA-Paper 87-1574. 1987. 33, 45

[32] KANNE, S., FRÜHAUF, H.H., AND MESSERSCHMID, E. "Thermochemical Relaxation through Collisions and Radiation." Journal of Thermophysics and Heat Transfer, volume Vol. 14, No. 4, Oct, 2000:p. 464470. 36

[33] PARK, C. Nonequilibrium Hypersonic Aerothermodynamics. Wiley Interscience Publication,New York, 1990. 36, 37

[34] MILLIKAN, R. AND WHITE, D. "Systematics of Vibrational Relaxation." The Journal of Chemical Physics, volume Vol. 39, No. 12, 1963:pp. 3209–3213. 36

[35] RAPP, D. "Interchange of Vibrational Energy between Molecules in Collisions." J. Chem. Physics, volume Vol. 41. No. 5, 1965. 37

[36] RIEDEL, U. "Numerische Simulation reaktiver Hyperschallstr¨omungen mit detaillierten Reaktionsmechanismen." Ph.D. thesis, Universität Heidelberg, Germany, 1992 (in German). 38

[37] Private communication with Uwe Bauder (a PhD student in Institute of Space Systems, Universität Stuttgart Germany). 40

[38] MICHAEL, L. "An efficient General Purpose Method for the Integration of Stiff Ordinary Differential Equations." AIChE journal, volume 22, No. 3, 1976:pp. 594–597. 40

[39] CATALFAMO, C., BRUNO, D., COLONNA, G., LARICCHIUTA, A., AND CAPITELLI, M. "High Temperature Mars Atmosphere. Part II: Transport Properties." The European Physical Journal D, volume 54, 2009:p. 613621. 43, 44

[40] PARK, C., JOHN, T.H., RICHARD, L.J., AND CANDLER, G. "Review of Chemical-Kinetic Problems of Future NASA Missions,II: Mars Entries." Journal of Thermophysics and Heat Transfer, volume Vol. 8, No. 1, 1994:pp. 9–23. 43

REFERENCES

[41] DRUGUET, M.C. "Prediction of the flow field over an orbiter entering the Mars atmosphere." Shock Waves, volume Volume 20, Issue 3, 2010:pp. 251–261. 44

[42] CHARBONNIER, J.M. "Workshop 2004 "Radiation of High Temperature Gas", TC3:." Technical report, Update of the axially symmetric test case for high temperature gas radiation prediction in Mars atmosphere entry, 2004. 44, 45, 90

[43] "NASA CEA Thermobuild Table." URL `http://www.grc.nasa.gov/WWW/CEAWeb/ceaThermoBuild.htm`. 45, 46, 48

[44] PARK, C. "Convergence of Computation of Chemical Reacting Flows." Progress in Astronautics and Aeronautics, volume Vol. 103, 1986:pp. 478–513. 45, 52

[45] COX, J., WAGMAN, D., AND MEDVEDEV, V. CODATA Key Values for Thermodynamics. Hemisphere Publishing Corp. New York, 1989. 46

[46] "National Institute of Standards and Technology , NIST Chemistry WebBook." URL `http://webbook.nist.gov/chemistry/`. 46, 48

[47] HEERMANN, D., editor. Computer Simulation Methods in Theoretical Physics. Springer-Verlag New York, Inc., New York, NY, USA, 1986. 46

[48] FERTIG, M. "Modellierung reaktiver Prozesse auf Siliziumkarbid-Oberflächen in verdünnten Nichtgleichgewichts-Luftströmungen." Ph.D. thesis, Universität Stuttgart, 2005. 47

[49] ANDERSON, J.D. Hypersonic and High Temperature Gas Dynamics. McGraw-Hill Book Company, 1989. 48

[50] BRDICKA, R. "Grundlagen der physikalischen Chemie." Technical report, Deutscher Verlag der Wissenschaften, Berlin, 12. Aufl., 1973. 49

[51] FROHN, A. "Einführung in die Technische Thermodynamik." Technical report, Aula Verlag, Wiesbaden, Zweite Aufl., 1989. 49

[52] HIRCHFELDER, J., CURTISS, C., AND BIRD, R. Molecular Theory of Gases and Liquids. Wiley Interscience Publication,New York, 1954. 50

[53] CAMAC, M. CO2 Relaxation Processes in Shock Waves, Fundamental Phenomena in Hypersonic Flow. Hall,J.G. Cornell University Press, Ithaca, 1966. 52, 55

[54] KNAB, O., FRÜHAUF, H.H., AND JONAS, S. "Multiple Temperature Descriptions of Reaction Rate Constants with Regard to Consistent ChemicalVibrational Coupling." In AIAA-Paper 92-2947. Jul. 1992. 53

[55] KNAB, O., FRÜHAUF, H.H., AND MESSERSCHMID, E.W. "Validation of a Physically Consistent Coupled Vibration-Chemistry-Vibration Model for Ionized Air in Thermo-Chemical Nonequilibrium." In AIAA-Paper 93-2866. Jul. 1993. 53

[56] HOLLAS, J.M. Basic atomic and molecular spectroscopy. Royal Society of Chemistry, 2002. 54

[57] CANDLER, G. "Computation of Thermo-Chemical Nonequilibrium Martian Atmospheric Entry Flows." AIWASME 5th Joint Thermophysics and Heat Transfer Conference, Seattle, WA, June 18-20, 1990. 54

[58] ALEXANDER, M. "Mars Transportation Environment Definition Document." In NASA / TM–2001-210935. March 2001. 58, 59, 60, 90, 99

[59] WÖRNER, M. "A Compact Introduction to the Numerical Modeling of Multiphase Flows." Wissenschaftliche berichte fzka 6932, Forschungszentrum Karlsruhe, Nov. 2003. 58, 59

[60] TSIRKUNOV, Y. AND VEREVKIN, A. "Computational Simulation of the Unsteady Gas - Particle Flow in a Hypersonic Shock Tunnel." In 6th International Conference on Multiphase Flow, ICMF 2007. Leipzig, Germany, July 9 . 13, 2007 2007. (PS3-8). 61, 72

[61] HENDERSON, C.B. "Drag Coefficients of Spheres in Continuum and Rarefied Flows." AIAA Journal, volume Vol. 14, No. 6, 1976:pp. 707–708. 62

[62] MAJID, A., BAUDER, U., STINDL, T., FERTIG, M., HERDRICH, G., AND RÖSER, H.P. "Development of Two Phase Solver Accounting for Solid Particles in Continuum Flows." In 40th Thermophysics Conference, Seattle USA. AIAA 2008-4105. 65

[63] ZHOU, Q. AND LESCHZINER, M. "An Improved Particle-Locating Algorithm for Eulerian-Lagrangian Computations of Two-Phase Flows in General Coordinates." International Journal of Multiphase Flow, volume 25, 1999:pp. 813–825. 66

REFERENCES

[64] CHEN, X. "Efficient Particle Tracking Algorithm for Two-phase Flows in Geometries using Curvilinear Coordinates." Numerical Heat Transfer, Part A: Applications: An International Journal of Computation and Methodology, volume Volume 32, Issue 4, 1997:p. 387 405. 66

[65] CHORDÁ, R., BLASCO, J.A., AND FUEYO, N. "An Efficient Particle-Locating Algorithm for Application in Arbitrary 2d and 3d Grids." International Journal of Multiphase Flow, volume Volume 28, Issue 9, 2002:pp. 1565–1580. 66

[66] CROWE, C., SOMMERFELD, M., AND TSUJI, Y. Multiphase Flows with Droplets and Particles. CRC Press, Boca Raton, 1998. 66, 68, 69, 70

[67] MAJID, A., BAUDER, U., STINDL, T., FERTIG, M., HERDRICH, G., AND RÖSER, H.P. "Study of Solid Particle Behavior in High Temperature Gas Flows." In 6th European Symposium on Aerothermodynamics for Space Vehicles. Versailles, France. Nov 3-6, 2008. 68, 69

[68] VASILEVSKII, E.B.AND DOMBROVSKII, L., MIKHATULIN, D., AND POLEZHAEV, Y.V. "Heat Transfer in the Neighborhood of the Stagnation Point Under Conditions of Hypersonic Heterogeneous Slip Flow Past Bodies." High Temperature, volume Vol. 39, No. 6, 2001:pp. 860–873. Translated from Teplofizika Vysokikh Temperatur, Vol. 39, No. 6, 2001, pp. 925-938. 68

[69] RUDINGER, G. "Fundamentals and Applications of Gas-Particle Flow." In GARDograph No. 222 on Flow of Solid Particles in Gases. AGARD-AG-222, 1976. 68

[70] RANZ, W. AND MARSHALL, W. "Evaporation from Drops(Part II)." Chemical Engineering Progress, volume Vol. 48, No. 4, 1952:pp. 173–180. 68, 69

[71] MAJID, A., BAUDER, U., FERTIG, M., HERDRICH, G., AND RÖSER, H.P. "Modeling of Dusty Plasma Flow and Determination of its Impact on Heat Shield Materials." In Advances in Applied Plasma Science, Vol.7. 2009. 70

[72] MAJID, A., BAUDER, U., FERTIG, M., HERDRICH, G., AND RÖSER, H.P. "Particle Wall Interactions in Dusty Hypersonic Entry Flows." Frontier of Applied Plasma Technology, volume Vol.3 No.1, January 2010. 71

[73] Tsirkunov, Y.M., Panfilov, S.V., and Klychnikov, M.B. "Semi empirical Model of Impact Interaction of a Disperse Impurity Particle with a Surface in a Gas Suspension Flow." Journal of Engineering Physics and Thermophysics, volume 67, No. 5-6, July 9 . 13, 2007 1994:pp. 1018–1025. (PS3-8). 72

[74] Keller, K., Desjean, M., Omaly, P., Marraffa, L., Esser, B., Gülhan, A., Montois, I., and Beck, J. "Dust Particle Erosion during Mars Entry." In 6th European Workshop on Thermal Protection Systems and Hot Structures, Stuttgart-Germany. April 1-3, 2009. 73

[75] "NASA Chemical Equilibrium with Applications (CEA) code." 78

[76] Bird, G. URL `http://sydney.edu.au/engineering/aeromech/dsmc_gab/`. 84

[77] Bird, G. Molecular Gas Dynamics and the Direct Simulation of Gas Flows. Clarendon Press,Oxford, 1994. 84

[78] "US Standard Atmosphere 1976." 85

[79] Wilson, F. "Gas-Surface Interaction Effect on Round Leading Edge Aerothermodynamics." Brazilian Journal of Physics, volume vol. 37, no. 2A, 2007:pp. 337–348. 88

[80] Anderson, W., Thomas, J., and van Leer, B. "A Comparison of Finite Volume Flux Vector Splitting for the Euler Equations." AIAA-Paper 85-0122, 1985. 123

[81] Liou, M.S. "Progress Towards an Improved CFD Method: AUSM+." AIAA-Paper, volume AIAA-95-1701-C, 1995. 124

[82] Liou, M.S. "A Sequel to AUSM: AUSM+." Journal of Computational Physics, volume 129, 1996:pp. 364–382. 124

Personal Contributions

[1] Majid, A., Bauder U., Stindl T., Fertig M., Herdrich, G.and Röser H.-P. "Development of Two Phase Solver Accounting for Solid Particles in Continuum Flows." In *40th Thermophysics Conference*, Seattle USA. AIAA 2008-4105

[2] Majid, A., Bauder U., Stindl T. Fertig M. Herdrich, G. and Röser H.-P.,"Study of Solid Particle Behavior in High Temperature Gas Flows." In *6th European Symposium on Aerothermodynamics for Space Vehicles.* Versailles, France. Nov 3-6, 2008

[3] Majid, A., Bauder, U., Fertig, M., Herdrich, G. and Röser H.-P. "Modeling of Dusty Plasma Flow and Determination of its Impact on Heat Shield Materials." In *Advances in Applied Plasma Science*, Vol.7, 2009

[4] Majid, A.,Bauder, U., Fertig, M., Herdrich, G. and Röser H.-P. "Particle Wall Interactions in Dusty Hypersonic Entry Flows." *Frontier of Applied Plasma Technology*, volume Vol.3 No.1, January, 2010

[5] Bauder, U., Majid, A., Fertig,M. and Auweter-Kurtz,Monika. "Improvement and Extension of the Loosely Coupled Navier-Stokes Code SINA to Different Gases." In *10th AIAA/ASME Joint Thermophysics and Heat Transfer Conference,Chicago, Illinois*, volume AIAA 2010-4518. 28 June - 1 July, 2010

Appendix A

Appendix

A.1 Table for the chemical reactions

Table A.1: Chemical reactions with forward rate coefficients

Chemical reactions	Rate Coefficients $(\frac{m^3}{mol\,s}$ or $\frac{m^6}{mol\,s})$		
Dissociation	C_f	s_f	A_f
$CO_2 + O_2 = CO + O + O_2$	6.90e15	-1.5	63275
$CO_2 + O = CO + O + O$	1.38e16	-1.5	63275
$CO_2 + C = CO + O + C$	1.38e16	-1.5	63275
$CO_2 + CO = CO + CO + O$	6.90e15	-1.5	63275
$CO_2 + CO_2 = CO + O + CO_2$	6.90e15	-1.5	63275
$CO + O_2 = C + O + O_2$	2.30e14	-1.0	129000
$CO + O = C + O + O$	3.40e14	-1.0	129000
$CO + C = C + O + C$	3.40e14	-1.0	129000
$CO + CO = C + O + CO$	2.30e14	-1.0	129000
$CO + CO_2 = C + O + CO_2$	2.300e14	-1.0	129000
$O_2 + C = O + O + C$	1.00e16	-1.5	59500
$O_2 + CO = O + O + CO$	2.00e15	-1.5	59500
$O_2 + CO_2 = O + O + CO_2$	2.00e15	-1.5	59500
$O_2 + O_2 = O + O + O_2$	2.00e15	- 1.5	59500
$O_2 + O = O + O + O$	1.00e16	-1.5	59500
Neutral Exchange			
$CO + CO = CO_2 + C$	2.33e03	0.5	65710
$CO + O = O_2 + C$	3.90e07	-0.18	69200
$CO_2 + O = O_2 + CO$	2.10e07	0.0	27800

A. APPENDIX

A.2 Table for entropy and standard enthalpy of CO_2, CO, O_2, O and C

Table A.2: Entropy S° and standard enthalpy H° data of CO_2, CO, O_2 for the computation of Equilibrium constant

T	CO$_2$		CO		O$_2$	
	S°	H°	S°	H°	S°	H°
298.15	213.787	-393.51	197.66	-110.535	205.149	0
500	234.898	-385.203	212.837	-104.604	220.698	6.086
1000	269.297	-360.11	234.541	-88.848	243.587	22.707
2000	309.29	-302.072	258.714	-53.799	268.772	59.202
3000	334.152	-240.694	273.619	-17.006	284.521	98.117
4000	352.18	-178.002	284.395	20.464	296.271	139.001
5000	366.412	-114.2	292.847	58.348	305.723	181.385
6000	378.353	-48.672	299.821	96.606	313.651	224.884
7000	388.889	19.724	305.814	135.491	320.461	269.069
8000	398.538	92.033	311.133	175.337	326.37	313.315
9000	407.582	168.86	316.058	217.177	331.502	356.874
10000	416.129	250.017	320.823	262.442	335.956	399.138
11000	424.199	334.71	325.574	312.328	339.828	439.745
12000	431.781	421.865	330.367	367.455	343.205	478.542
13000	438.866	510.387	335.189	427.733	346.166	515.525
14000	445.458	599.329	339.979	492.393	348.78	550.788
15000	451.574	687.984	344.651	560.119	351.105	584.479
16000	457.249	775.905	349.113	629.257	353.189	616.767
17000	462.522	862.885	353.285	698.068	355.072	647.823
18000	467.439	948.897	357.113	765.028	356.786	677.804
19000	472.041	1034.008	360.58	829.14	358.357	706.845
20000	476.363	1118.275	363.717	890.277	359.804	735.059
21000	480.43	1201.623	366.608	949.53	361.145	762.531
22000	484.249	1283.716	369.4	1009.571	362.391	789.329
23000	487.81	1363.809	372.308	1075.02	363.555	815.501
24000	491.079	1440.61	375.617	1152.823	364.644	841.091

Table A.3: Entropy S° and standard enthalpy H° data of O and C for the computation of Equilibrium constant

T	O		C	
	S°	H°	S°	H°
298.15	161.06	249.175	158.101	716.68
500	172.2	253.518	168.864	720.882
1000	186.792	264.035	183.279	731.28
2000	201.25	284.888	197.715	752.113
3000	209.706	305.749	206.326	773.372
4000	215.775	326.851	212.65	795.375
5000	220.581	348.397	217.701	818.02
6000	224.598	370.441	221.901	841.062
7000	228.06	392.905	225.49	864.345
8000	231.103	415.696	228.62	887.786
9000	233.811	438.686	231.396	911.357
10000	236.245	461.79	233.904	935.164
11000	238.455	484.982	236.215	959.412
12000	240.482	508.273	238.383	984.334
13000	242.357	531.694	240.446	1010.123
14000	244.104	555.276	242.43	1036.895
15000	245.744	579.045	244.346	1064.679
16000	247.291	603.01	246.2	1093.41
17000	248.755	627.169	247.991	1122.948
18000	250.146	651.509	249.715	1153.105
19000	251.471	676.012	251.367	1183.675
20000	252.735	700.662	252.947	1214.468
21000	253.945	725.452	254.454	1245.362
22000	255.105	750.399	255.895	1276.336
23000	256.223	775.548	257.282	1307.53
24000	257.306	800.988	258.633	1339.286

A.3 Diffusion collision integral $\Omega^{1,1}(\text{Å}^2)$ as a function of temperature of 5 species CO_2, O_2, CO, O and C

Table A.4: Diffusion collision integral $\Omega^{1,1}(\text{Å}^2)$ for temperature range 300 K to 4000 K

Species	T(K)					
	300	500	600	1000	2000	4000
$CO_2 - CO_2$	17.35	14.39	13.66	12.12	10.66	9.47
$CO_2 - O_2$	13.68	11.84	11.36	10.27	9.08	7.97
$CO_2 - CO$	14.18	12.36	11.88	10.77	9.52	8.26
$CO_2 - C$		10.84	10.5	9.52	8.22	7.08
$CO_2 - O$		9.15	8.88	8.12	7.11	6.19
$O_2 - CO$	11.6	10.37	10.02	9.15	7.96	6.76
$O2 - C$		8.33	8.01	7.21	6.222	5.26
$CO - C$		9.01	8.62	7.72	6.57	5.51
$CO - O$		7.4	7.11	6.37	5.42	4.55
$C - C$	12.34	10.5	9.96	8.66	7.14	5.84
$C - O$	10.35	8.82			6.49	5.29

Table A.5: Diffusion collision integral $\Omega^{1,1}(\text{Å}^2)$ for temperature range 5000 K to 20000 K

Species	T(K)					
	5000	6000	8000	10000	15000	20000
$CO_2 - CO_2$	9.13	8.86	8.44	8.12	7.54	7.15
$CO_2 - O_2$	7.64	7.38	6.98	6.69	6.17	5.82
$CO_2 - CO$	7.86	7.54	7.05	6.68	6.04	5.6
$CO_2 - C$	6.72	6.41	6.0	5.67	5.1	4.71
$CO_2 - O$	5.91	5.68	5.34	5.09	4.62	4.33
$O_2 - CO$	6.4	6.12	5.69	5.36	4.8	4.42
$O2 - C$	4.97	4.74	4.4	4.15	3.7	3.4
$CO - C$	5.19	4.94	4.55	4.27	3.77	
$CO - O$	4.29	4.09	3.77	3.53	3.12	2.85
$C - C$	5.43	5.11	4.59	4.17	3.4	2.86
$C - O$		4.56	4.08	3.7	3.02	2.66

A.4   Viscosity collision integral $\Omega^{2,2}(\text{Å}^2)$ as a function of temperature of 5 species CO_2, O_2, CO, O and C

Table A.6: Viscosity collision integral $\Omega^{1,1}(\text{Å}^2)$ for temperature range 300 K to 4000 K

Species	T(K)					
	300	500	600	1000	2000	4000
$CO2 - CO2$	20.35	16.45	15.5	13.58	11.92	10.69
$CO2 - O2$	15.74	13.35	12.76	11.47	10.23	9.15
$CO2 - CO$	16.24	13.92	13.32	12.03	10.74	9.5
$CO2 - C$		12.48	12.08	10.98	9.62	8.36
$CO2 - O$		10.44	10.13	9.29	8.22	7.23
$O2 - CO$	13.11	11.6	11.19	10.25	9.13	7.93
$O2 - C$		9.62	9.29	8.41	7.31	6.26
$CO - CO$	13.67	12.18	11.77	10.81	9.57	8.16
$CO - C$		10.48	10.08	9.07	7.8	6.63
$CO - O$		8.61	8.29	7.46	6.42	5.46
$C - C$	13.44	11.5	10.93	9.44	7.77	6.31
$C - O$	11.36	9.79			7.06	5.87

Table A.7: Viscosity collision integral $\Omega^{2,2}(\text{Å}^2)$ for temperature range 5000 K to 20000 K

Species	T(K)					
	5000	6000	8000	10000	15000	20000
$CO2 - CO2$	10.32	10.02	9.57	9.21	8.59	8.15
$CO2 - O2$	8.8	8.53	8.1	7.77	7.19	6.79
$CO2 - CO$	9.08	8.74	8.21	7.79	7.07	6.56
$CO2 - C$	7.95	7.62	7.15	6.78	6.14	5.71
$CO2 - O$	6.92	6.66	6.28	6.01	5.49	5.15
$O2 - CO$	7.54	7.23	6.73	6.36	5.7	5.25
$O2 - C$	5.94	5.69	5.3	5.01	4.5	4.16
$CO - CO$	7.7	7.33	6.75	6.31	5.54	5.01
$CO - C$	6.26	5.98	5.54	5.21	4.63	
$CO - O$	5.17	4.93	4.58	4.31	3.84	3.52
$C - C$	5.92	5.6	5.11	4.71	3.94	3.38
$C - O$		5.17	4.69	4.3	3.57	3.18

A.5   Representative chemical composition of Mars soil

Table A.8: chemical composition of Mars soil

Constituent	Concentration %
S_iO_2	43.4
Fe_2O_3	18.2
Al_2O_3	7.2
SO_3	7.2
MgO	6
CaO	5.8
Na_2O	1.34
Cl	0.8
P_2O_5	0.68
T_iO_2	0.6
MnO	0.45
Cr_2O	0.29
K_2O	0.1
CO_3	<2
H_2O	0-1

Appendix B

Fluxes computation

The space discretization is performed in cell-centered finite-volume method. The fluxes on the cell surfaces are calculated using flux splitting scheme from average values on the left (l) and right (r) side of the cells (see figure B.1). The MUSCL (Monotone Upstream-centered Schemes for Conservation Laws) scheme is used for the solution vector at the cell surfaces.
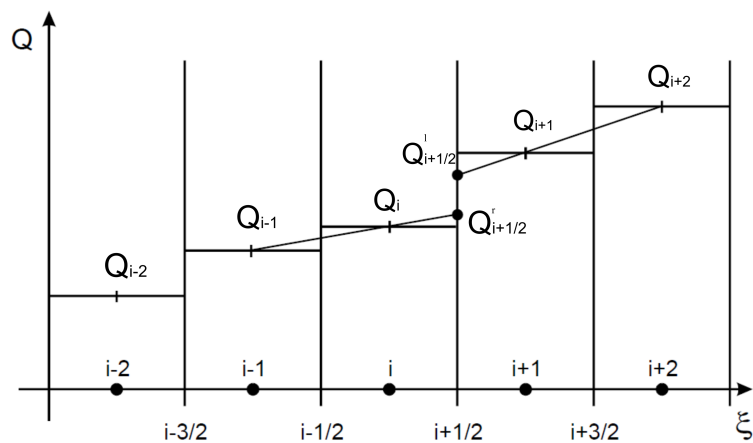

Figure B.1: Flux determination at walls of cells

The following formulation is implemented based on the work of Anderson, Thomas and Van Leer [80]:

$$(Q_{i+\frac{1}{2}})_l = Q_i + \left\{ \tfrac{1}{4} s_{Alb,i} \Big[(1 - S_M s_{Alb,i+1})(Q_i - Q_{i-1}) + (1 + S_M s_{Alb,i})(Q_{i+1} - Q_i) \Big] \right\}_i,$$

$$(Q_{i+\frac{1}{2}})_r = Q_{i+1} + \left\{ \tfrac{1}{4} s_{Alb,i} \Big[(1 - S_M s_{Alb,i+1})(Q_{i+2} - Q_{i+1}) + (1 + S_M s_{Alb,i})(Q_{i+1} - Q_i) \Big] \right\}_{i+1},$$
$$(B.1)$$

where the TVD flux limiter is used from Van Albada [19]:

$$S_{Alb,i} = \frac{2(Q_{i+1} - Q_i)(Q_i - Q_{i-1}) + \epsilon}{(Q_{i+1} - Q_i)^2 (Q_i - Q_{i-1})^2 + \epsilon}, \tag{B.2}$$

where ϵ is used in order to avoid instabilities in the flowfield and to limit maximum changes in the fluxes. This also prevents a division by zero. The value is taken around $10^{-5} - 10^{-6}$.

AUSM$^+$ Scheme

The Advection Upstream Splitting Method (AUSM) scheme was introduced by Liou and Steffen in 1991. The AUSM scheme defines a cell interface Mach number based on characteristic speeds from the neighboring cells. The interface Mach number is used to determine the upwind extrapolation for the convective part of the inviscid fluxes. A separate splitting is used for the pressure terms. Generalized Mach number and pressure splitting functions were described by Liou and the new scheme was termed ASUM+.

This numerical scheme is explained in detail in [19; 81; 82]. However, it is worthy to mention here that at the cell faces, the speed of sound is computed using the following simple formulation*:

$$a_{i+\frac{1}{2}} = \frac{1}{2}(a_i + a_{i+1}), \tag{B.3}$$

where a_i and a_{i+1} are used to express frozen speed of sound in the cell i and $i + 1$ respectively.

---

*In future it is intended to be revised

Curriculum Vitae

Personal

Name:	Abdul Majid
Birth:	2nd of May 1977
Birth Place:	Sahiwal, Pakistan
Nationality:	Pakistani
Martial Status:	Married
email:	majid363@yahoo.com

Education

04/2007-Present	PhD in Aerospace Engineering, Student at Institute of Space Systems, University of Stuttgart, Stuttgart, Germany
09/2003-12/2004	Masters of Sciences in Aeronautical Engineering, Institut Supérieur de l'Aéronautique et de l'Espace (ISAE), Toulouse, France
1996-2000	Bachelor of Sciences in Mechanical Engineering, University of Engineering and Technology, Lahore, Pakistan

Professional

2006-Present	Manager (Design & Development), Pakistan Space and Upper Atmosphere Commission SUPARCO, Pakistan, on study leave abroad for PhD studies in aerospace engineering
2004-2006	Assistant Manager (Design & Development), SUPARCO, Pakistan
01/2001-07/2001	Participant in a training program for aerospace engineering in Islamabad Institute of Space Technology, (IIST)